SOLID-STATE DYE-SENSITIZED MESOPOROUS TiO$_2$ SOLAR CELLS

THÈSE N^O 2187 (2000)

PRÉSENTÉE AU DÉPARTEMENT DE CHIMIE

ÉCOLE POLYTECHNIQUE FÉDÉRALE DE LAUSANNE

POUR L'OBTENTION DU GRADE DE DOCTEUR ÈS SCIENCES

PAR

Udo BACH

Diplom-Chemiker, Universität Konstanz, Allemagne
de nationalité allemande

accepteé sur proposition du jury:

Prof. M. Grätzel, directeur de thèse
Dr D. Lupo, rapporteur
Dr B. O'Regan, rapporteur
Prof. L. Zuppiroli, rapporteur

Lausanne, EPFL
2000

To my parents

Abstract

The objective of this work was to develop a solid-state dye-sensitized solar cell, in which the liquid electrolyte, commonly applied in photoelectrochemical cells, is replaced by a solid organic charge transport material (*spiro*-OMeTAD).

The dye-sensitized nanostructured solid-state junction realized in this work shows monochromatic photon-to-electron conversion efficiencies (IPCE) as high as 50 % (uncorrected for transmission losses) compared to 70 % IPCE for similar *photoelectrochemical* cells. Maximum white light conversion efficiencies reach 1.8 % (AM1.5; 10 mW/cm^2). This is the first time that dye-sensitized hybrid organic/inorganic solar cells with such high conversion yields are obtained exceeding previously reported performances by about two orders of magnitude. Transient laser spectroscopy showed that dye regeneration in the solid junction proceeds at least one order of magnitude faster than in comparable photoelectrochemical systems, however the analysis of photocurrent action spectra revealed interfacial charge recombination during charge collection as the cells main loss mechanism. Blocking of the SnO$_2$-glass window material with a dense TiO$_2$ layer proved to be vital in avoiding internal short circuits in the cell, while gold, platinum, graphite and conducting polythiophene polymers were found to be suitable materials to establish ohmic contacts to *spiro*-OMeTAD. The conductivity of thin *spiro*-OMeTAD films was adjusted by the addition of appropriate dopants like the diradical cation *spiro*-OMeTAD^{++}(PF$_6^-$)$_2$, which was synthesized and isolated in crystalline form. The electronic properties of organic/inorganic photovoltaic junctions could be controlled by means of a self-assembled organic layer located at the heterojunction. The dipole moment of the self-assembling molecules was found to be the chief parameter, controlling the rectifying junction properties. Finally, mobility studies were conducted on charge transport materials containing *spiro*-centers. High charge mobilities were measured, comparable to those of non-*spiro*-analogues. The '*spiro*-concept' therefore proved to be a powerful strategy to confer high morphologic stability to a material, while maintaining its electronic properties.

Résumé

Le but de ce travail a été le développement d'une pile solaire, nanocristalline à colorant, dans laquelle l'électrolyte liquide, couramment appliqué dans des cellules photo-electrochimiques, est remplacé par un transporteur de charges organique à l'état solide (*spiro*-OMeTAD).

La jonction solide sensibilisée par un colorant réalisée dans ce travail affiche des efficacités de conversion de la lumière incidente (IPCE) atteignant 50 % (non corrigés pour les pertes de transmission), ce qui est comparable avec les 70 % atteints par des cellules photo-électrochimiques à jonction électrolytique. Les rendements de conversion de l'énergie sous illumination en lumière blanche atteignent 1.8 % au maximum (AM1.5; 10 mW/cm^2). C'est la première fois qu'une cellule solaire solide hybride organique/inorganique basée sur un colorant, montre des rendements aussi élevés, dépassant les performances rapportées jusqu'à présent de deux ordres de grandeur. En utilisant la spectroscopie laser on a pu montrer que la régénération du colorant par le transporteur de trou est dix fois plus rapide que pour des systèmes photo-électrochimiques basé sur le couple I_3^-/I^-. Néanmoins, l'analyse des spectres d'action de photocourant a montré que la recombinaison de charges à travers l'interface constitue le mécanisme de perte principal. La passivation de la surface de SnO_2 par une couche dense de TiO_2 est nécessaire afin d'éviter des courts-circuits internes, tandis que l'or, le platine, le carbone et des polymères conducteurs comme des polythiophènes sont des matières convenables pour établir un contact ohmique avec le *spiro*-OMeTAD. La conductivité des couches minces de *spiro*-OMeTAD a été ajustée en ajoutant des dopants appropriés comme le diradical cation *spiro*-OMeTAD$^{++}(PF_6^-)_2$, qui a été synthétisé et isolé sous sa forme cristalline. Les propriétés électroniques des jonctions photovoltaïques organique/inorganique ont pu être contrôlées en utilisant des couches auto-assemblées, localisées à l'interface. Le moment dipolaire des molécules auto-assemblées a été identifié comme le paramètre principal contrôlant les propriétés de la jonction rectifiante. Finalement des études sur la mobilité de charge ont été réalisées avec des conducteurs de trous possédant un centre *spiro*. Des mobilités de charge élevées, comparables à celles de composés analogues dépourvus de centre *spiro*, ont été mesurées. Le concept '*spiro*' est donc une stratégie efficace pour conférer des stabilités morphologiques élevées a un composé tout en maintenant ses propriétés électroniques.

Zusammenfassung

Ziel dieser Arbeit war es, den gegenwärtig in photoelektrochemischen Solarzellen verwendeten flüssigen Elektrolyten durch ein organisches Ladungstransportmaterial (*spiro*-OMeTAD) zu ersetzen.

Die in der vorliegenden Arbeit untersuchte nanostrukturierte, farbstoffsensibilisierte Solarzelle wandelt Photonen in Elektronen mit Quantenausbeuten (IPCE) von bis zu 50 % (ohne Berücksichtigung von Transmissionsverlusten), im Vergleich zu 70 % für entsprechende photoelektrochemische Zellen. Bei simuliertem Sonnenlicht (AM1.5; 10 mW/cm^2) wurden Wirkungsgrade von bis zu 1.8 % gemessen. Dies entspricht einer Verbesserung gegenüber bereits bekannten, vergleichbaren Systemen um etwa zwei Grössenordnungen. Laserspektroskopische Untersuchungen zeigten, dass die Regenerierung des photooxidierten Farbstoffes mehr als zehn mal schneller verläuft als in vergleichbaren photoelektrochemischen Systemen, während eine genauere Auswertung von IPCE Spektren die Ladungsrekombination über die Phasengrenze hinweg als wichtigsten Verlustmechanismus aufdeckte. Die Passivierung der SnO$_2$ Oberfläche mittels einer kompakten TiO$_2$ Schicht erwies sich als unumgänglich, um interne Kurzschlüsse in der Solarzelle zu vermeiden, während Gold, Platin, Graphit und leitfähige Polythiophene sich als geeignete Kontaktmaterialien für *spiro*-OMeTAD erwiesen. Die Leitfähigkeit dünner *spiro*-OMeTAD Schichten konnte durch die Zugabe geeigneter Dotierstoffe wie z. B. dem Diradikalkation *spiro*-OMeTAD^{++}(PF$_6^-$)$_2$ gezielt erhöht werden. Die elektronischen Eigenschaften von TiO$_2$/*spiro*-OMeTAD Dioden konnten durch Adsorption von sich selbst organisierenden organischen monomolekularen Schichten kontrolliert werden. Es zeigte sich, dass das Dipolmoment der zur Oberflächenmodifikation verwendeten Moleküle einen entscheidenden Einfluss auf die rektifizierenden Eigenschaften des Heterokontaktes hat. Zuletzt wurden Ladungsmobilitätsmessungen an *spiro*-derivatisierten Lochleitern durchgeführt. Die gemessenen Ladungsträgermobilitäten sind mit denen der entsprechenden nicht-*spiro*-Verbindungen vergleichbar, womit sich das 'spiro-Konzept' als geeignete Strategie erwies, um hohe morphologische Stabilität und hervorragende Ladungstransport-eigenschaften in einem Material zu vereinen.

Chapter 1

Introduction

A tremendous increase in worldwide energy consumption, along with the threat that fossil energy resources might soon draw to a close encouraged the search for alternative energy sources. However one of the main drawbacks renewable energy projects have to face these days is the extraordinary cheap price of fossil energy, disregarding the consequential damage costs of its production and consumption. Only recently concerns of climatic consequences of the worldwide CO_2 production, along with renewed concerns about impending energy crises raised new interest in renewable energy sources on a political and economical level[1-3].

The field of photovoltaics is of major importance among renewable energy sources, as solar energy is largely abundant, surpassing our present global annual energy needs by a factor of 10,000. Harnessing this enormous potential of free energy represents an exciting challenge to scientists and politicians as well as the global economy. To date the field of photovoltaics is exclusively dominated by conventional inorganic semiconductor technologies like silicon or thin film solar cells. Drastic improvements in device manufacture led to a remarkable increase in energy conversion efficiencies and significant price cuts. However due to some fundamental concepts of classical inorganic pn-junction solar cells such devices will always demand the use of extremely pure starting materials and somewhat sophisticated production procedures. A very promising alternative to classical, inorganic pn-junction solar cells is the concept of nanoporous, dye-sensitized

photoelectrochemical solar cells, introduced by O'Regan and Grätzel[4] in 1991. Those cells exhibit impressive white light energy efficiencies of up to 10% while they are based on cheap starting materials and simple printing techniques[5]. They thereby represent the only alternative conceptual approach rivaling conventional solid-state solar cells.

Silicon pn-junction solar cell

hotoelectrochemical solar cell
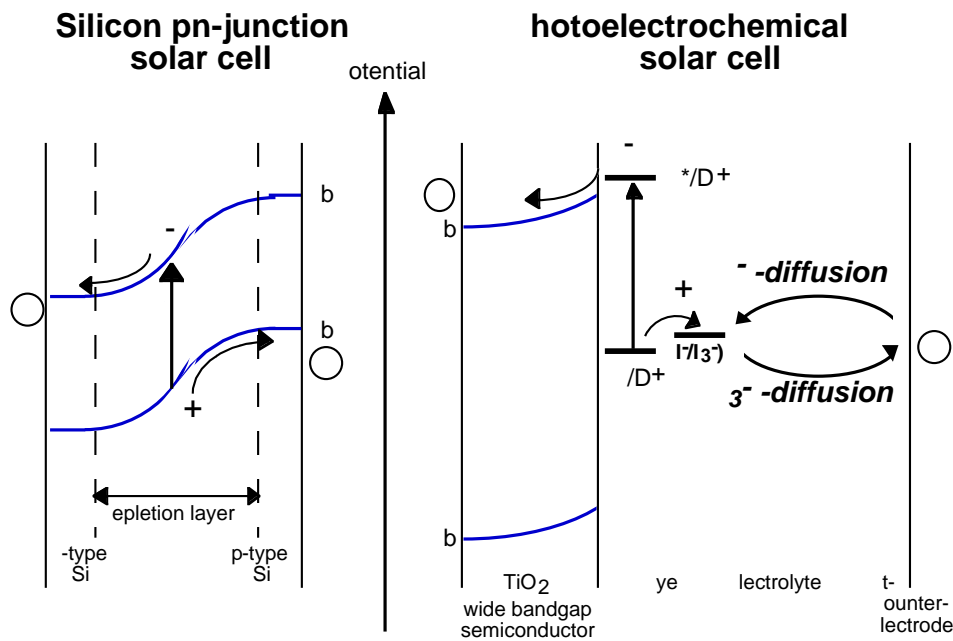
Figure 1.1 Simplified energy band schemes for silicon pn-junction solar cells and photoelectrochemical solar cells.

In a classical pn-junction solar cell a narrow bandgap semiconductor takes over the function of the light absorber and the charge transport material (see Figure 1.1). Interband excitation by absorption of a photon of $h\nu > E_{bandgap}$ promotes an electron from the valence band to the conduction band. Thereby an electron hole pair is formed. Whenever this process occurs inside or close to the depletion layer of the pn-junction, the internal built-in field will split the electron hole pair and the two charge carriers of opposite sign are directed towards the collecting electrodes. Inside such a pn-junction minority and majority charge carriers coexist in the same bulk volume. Hence these cells are very sensitive to the

presence of trace impurities or defects which can act as very efficient recombination centers, decreasing the external quantum efficiency. In order to avoid a significant decline in charge carrier collection efficiency due to bulk recombination, high efficiency pn-junction solar cells will always demand the use of ultrapure, highly crystalline materials, making silicon solar cell production cost and energy intensive. Dye-sensitized photoelectrochemical solar cells on the other hand, offer a possibility to circumvent this problem. In such cells a wide bandgap semiconductor like TiO_2 – a cheap, largely abundant starting material - is used instead. The semiconductor is sensitized to visible light by adsorption of a self-assembling monolayer of an organic or transition metal complex sensitizer. When the redox potential of the excited state of the dye $E(D/D^+)$ lies above the conduction band edge of TiO_2 electron injection from the exited state of the sensitizer to the TiO_2 will occur, leaving behind the radical cation of the dye. The dye ground state is regenerated by electron transfer from a donor, dissolved in the electrolyte. The oxidized donor will then reach the counter electrode via a diffusion mechanism, where it is subsequently reduced. **The fundamental advantage of dye-sensitized heterojunction solar cells arises from the fact that bulk recombination is suppressed, as only *majority* charge carriers are present in each of the two phases, confining recombination to the interface.**

Photovoltaic effects resulting from dye-sensitization of semiconductors are known for a long time[6,7] but remained of low efficiency. The achievement of Grätzel and his co-workers was to use a nanoporous sponge-like TiO_2 layer exhibiting a surface area which is about 3 orders of magnitude larger than that of a comparable flat device, resulting in an efficient light harvesting. An additional innovation was to use ruthenium(II)polypyridyl complexes, substituted with carboxylic groups which specifically bind to the TiO_2 surface (see Figure 1.2). *cis*-$Ru(dcbpy)_2(NCS)_2$ represents the most efficient sensitizer known so far, combining high charge injection efficiency with good light harvesting over the total visible range of the spectrum, down to the near infrared.
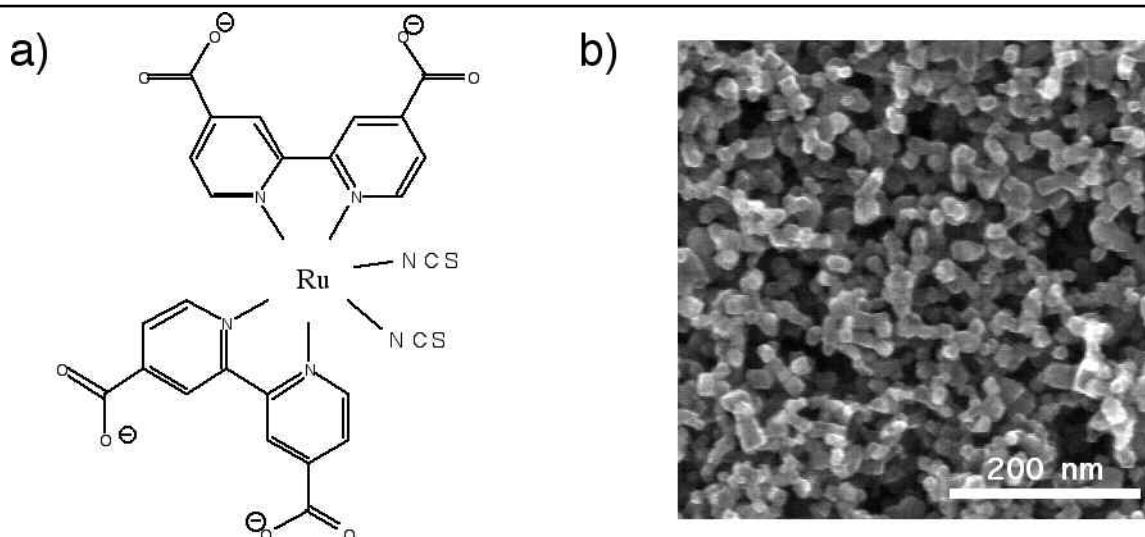
**Figure 1.2** a) chemical structure of cis-Ru(dcbpy)$_2$(SCN)$_2$; b) SEM micrograph of a thin film of nanocrystalline TiO$_2$.

Despite the very promising performance of these cells and contrary to earlier predictions the series production for commercial applications faced unexpected problems arising from the corrosive and volatile nature of the liquid iodine/iodide electrolyte used in such cells. While sealing of solid-state electronic components like computer chips or silicon solar cells towards water and oxygen is a standard technique, sealing of photoelectrochemical solar cells turned out to be a much more difficult task. Additional prerequisites towards the sealant like non-permeability for the electrolyte solvent and inertness towards the corrosive nature of iodine have to be guaranteed on the long-term. A second major problem is that conventional current-collector grids cannot be applied to photoelectrochemical solar cells, as even silver or gold grids do not resist the corrosive nature of the electrolyte. Practical advantages may therefore be gained by the replacement of the liquid electrolyte with a solid charge transport material. Inorganic p-type semiconductors have been tested in this regard, but photon-to-electron conversion efficiencies remained low.

The aim of this work was to elucidate, whether organic charge transport materials can be used to replace the liquid iodine/iodide electrolyte in standard photoelectrochemical solar cells, thereby forming a solid-state dye-sensitized

organic/inorganic heterojunction. Such heterojunctions were unknown in the literature when this work was started and preliminary attempts in our group to apply hole conducting substances like TPD or *spiro*-TAD as a replacement for the liquid electrolyte did produce photocurrents only in the nanoampere range.
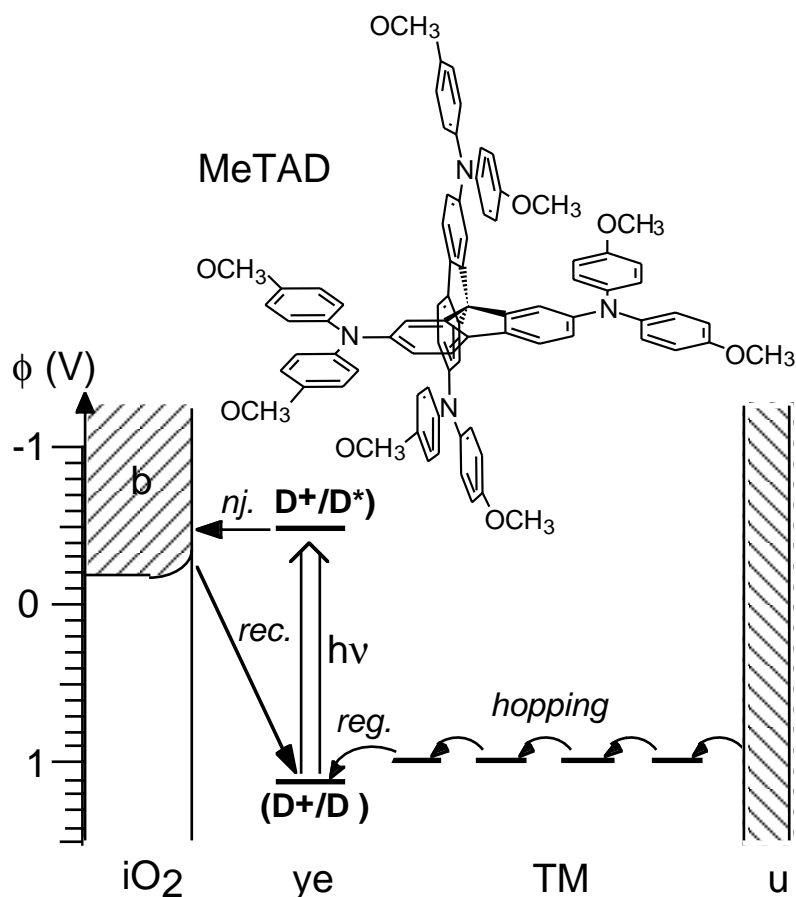
Figure 1.3 Scheme for the electron transfer processes (injection, regeneration, recapture, hopping) occurring in the dye sensitized heterojunction, as well as the approximate redox potentials and band energies of the different components. HTM stands for hole transport material.

The work was supported by a collaboration with Covion Organic Semiconductors GmbH/Frankfurt (Germany) (former Hoechst AG) who also provided the *spiro*-linked hole conducting materials. A patent covering the application of these organic semiconductors in dye-sensitized heterojunctions was submitted by Hoechst before the beginning of this work.

The solid-state approach

The basic functional principle of a dye-sensitized solid-state heterojunction is shown in Figure 1.3. As already described for classical dye-sensitized heterojunction solar cells absorption of a photon gives rise to the dye's electronically excited state from which electron injection into the conduction band of the TiO_2 proceeds. While the electron now reaches the working electrode via a percolation mechanism inside the porous TiO_2 structure the photooxidized dye has to be regenerated by a neighboring hole conductor molecule. Once the positive charge is injected into the organic charge transport material it is mobile via a hopping mechanism, by which it can reach the counter electrode.
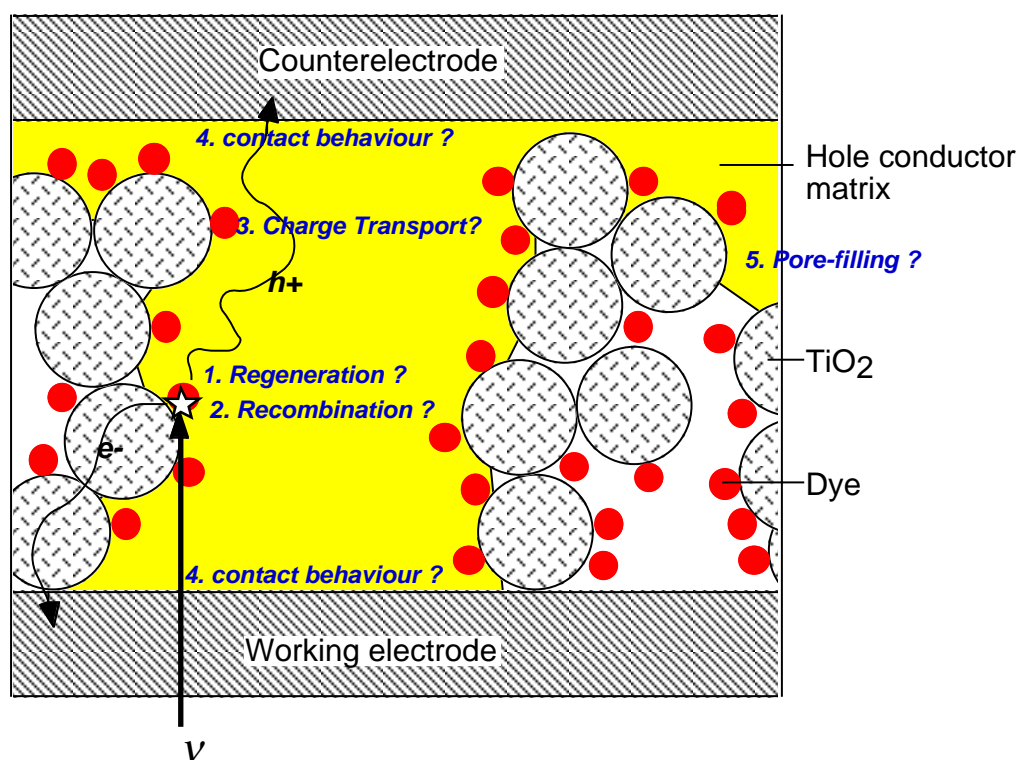
Figure 1.4 Summary of the problems, which might arise from replacing the liquid electrolyte by an organic charge transport material.

Several potential problems arise from this new configuration, which are summarized schematically in Figure 1.4. In order to reach high external photon-

to-electron conversion efficiencies each of the sequential electron transfer steps shown in Figure 1.3 needs to proceed with a quantum efficiency close to unity. As capture of TiO_2 conduction band electrons by dye radical cations competes with dye **regeneration** the latter has to be at least one order of magnitude faster than the recombination process. Once the hole was transferred to the hole conductor and the electron is located inside the TiO_2 phase **recombination** might still occur via the sensitized interface, so the lifetimes of the carriers has to be substantially longer than the time they require to reach the contacting electrodes.

In order to support high photocurrents the **charge transport** capacities of the two interpenetrating networks need to be sufficiently high, as not to limit the cell efficiency, due to their high ohmic resistances. These properties will mainly be governed by material properties such as charge mobility and charge carrier concentration. A further important requisite for a functioning solar cell is to find suitable contact and window materials, which show an appropriate **contact behavior** to both TiO_2 and the hole conductor. Iodine/iodide for example is known to have a very high overpotential at fluorine doped SnO_2 glass (which in the following will be referred to as SnO_2-glass). Photoelectrochemical solar cells based on iodine/iodide electrolytes therefore can be made by using SnO_2 glass on which the TiO_2 electrode is simply printed on top. However, when using an organic charge transport material internal short circuits due to an ohmic contact of the hole conductor and SnO_2 might occur. On the other hand one needs to make sure that the counter electrode material forms an ohmic contact with the hole conductor, as not to impede current flow from the hole conductor to the counter electrode. Finally one has to find a way to quantitative **pore filling** of the nanoporous TiO_2 structure with an organic matrix, so that each dye molecule is in close vicinity to the TiO_2 surface, as well as to a hole conductor molecule.

In the course of this work all the aforementioned problems shall be addressed individually by different techniques, probing potential loss mechanisms and finding practical solutions leading a way towards a functioning device and a

deeper understanding of the elementary processes contributing to the device performance.

References

1)   Bücher, K.; Fricke, J. Phys. in unserer Zeit **1990**, 21. Jahrg., Nr.6.

2)   Worldwatch Institute report, state of the world; annual reports, W. W. Norton & Company: New York.

3)   Scheer, H. Sonnenstrategie, Politik ohne Alternative; Piper GmbH: Munich, **1993**.

4)   O'Regan, B.; Grätzel, M. Nature **1991**, 353, 737-739.

5)   Nazeeruddin, M. K.; Kay, A.; Rodicio, I.; Humphry-Baker, R.; Müller, E.; Liska, P.; Vlachopoulos, N.; Graetzel, M. J. Am. Chem. Soc. **1993**, 115, 6382-6390.

6)   Moser, J. Monatsh. Chemie **1887**, 8, 373.

7)   Honda, K.; Fujishima, A. Nature **1972**, 238, 681-683.

Chapter 2

History & state of the art

In the following chapter a brief overview shall be given of solid-state solar cells involving organic components. Its aim is to give a short outline on the different concepts pursued to date, their advantages, drawbacks and potentials, in order to provide a comparison and measure with regards to the advances realized in this work. The first part will focus on *dye-sensitized* systems, where *dye-sensitized* shall be referred to as 'sensitization by a monolayer of dye, which self-assembled on the semiconductor surface', in order to distinguish it from organic thin film solar cells, which will be the subject of the second part of this chapter.

2.1 Solid-state dye-sensitized solar cells

In 1839 Becquerel[1] observed for the first time a photovoltaic effect on an illuminated silver electrode, immersed in an iodine/iodide electrolyte. About 48 years later J. Moser[2] was the first to report on the observation of a dye-sensitized photovoltaic effect. Similar to Becquerel's experiment Moser studied photoelectrochemical systems, where he observed a significant increase in photovoltage upon addition of an erythrosine dye to the electrolyte. Dye-sensitization processes and their theoretical understanding steadily improved since their first discovery, mainly due to their importance in photography.

It was only in 1988 that Tennakone[3] reported for the first time a *solid-state* dye-sensitized heterojunction between TiO_2 and CuSCN. However sensitized photocurrents were still low due to the nonporous structure of the junction.

Alternative approaches were undertaken since then to form *solid-state dye-sensitized* junctions, employing either wide bandgap semiconductors or organic semiconductors. These two approaches shall now be presented in more detail.

2.1.1   Inorganic solid-state dye-sensitized solar cells

In this approach a monolayer of dye is sandwiched between two inorganic wide bandgap semiconductors, while one of them exhibits a p-type and the other an n-type conduction mechanism. While wide bandgap n-type semiconductors are widely used, only few wide bandgap *p-type* semiconductors are known. Out of these Cu(I)SCN and Cu(I)I proved to be appropriate for their use in dye-sensitized solid-state junctions. A potential advantage of inorganic semiconductors is their generally high charge mobility compared to organic semiconductors. However the very limited choice of potentially interesting materials is a clear drawback, compared to the nearly unlimited choice of organic charge transport materials.

Analogous to their photoelectrochemical counterparts efficient dye-sensitized solid-state solar cells require a nanoporous junction structure. The first solar cell of this type was reported in 1995[4] in form of a $TiO_2/Cu(I)I$ heterojunction, sensitized with a cyanidine dye. Inorganic semiconductors commonly exhibit a crystalline structure on the nanometer scale. When forming an inorganic interpenetrating network on the nano-scale the crystal lattice mismatch of the two semiconductors will in almost any case impair the formation of a good contact between the mesoporous surfaces. Appropriate dyes might exhibit a certain buffer function between the two crystal structures – especially if the dye is substituted with two sets of attachment groups, each of them strongly interacting with one of the semiconductor components. In this case the sensitized nanoporous structure of one semiconductor component could efficiently act as a template similar to the mechanisms known from biomineralisation. Another one of its drawbacks, when compared to organic materials is the difficult

processability of most inorganic semiconductors. The solvent castability of CuI[4] represents a very exceptional advantage of this material.

Despite the apparent inconveniences of all-inorganic sensitized junctions their photon-to-electron conversion efficiencies have drastically increased over the past years. O'Regan et al.[5] recently reported on a system based on an electrodeposited layer of ZnO, sensitized with a phosphonated ruthenium polypyridyl complex. The heterojunction is finally formed by electrodeposition of CuSCN, growing inside the porous ZnO structure. White light solar energy conversion efficiencies of up to 1.5 % and photon-to-electron conversion efficiencies of up to 45 % have recently been obtained by such systems.

An alternative concept, strongly related to inorganic solid-state dye-sensitized solar cells, is to use an extremely thin layer of a low bandgap semiconductor as sensitizer, sandwiched between two wide bandgap semiconductors, forming a so-called η-solar cell (e.g. TiO_2/CdTe/CuSCN)[6]. So far only its concept was proposed in literature and its feasibility still has to be proven.

2.1.2 Inorganic/organic solid-state dye-sensitized solar cells

As already described in the previous section inorganic/organic heterojunctions have several advantages over their inorganic counterparts such as their nearly unlimited chemical tunability, their easy processability and their amorphous structure which easily adopts to any nanoporous inorganic template. The TiO_2/dye/*spiro*-OMeTAD junction studied in this work belongs to this category. However similar approaches were pursued in parallel in different laboratories.

Low molecular weight charge transport materials as well as semiconducting polymers were applied in such junctions. Hagen et al.[7] were the first to report on a solid-state device based on a molecular semiconductor, which was applied to a $Ru(dcbpy)_2(SCN)_2$ sensitized nanocrystalline TiO_2 electrode via thermal evaporation. However energy conversion efficiencies were still low (IPCE < 0.2

%). The first solid-state dye-sensitized heterojunction of TiO_2 and a semiconducting polymer was reported by Yanagida and co-workers[8,9]. They formed a solid-state heterojunction by electrodeposition of polypyrole into a nanoporous TiO_2 structure, sensitized with $Ru(dcbpy)_2(SCN)_2$. Solar energy conversion efficiencies were somewhat higher than for the system reported by Hagen and co-workers but still did not exceed 0.1 %. A thin film composite device was described recently by Kocher et al.[10], comprising a blend of dye-sensitized TiO_2 particles, a conducting polymer (LPPP) and C_{60}. However, an external bias was necessary to sustain a measurable photocurrent. This might be due to insufficient interparticle contact or insufficient doping of the device.

2.2. Organic thin film solar cells

Thin films of organic pigments were known to exhibit semiconducting properties from their use in reprography. Morel, Ghosh, Feng et al[11,12] reported on a solar cell in 1978 based on the Schottky junction of aluminum and a merocyanine dye, which showed an overall sunlight conversion efficiency of 0.7 % - about 35 times higher than any efficiency that had been reported on organic films before. Since then interest in organic solar cells strongly increased, in particular driven by the research effort undertaken by companies like Exxon, Xerox, Kodak and Shell in the 1980s, giving rise to numerous publications and review articles[13-16]. However, white light conversion efficiencies never exceeded 1 %[15], so that most research activities were abandoned.

In thin film organic solar cells light is adsorbed by dye molecules inside a dye layer, typically several tens of nanometers thick, forming an exciton – an electron/hole pair which is strongly bound. These excitons can give rise to free charge carriers by dissociation under the influence of a strong electric field. In general such fields develop close to the interface of two materials exhibiting different work functions due to the formation of a charge carrier depletion layer.

According to the origin of this built-in field one can distinguish three different types of organic solar cells:

Most organic photodiodes are based on the rectifying junction of an organic semiconductor and a metal, forming a **Schottky type cell** (1), such as the cell reported by Morel and co-workers[11]. A rectifying contact can also be formed by the formation of a pn-junction between the light absorbing, semiconducting dye and a second semiconductor of opposite conduction type. This second semiconductor can be an inorganic wide bandgap semiconductor (2) or a second light absorbing, semiconducting dye (3), giving rise to an **organic/inorganic** or **organic/organic pn-heterojunction**.

The main limitation of all three device types is the limited diffusion length of excitons in organic materials, which usually does not exceed several tens of nanometers. Therefore the photovoltaically active area in a thin film solar cell is limited to a very thin layer, close to the junction, which usually is too thin to assure a good light harvesting over a wide spectral range. Exciton lifetimes also strongly depend on the presence of bulk-impurities, demanding highly purified dyes. Heterojunction formation by two different organic dyes can improve the light harvesting, especially if their absorption spectra are complementary to each other[17,18]. However, layer thicknesses have to be optimized to prevent optical filter effects due to photovoltaically inactive areas away from the junction. Attempts were made to widen the thickness of the photovoltaically active area by incorporation of a co-evaporated layer of the two organic, semiconducting device components, resulting in a strong increase in device efficiency[19].

Another inconvenience of organic thin film solar cells is the limited conductivity of the organic layer. Organic devices commonly show strong sublinearity of the photocurrent at illumination intensities close to AM1.5 (100 mW/cm^2). However control of the charge carrier density via chemical doping with electron acceptors like iodine for p-type materials[20] or with donors like H_2 for n-type materials[21] can drastically improve the conductivity and the device performance.

An interesting approach, partially overcoming the problem of low conductivity and limited exciton diffusion widths is to combine two organic pn-junctions in series, leading to a tandem cell with a doubled photovoltage, compared to the simple pn-structure device[22].

Interpenetrating networks

As could be seen from the last section the recombination of an exciton before it reaches the built-in field region is the main loss mechanism in organic thin film solar cells. This problem can be overcome by the formation of an interpenetrating pn-heterojunction in which the average width of the p-type and n-type domains are smaller than the exciton diffusion length, thereby guaranteeing that almost every exciton can reach the interface before it decays. However the role of the electric field in these devices is somehow doubtful, as the depletion layer width is generally much wider than the dimension of phase segregation. It might be more exact to assume the totality of the interpenetrating network to be depleted with exciton splitting occurring via an interfacial electron transfer mechanism. Similar to thin film solar cells the rectifying junction can be formed by two organic semiconductors or a blend of an organic and an inorganic semiconductor.

Semiconducting polymers are superior to their low molecular weight analogues, concerning their applicability in interpenetrating junctions. This is due to the fact that charge transport in semiconducting polymers mainly proceeds along the polymer chain, so that percolation starts already at low concentration thresholds (for a review on polymer solar cells see [23]).

Poly(p-phenylenevinylene) derivatives are the most prominent examples for polymers used in organic solar cells. Depending on their substituents they can either exhibit p-type or n-type behavior. The first junction of this type was reported in 1995, using a phase–segregated thin film of MEH-PPV as p-type material and CN-PPV as n-type material[24]. The phase separation was on the scale

of 10-100 nm and IPCE values as high as 6% were recorded. Recently significantly improved device performances were reported, based on a polythiophene/PPV-derivative heterojunction, assembled via a lamination technique with IPCE values reaching 29%[25].

A different approach to form organic interpenetrating heterojunctions is to strongly dope a p-type conducting polymer with a low molecular weight acceptor until charge percolation occurs inside the acceptor phase. The blends attracting most attention are those of PPV- or thiophene derivatives doped with fullerenes as acceptor, reaching 23 % IPCE for polythiophene/C_{60} junctions[26] and 29 % for PPV/C_{60} junctions[27]. Perylene nanocrystals were also used as doping acceptor[28]. Different theoretical models were developed to describe the functioning principals of these devices[29,30].

Recently increased interest was raised in composites of semiconducting polymers and nanosized semiconductor particles, where either the polymer or the semiconductor *and* the polymer take over the function of the light absorber. Among those nanocrystalline heterojunctions of TiO_2 with either PPV[31] or polythiophene[32] derivatives have received particular interest. Several different techniques were applied to form the heterojunctions. Commonly the first step was the formation of a nanoporous thin film of TiO_2 via spray pyrolysis or via deposition of a colloidal paste followed by a sintering step, while the polymer was applied via a spin-coating technique or (in the case of polythiophene) via electrodeposition. IPCE values reported on these systems are still very low (below 3%). However just recently highly efficient TiO_2/polythiophene solar cells showing peak IPCE values of up to 10 % could be accomplished in our group[33]. Photovoltaic cells of comparable efficiency were obtained, when polycrystalline films of low bandgap semiconductors like CdSe, CdS or $CuInSe_2$ are contacted with a thin film of polythiophene via electrodeposition[34,35]. Overall white light conversion efficiencies of 1.3 % at 56 mW cm^{-2} were reported for a CdSe/poly(3-methylethiophene) junction[35].

One particularly interesting aspect of nanoparticle/polymer solar cells is that charge 'hopping' from one semiconductor particle to another takes place even in blends prepared from spincoating solutions containing both, the polymer and the colloidal nanoparticles. Usually those devices are not exposed to successive heat treatments. This is surprising, as nanocrystalline semiconductor films used in photoelectrochemical solar cells generally need such a heat treatment to induce interparticle contact and 'necking'. If this heat treatment could be made redundant cheap, flexible dye-sensitized solar cells based on plastic substrates could be realized.

Various examples of composite nanoparticle/polymer films made via spincoating can be found in literature[10,36-38]. Most examples actually show that charge percolation inside the nanoparticle network is strongly reduced, compared to nanocrystalline, sintered films. Arango et al.[37] reported a decrease in photoconductivity of two orders of magnitude when comparing a sintered polymer-coated TiO_2 film, to a composite made via spin-coating of a TiO_2-colloid/polymer solution. The reduced interparticle contact also leads to low photovoltaic performances. An exception to these observations is the CdSe/PPV composite solar cell reported by Greenham and co-workers[38]. Peak IPCE values of 12 % were obtained from spin-coated composite thin films with a weight ratio of CdSe (ø 5 nm):MEH-PPV = 9:1 (film thickness = 300 – 500 nm). Removal of surface adsorbed species from the colloid, prior to the cell assembly was shown to be crucial for interparticle electron transfer to occur.

References

1) Becquerel, E. *C.R. Acad.. Sci. Paris* **1839**, *9*, 561.

2) Moser, J. *Monatsh. Chemie* **1887**, *8*, 373.

3) Tennakone, K.; Hewaparakkrama, K. P.; Dewasurendra, M.; Jayatissa, A. H.; Weerasena, L. K. *Semicond. Sci. Technol.* **1988**, *3*, 382-387.

4) Tennakone, K.; Kumara, G. R. R. A.; Kumarasinghe, A. R.; Wijayantha, K. G. U.; Sirimanne, P. M. *Semicond. Sci. Technol.* **1995**, *10*, 1689-1693.

5)   O'Regan, B.; Schwartz, D. T.; Zakeeruddin, S. M.; Grätzel, M. *Adv. Mater.* **2000**, *submitted.*

6)   Siebentritt, S.; Ernst, K.; Fischer, C.-H.; Könenkamp, R.; Lux-Steiner, M. C. *CdTe and CdS as extremely thin absorber materials in an eta solar cell*: Barcelona (Spain), 1997, pp 1823-1826.

7)   Hagen, J.; Schaffrath, W.; Otschik, P.; Fink, R.; Bacher, A.; Schmidt, H.-W.; Haarer, D. *Synth. Met.* **1997**, *89*, 215-220.

8)   Murakoshi, K.; Kogure, R.; Yanagida, S. *Chemistry letters* **1997**, *5*, 471-472.

9)   Murakoshi, K.; Kogure, R.; Wada, Y.; Yanagida, S. *Solar Energy Materials and solar cells* **1998**, *55*, 113-125.

10) Kocher, M.; Däubler, T. K.; Harth, E.; Scherf, U.; Gügler, A.; Neher, D. *Appl. Phys. Lett.* **1998**, *72*, 650-652.

11) Morel, D. L.; Ghosh, A. K.; Feng, T.; Stogryn, E. L.; Purwin, P. E.; Shaw, R. F.; Fishman, C. *Appl. Phys. Lett.* **1978**, *32*, 495-497.

12) Ghosh, A. K.; Feng, T. *Journal of Applied Physics* **1978**, *49*, 5982-5989.

13) Chamberlain, G. A. *Solar Cells* **1983**, *8*, 47.

14) Horowitz, G. *Adv. Mater.* **1990**, *2*, 287.

15) Woehrle, D.; Meissner, D. *Adv. Mater.* **1991**, *3*, 129.

16) Simon, J.; André, J. J. *Molecular semiconductors*; Springer-Verlag: Berlin, 1985.

17) Tang, C. W. *Appl. Phys Lett.* **1986**, *48*, 183.

18) Kudo, K.; Moriizumi, T. *Jpn. J. Appl. Phys.* **1981**, *20*, L553-L556.

19) Hiramoto, M.; Fujiwara, H.; Yokoyama, M. *Journal of Applied Physics* **1992**, *72*, 3781-3787.

20) Yamashita, K.; Harima, Y.; Matsubayashi, T. *J. Phys. Chem.* **1998**, *1989*, 5311-5315.

21) Hiramoto, M.; Kishigami, Y.; Yokoyama, M. *Chem. Lett.* **1990**, 119-122.

22) Hiramoto, M.; Suezaki, M.; Yokoyama, M. *Chem. Lett.* **1990**, 327-330.

23) Hadziioannou, G.; Hutten, P. F. v. *Semiconducting polymers*: Weinheim, 2000.

24) Halls, J. J. M.; Walsh, C. A.; Greenham, N. C.; Marseglia, E. A.; Friend, R. H.; S.C.Moratti; Holmes, A. B. *Nature* **1995**, *376*, 498-500.

25) Granström, M.; Petrisch, K.; Arias, A. C.; Lux, A.; Andersson, M. R.; Friend, R. H. *Nature* **1998**, *395*, 257-260.

26) Roman, L. S.; Mammo, W.; Pettersson, L. A. A.; Andersson, M. R.; Inganäs, O. *Adv. Mater.* **1998**, *10*, 774-777.

27) Yu, G.; Gao, J.; Hummelen, J. C.; Wudl, F.; Heeger, A. J. *Science* **1995**, *270*, 1789.

28) Dittmer, J. J.; al., e. *Sol. Energy Mater. Sol. Cells* **2000**, *61*, 53-61.

29) Köhler, A.; Santos, D. A. d.; Beljonne, D.; Shuai, Z.; Brédas, J. L.; Holmes, A. B.; Kraus, A.; Müllen, K.; Friend, R. H. *Nature* **1998**, *392*, 903-906.

30) Pettersson, L. A. A.; Roman, L. S.; Inganäs, O. *J. Appl. Phys.* **1999**, *86*, 487-496.

31) Savenije, T. J.; Warman, J. M.; Goossens, A. *Chem. Phys. Lett.* **1998**, *287*, 148-153.

32) Kajihara, K.; Tanaka, K.; Hirao, K.; Soga, N. *Jpn. J. Appl. Phys.* **1997**, *36*, 5537-5542.

33) Spiekermann, S. *unpublished results* .

34) Gamboa, S. A.; Nguyen-Cong, H.; Chartier, P.; Sebastian, P. J.; Calixto, M. E.; Rivera, M. A. *Sol. Energy Mater. Sol. Cells* **1998**, *55*, 95-104.

35) Chartier, P.; Cong, H. N.; Sene, C. *Sol. Energy mater. Sol. Cells* **1998**, *52*, 413-421.

36) Salafsky, J. S.; Lubbrthuizen, W. H.; Schropp, R. E. I. *Chem. Phys. Lett.* **1998**, *290*, 297-303.

37) Arango, A. C.; Carter, S. A.; Brook, P. J. *Appl. Phys. Chem.* **1999**, *74*, 1698-1700.

38) Greenham, N. C.; Peng, X.; Alivisatos, A. P. *Physical Review B* **1996**, *54*, 17628.

Chapter 3

Experimental

3.1 Materials

Unless otherwise stated all chemicals used were at least reagent grade, purchased from Fluka AG or Aldrich, Switzerland. Solvents were at least puriss. p.a. (Fluka&Aldrich).

Ruthenium polypyridyl complexes were used as received from our co-workers Dr. Nazeeruddin and Dr. Zakeeruddin.

The merocyanine dyes Mc2, Mc3 and Mc4 were used as received from Riedel-de-Haën, Germany.

The perylene dye was used as received from the group of Prof. Langhals, Munich/Germany.

Spiro-OMeTAD and analogue substances were used as received from Dr. Spreitzer - Covion Organic Semiconductor GmbH, Frankfurt/Germany (formerly Aventis, formerly Hoechst AG). If not stated otherwise the purity was > 99.8 %, according to HPLC analysis.

3.1.1 OMeTAD(PF$_6$)$_2$

The hexafluorophosphate salt of the diradical cation of *spiro*-OMeTAD was synthesized according to the following procedure:

A solution of [N(p-C$_6$H$_4$Br)$_3$][SbCl$_6$] (844 mg) and of tetrabutylammonium hexafluorophosphate (6.51 g) in acetonitrile (250 ml) was added dropwise to a stirred solution of *spiro*-OMeTAD (576 mg) in chlorobenzene (2.5 ml). The reaction mixture was stirred for another 30 minutes, its volume reduced to about 20 ml (bath temperature 30°C) and stored for one week in the refrigerator at 5°C.

The precipitate was filtered off, washed with a small amount of methanol, then dried in air and stirred for further 15 minutes in toluene (20 ml). The crude product was filtered off, then washed with toluene (10 ml) and dried overnight in vacuum. Yield: 702 mg/98.5 %.

The crudum was dissolved in acetonitrile (50 ml) and filtered. Then tetrabutylammonium hexafluorophosphate (16.25 g) was added to the solution. After storing the mixture at 5 °C for a time period of several days, the precipitate was filtered off and washed with acetonitrile (2 ml) and methanol (10 ml), then stirred for 15 min in toluene (40 ml). The pure compound was filtered off and dried over night under vacuum. Yield: 360 mg/51 %.

Elemental analysis (CHN):
calculated: C: 64.20 %;   H: 4.52 %;   N: 3.68 %   Br, Cl, I: 0.00 %
found: C: 64.10 %;   H: 4.52 %;   N: 3.76 %   Br, Cl, I: 0.35 %
(the starting material [N(p-C$_6$H$_4$Br)$_3$][SbCl$_6$] is 55.41 % in Br, Cl, I)
EPR and UV/VIS spectra see Chapter 4

3.2 Instrumental

UV/VIS spectroscopy

Absorption spectra were recorded using a Varian spectrophotometer (model Cary 1E or Cary 5 equipped with an integrating sphere).

Current-voltage characteristics

Current-voltage characteristics were measured using a computer controlled potentiostat EG&G Princeton model 273A (dark currents) or a Keithley 2400 SourceMeter for photovoltaic characterizations as described below.

EPR measurements

Conventional electron magnetic resonance spectra (first harmonic, absorption in phase) were measured using a Bruker ESR spectrometer (model ER 4162 ST, x-band) equipped with a standard TE102 cavity (model ER 4162 ST), kindly made available by the research group of Prof. Zuppiroli (Département de Physique/EPFL). All samples were measured under ambient temperature conditions.

Kelvin probe technique

The Kelvin probe technique is a non-contact method for measuring the potential difference between a reference probe and a sample surface being brought in close proximity of each other (distance about 1 mm). Due to electromechanically induced vibration of the probe with respect to back contacted and grounded

sample, an AC current appears in the external circuit because of the capacitance modulation in the presence of an electrostatic field. By a phase sensing demodulator and a feedback loop, the amplitude of the current is nullified. The externally applied voltage, needed for current compensation is the actual read-out of the measurement being equal, but opposite in sign compared to the contact-potential difference (CPD). From the CPD the workfunction of the sample can be calculated by subtracting the measured value for the CPD from the workfunction of the metal reference probe, which is assumed to be constant[1,2]. The Kelvin probe apparatus (Besocke Delta ϕ, Jülich, Germany) was placed in a Farraday cage inside a glove box (argon atmosphere, $H_2O < 10$ ppm).

3.3 Thin film deposition techniques

3.3.1 Spray pyrolysis

The precursor $[Ti(acac)_2(i\text{-}C_3H_7O)_2]$ was synthesized under inert gas atmosphere by dropwise addition of acetylacetone to a stirred solution of $[Ti(i\text{-}C_3H_7O)_4]$ (molar ratio 2:1). A solution of $[Ti(acac)_2(i\text{-}C_3H_7O)_2 + 2 \ i\text{-}C_3H_7OH]$ (TAA) is formed thereby and stored under argon atmosphere, prior to use. This precaution was taken despite the fact that TiO_2 films made from solutions stored for several years under normal atmosphere showed similar current-voltage characteristics to films made from freshly prepared solutions. The TAA solution, which was 2 M in $[Ti(acac)_2(i\text{-}C_3H_7O)_2]$ was diluted 1:9 (TAA:EtOH) to 0.2 M immediately before each coating process. TAA solutions are also commercially available from Lancaster Synthesis Ltd/England.

The spray pyrolysis process was performed, following the procedure published by Kavan and co-workers[3]. The aerosol was prepared using a chromatographic atomizer. The handheld device was directed on the sample, sitting on a massive

titanium plate (10x280x200 mm) with a controlled temperature (NiCr/Ni thermopile). The distance between sample and atomizer was about 15-20 cm at varying angles. Each single spraying process produced an aerosol of about 50 ml gas volume, containing roughly 150 µl of atomized solution. The substrates were carefully cleaned prior to the coating process by sequential sonification in ethanol, acetone, Helmanex and ultrapure water (< 0.5 µS/cm, 0.2 µm filter). Thin 1 mm float glass was used to mask areas which were not supposed to be coated with TiO_2.

Thin films of TiO_2 were prepared by sequential repetition of single spraying steps with a defined number of repetitions and defined breaks. Typically a surface of 5x5 cm was exposed to two single spraying steps, followed by a 10 seconds break prior to subsequent spraying. 5 to 40 repetitions of this cycle were accomplished to finally form the TiO_2 layer. The device was thermally equilibrated on the hotplate for at least 5 minutes prior to the spray-coating process and left for at least 5 minutes after the deposition, to complete the conversion process.

Advanced spray pyrolysis set-up

As the film preparation parameters are poorly controlled, when using the handheld/handdriven atomizer described above, a more sophisticated setup was realized, which schematically is shown in Figure 3.1. The fluxes of the carrier gases and the precursor solution can be controlled and regulated by separate flux meters, and by the setup parameters of the peristaltic pump (Pharmacia LKG pump C-1). Carrier gas and precursor solution are introduced into an ultrasonic nozzle (Lechler Ultraschall-Zerstäuber US1 – 710.070.16.60.00.0; Metzingen/Germany; 100 kHz; 8 W; opening angle 30°). The typical drop size for aerosols made from aqueous solutions is specified to be 22 µm (standard deviation 1.7 µm). The nozzle itself sits on a cylindrical glass cover of a diameter of 8 cm and a height of 22 cm. This glass cover was replaced by an explosion safe

metal cylinder with a loose cover, whenever there was concern that the enclosed aerosol be self-explosive at the hotplate temperature.
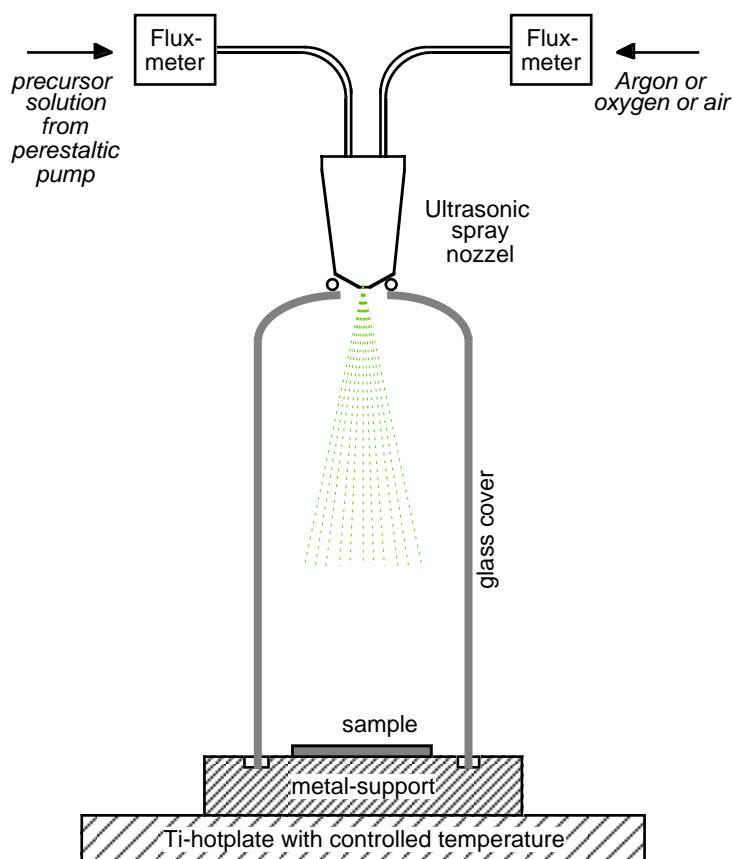

Figure 3.1. Spray pyrolysis set-up with an integrated ultrasonic nozzle.

The glass or metal cylinder was placed on a metal base plate, on which the sample was placed. The metal substrate sat on a temperature controlled titanium plate. The hotplate and metal substrate were thermally equilibrated for at least 90 minutes prior to the experiment and its temperature controlled separately in the metal substrate via a thermocouple. The whole setup was permanently placed in a hood and protected with an explosion shield.

Experiments were also conducted with a base plate equipped with thin channels under the substrates. A vacuum was applied via these channels (50 mbar) to improve the thermal contact between the substrate and the base plate similar to the set-up introduced by Smestad et al.[4]. However the missing contact at the

device areas above the channels turned out to introduce a strong temperature inhomogenity which was not observed in absence of the vacuum chuck[1].

3.3.2 MOCVD set-up

For MOCVD experiments the advanced spray pyrolysis set-up described above was slightly modified. The ultrasonic nozzle was replaced by a T-piece, in which two separate gas flows were united just before the injection into the reaction cylinder. Bubbling of an appropriate carrier gas through a heated and stirred precursor liquid/solution generated the precursor vapors. The second gas stream eventually contains a further reactant such as oxygen or water. Water saturation of the carrier gas was reached by bubbling of the carrier gas through water. The fluxes of both gaseous components were controlled via appropriate flux meters.

3.4   Photovoltaics

3.4.1   Definitions & measuring conditions

Short-circuit current (Isc). Cell current (density) measured at an applied potential of zero volt.

Open-circuit voltage (U_{oc}). External bias voltage, at which the measured cell current is zero.

---

[1]   Temperature gradients could be revealed when TiO_2 depositions were done at substrate temperatures between 250 and 300 °C. Films growing on cooler substrate surfaces exhibited a stronger scattering than those growing on somewhat hotter areas. This temperature dependence of the TiO_2 particle size formed via spray pyrolysis was already reported by Yanagi et al.[5].

Power output (P). For a given bias voltage the power output of the cell is the product of the measured cell current and the bias voltage $P(V) = U \times I$. $P(V)$ generally increases when V is increased from zero, goes through a maximum and decreases to zero at $V = Voc$. I_{max} and V_{max} are the coordinates of the maximum in the $P(V)$ curve (maximum power point). The maximum power corresponds visually to the area of the largest rectangle, which can fit inside the current voltage curve.

Fill-factor (FF). The fill factor is defined as

$$FF = \frac{I_{max} \cdot V_{max}}{I_{SC} \cdot V_{OC}}$$

(3.1)

Efficiency (η). The efficiency is defined as the ratio of maximum electric power output to the radiation power incident on the solar cell surface.

$$\eta = \frac{P_{max}}{P_{in}} = \frac{I_{SC} \cdot V_{OC} \cdot FF}{P_{in}}$$

(3.2)

η is directly proportional to FF, Isc and Uoc. Efficient solar cells therefore need to be optimized with respect to each of these three parameters. Efficiencies are dependent on the incident irradiation power and its spectral distribution. Both parameters should be indicated, whenever η is mentioned.

AM 1.5. AM 1.5 (air mass 1.5) is a specific calculated spectral distribution, which corresponds to the spectrum of sunlight at sea level after traversing the atmosphere 1.5 times. If not specified differently AM 1.5 conditions correspond to an incident radiation energy per surface area of 1000 W/m^2 (100 mW/cm^2).

Spectral mismatch & calibration. Artificial light sources will always have a spectrum different from AM 1.5 conditions, even when corrected with appropriate 'sunlight filters' (Oriel$^{©}$). To quantify the difference in spectral distribution a mismatch factor is defined (analog to reference [6]):

$$M = M_{RC} \cdot M_{TC}^{-1} = \frac{\int E_{AM1.5}(\lambda)S^{RC}(\lambda)d\lambda}{\int E_{sim}(\lambda)S^{RC}(\lambda)d\lambda} \cdot \frac{\int E_{sim}(\lambda)S^{TC}(\lambda)d\lambda}{\int E_{AM1.5}(\lambda)S^{TC}(\lambda)d\lambda} \tag{3.3}$$

$E_{AM1.5}(\lambda)$, $E_{sim}(\lambda)$	=	relative spectral irradiation intensities of AM 1.5 and the simulated sunlight
$S_{RC}(\lambda)$ and $S_{TC}(\lambda)$	=	relative spectral sensitivity of reference and test cell

A reference cell (RC) is calibrated at standard AM 1.5/1000 (W/m^2) conditions and the value of the short circuit current ($I_{AM1.5}^{RC}$) under these conditions specified. This reference cell is used in the following to calibrate a sunlight simulator with an unknown overall radiation output, in order to determine the current output of a test cell under AM 1.5 conditions ($I_{AM1.5}^{TC}$). A photoreponse of I_{sim}^{RC} and I_{sim}^{TC} is measured under the simulated light conditions.

According to equation 3.3 two corrections (M_{RC} and M_{TC}) have to be considered. First of all, the spectral mismatch in the spectrally sensitive region of the *reference* cell (M_{RC}) and second the spectral mismatch in the spectrally sensitive region of the *test* cell (M_{TC}):

$$\frac{I_{sim}^{RC}}{I_{AM1.5}^{RC}} \cdot M_{RC} = \frac{I_{sim}^{TC}}{I_{AM1.5}^{TC}} \cdot M_{TC} \tag{3.4}$$

The current of the test cell under AM 1.5 conditions $I_{AM1.5}^{TC}$ therefore follows as:

$$I_{AM1.5}^{TC} = I_{sim}^{TC} \cdot \left(\frac{I_{AM1.5}^{RC}}{I_{sim}^{RC}} \right) \cdot M^{-1} \tag{3.5}$$

Equation 3.3 shows that the spectral mismatch factor M is exactly one, if reference and test cell have the same relative spectral sensitivity ($S_{RC}(\lambda) = S_{TC}(\lambda)$). From the above findings we can therefore conclude that:

- It is indispensable to use reference cells which are adjusted to the spectral response of the test cell.

- A specific mismatch factor is only valid for a specific combination of reference and test cell.

- M does not contain any information as to what extent the spectral distribution of the simulated light matches AM 1.5. An installation using a simple light bulb will have a mismatch factor M of exactly 1, if only the relative spectral responses of reference and test cells are equal. In order to conclude to what extent the spectral distribution of the simulated light corresponds to AM 1.5 (in the spectrally sensitive region of our test cell) the correction factor M_{TC} has to be considered.

Our photovoltaic characterization set-ups are calibrated with a silicon reference cell equipped with a Schott$^©$ KG3 filter. This filter is highly transmitting in the visible range, while it absorbs strongly in the UV and IR range. The spectral responses of the silicon reference cell and dye sensitized cells are thereby made similar (Silicon cells are highly sensitive to infrared light up to $\lambda = 1100$ nm, while the spectral response of dye sensitized cells is negligible above 850 nm). Calibration were performed by the PV calibration laboratory of *the Frauenhofer Institute for Solar Energy Systems ISE, Freiburg/Germany* and the *National Renewable Energy Laboratory* in Golden/Colorado. A xenon or sulfur lamp was used as a light source, both of them exhibiting spectral responses similar to AM1.5 sunlight. The xenon lamp was equipped with a Schott KG filter to correct for the strong radiation output in the near-IR, which is due to the specific emission peaks of the xenon ions above 800 nm. A spectral mismatch of our photovoltaic characterization set-up of 0.98 was derived[7] (xenon lamp (Oriel$^©$ 450 W) incl. KG filter/reference cell = silicon cell incl. KG3 filter /dye sensitized solar cell based on $Ru(dcbpy)_2(SCN)_2$ as sensitizer).

The spectral response (IPCE) is calibrated by comparing the relative spectral response of a test cell to the spectral response of a calibrated silicon test cell as a function of wavelength (Frauenhofer Institute in Freiburg).

Forward bias/reverse bias. The forward bias is the potential applied to a device where the n-type material is negatively charged and the p-type material positively charged. In case of SnO_2/*spiro*-OMeTAD/Au diodes the forward bias is defined as

a negative polarization of the SnO_2 electrode. The forward bias potential is defined to be negative. By definition, reverse bias corresponds to the opposite polarization.

Frontside / backside illumination. Front side illumination shall be defined as illumination through the SnO_2 glass substrate, while back side illumination is defined as the illumination through the counter electrode. This interpretation is arbitrary and examples can be found in literature using the inverse definition.

IPCE. (incident-photon-to-electron conversion efficiency, or external quantum efficiency or photoresponse). Defines the ratio of the number of electron/hole pairs ($n_{electrons}(\lambda)$) generated in the external circuit of the solar cell to the number of photons ($n_{photons}(\lambda)$) incident on the photovoltaically active surface of the device. If not specified differently the IPCE is measured under short circuit conditions. If the response of the test cell is not linear the IPCE will be a function of the light intensity Photocurrents measured under IPCE conditions at 550 nm were about 1/500 of the ones measured at full sun.

$$IPCE(\lambda) = \frac{n_{electrons}(\lambda)}{n_{photons}(\lambda)} = \frac{I(\lambda)/e}{P_{in}(\lambda)/h\nu} = \frac{I(\lambda)}{P_{in}(\lambda)} \cdot \frac{hc}{e\lambda}$$

(3.6)

$I(\lambda) =$ photocurrent measured under monochromatic illumination at λ with an irradiation intensity of $P_{in}(\lambda)$.

APCE (absorbed photon-to-electron conversion efficiency, internal quantum efficiency). Is the IPCE value, corrected for the real percentage of photons, which are adsorbed (not transmitted or reflected) by the photovotaically active component of the test cell.

3.4.2 Photovoltaic characterization set-up

The photovoltaic characterization set-ups are explained in great detail in the literature[7]. In addition to the IPCE and white-light measuring installation described therein a sulfur-lamp was employed to characterize the white-light response of test cells (model *solar 1000*; Fusionlighting Inc/USA). The lamp was equipped with a filter wheel holding several neutral density filters with different transmission behaviors and a monochromatic filter of 520 nm (band halfwidth of about 50 nm). The position of the filterwheel could be selected automatically by means of a computer. The sample holder was placed under the filterwheel. The homogeneity of the spot size was large enough to illuminate a 7x7 cm area, corresponding to AM 1.5/1000 W/cm^2 with local differences in light intensity of less than 5%. The sample holder could simultaneously hold four cells having four contacts each. Each of the 16 test cells was separately addressable and its current-voltage characteristic could be measured and recorded, using a computer controlled potentiostat (2400 Source Meter, Keithley/USA). Using a computer program (Igor Pro) all 16 cells could be characterized concerning their current-voltage characteristics at four different light levels, in the dark and with monochromatic light of 520 nm.

The IPCE set-up was modified with a sample holder holding one sample with four contacts. All four cells were automatically characterized in sequence. A stepper motor was used to bring the measured test cell into the measuring position. All four test cells could be characterized automatically. Both sample holders were equipped with an aeration system, allowing for measurements under controlled atmosphere conditions.

3.4.3 Device preparation

Structured SnO_2 glass:

SnO_2 glass (Asahi, typ 'u', 1 mm) was cut into 100x100 cm plates and then structured by Zn/HCl etching (20 mg/cm^2 zinc granulate (Fluka, puiss.: grit 96453), 1 ml/cm^2 4N HCl, 3 min. reaction time; 2 repetitions). Scotch$^©$ tape was used as mask material. After etching the samples were cut into 25x25 mm plates exhibiting an etched band of 9x25 mm on one side. Prior to any further experiments these substrates were cleaned by subsequent sonification for 10 minutes in various solvents (acetone, ethanol, Hellmanex$^®$ II (2 % in H_2O), H_2O, H_2O, H_2O and ethanol). Cleaned substrates were stored in pure ethanol.

TiO_2 underlayer: see chapter 3.3.1

Nanocrystalline TiO_2 layers:

Screenprintable TiO_2 pastes were employed (preparation see reference[8]) to print 1 cm broad TiO_2 stripes onto the substrate. Before sintering the printed films were left to equilibrate for about 30 minutes .

The sintering step was performed on a temperature-controlled hotplate under a constant flux of oxygen.

Sintering program:

Ramp of 5 min. to 70°C (kept for 20 min)
Ramp of 15 min to 120°C (kept for 20 min)
Ramp of 15 min to 400°C (kept for 40 min)
Cooling down (about one hour)

TiO_2 films of different thickness could be realized using appropriate screens in combination with pastes with appropriate TiO_2 contents. If not otherwise

specified no scattering particles were added to the TiO_2 pastes and the films obtained where highly transparent.

$TiCl_4$ treatment

If not otherwise specified the TiO_2 films were subject to a $TiCl_4$ treatment:

50 μl/cm^2 of a 0.02 M $TiCl_4$ solution were applied to the nanocrystalline film for 12 hours at room temperature. Afterwards the samples were washed with a large amount of distilled water and sintered for a second time:

Sintering program:
Ramp of 10 min. to 440°C (kept for 5 min)
Cooling down (about one hour)

Prior to the final assembly of the solar cells the TiO_2 films were stored in a dessicator over silica gel.

Dye uptake

Typically the nanocrystalline TiO_2 films were soaked in the corresponding dye solution for 24 hours in the dark prior to the spin coating process.

Spin-coating

The samples were removed from the dye solution, washed in the same solvent which was used for the dye uptake and dried under an argon flow.

100 –150 μl of spincoating solution were applied to the sample and a thin film was formed by rotating the sample at 1000 rev./min for 30 seconds (acceleration: 200 rev./min per second).

The samples were dried in air for a time period of one to two hours before being transferred into a vacuum chamber to apply a thin gold layer via thermal

evaporation. Prior to this the optical properties of the samples were characterized by UV/VIS spectroscopy using an integrating sphere.

Gold evaporation:

For the gold deposition the samples were placed inside the vacuum chamber of an evaporator (model *auto 306 turbo*; Edwards High Vacuum International/England). The evaporation was performed once the pressure dropped below 5×10^{-6} mbar. Evaporation rates were 0.1 – 0.2 nm/s for the first 2 nm and 0.5 – 0.7 nm/s until the desired layer thickness was reached. A metal mask was used to mask the areas on the sample. A glass blank was also subject to the evaporation process. Its optical characteristics were determined by UV/VIS spectroscopy (using an integrating sphere), in order to to estimate both, the optical loss when the solar cells were operated in the backside illumination mode, and the reflection, when the solar cells were operated in frontside illumination mode.

References

1)	Besocke, K.; Berger, S. *Rev. Sci. Instrum.* **1976**, *47*, 840-842.

2)	Moons, E.; Goossens, A.; Savenije, T. *J. Phys. Chem. B.* **1997**, *Vol 101, Iss 42*, 8492-8498.

3)	Kavan, L.; Grätzel, M. *Electrochim Acta* **1995**, *40*, 643.

4)	Smestad, G.; Silva, A. D.; Tributsch, H.; Fiechter, S.; Kunst, M.; Meziani, N.; Birkholz, M. *Solar Energy Mater.* **1998**, *18*, 299-313.

5)	Yanagi, H.; Ohoka, Y.; Hishiki, T.; Ajito, K.; Fujishima, A. *Appl. Surf. Sci.* **1997**, *113/114*, 426-431.

6)	Seaman, C. H. *Solar Energy* **1982**, *29*, 291-298.

7)	Planta, C. v. *Die photoelektrische Charakterisierung der mit Farbstoff sensibilisierten nanokristallinen Solarzelle*; Ecole Polytechnique Fédéral de Lausanne: Lausanne, 1996.

8)	Barbé, C. J.; Arendse, F.; Comte, P.; Jirousek, M.; Lenzmann, F.; Shklover, V.; Grätzel, M. *J. Am. Ceram. Soc.* **1997**, *80*, 3157.

Chapter 4

Spiro-OMeTAD

4.1 General properties
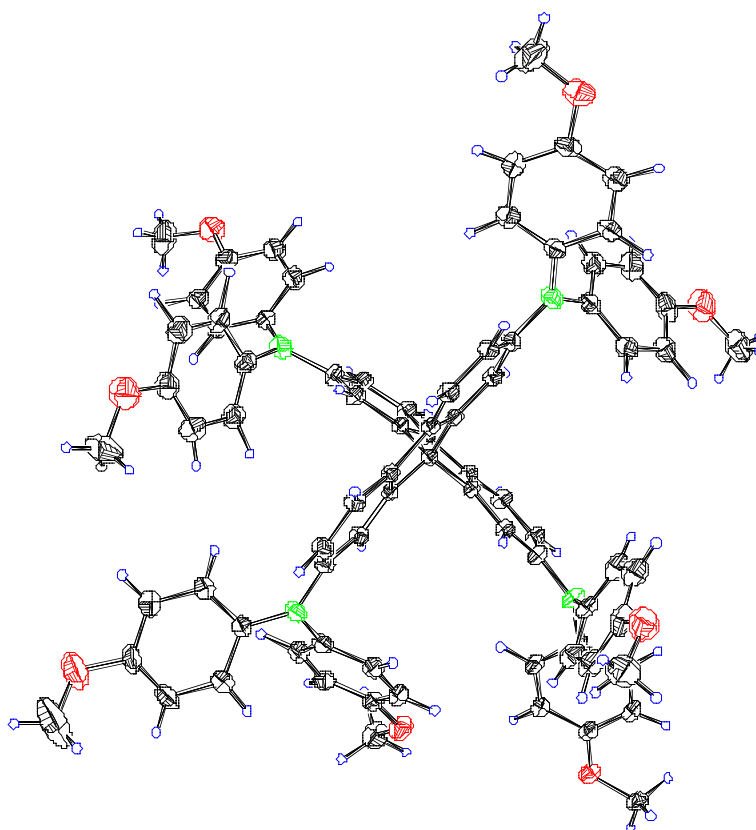
Figure 4.1. 3D-structure of 2,2',7,7'-tetrakis(N,N-di-*p*-methoxyphenyl-amine)-9,9'-spirobifluorene (*spiro*-OMeTAD) derived from x-ray structure analysis of a *spiro*-OMeTAD crystal.

4.1.1 Stability of the amorphous state:

A glass transition temperature of 121 °C was determined for *spiro*-OMeTAD by differential scanning calorimetry. In general, dimerisation of molecular hole conductors via a *spiro*-center showed substantial improvement of their thermal stability (see table 4.1). Thin films of *spiro*-OMeTAD , which were spincoated on glass did not show any sign of crystallization even after storing them for 2 years at room temperature. In contrast to this films of N,N'-diphenyl-N,N'-bis(3-methylphenyl)-1,1'-biphenyl-4,4'diamine (TPD), prepared under similar conditions clouded over after several weeks and were completely opaque after two years.

Substance	Tg	mp.
Spiro-OMeTAD	121 °C	246 °C
TPD	62 °C	167 °C
Spiro-TPD	115 °C	234 °C

Table 4.1 Glass transition temperatures determined via differential scanning calorimetry and melting points of *spiro*-OMeTAD and two other hole conducting substances[1].

4.1.2 Optical properties

The absorption spectrum of *spiro*-OMeTAD in solution is shown in Figure 4.2. Thin *spiro*-OMeTAD films of a few micrometers exhibit a faint yellowish color. The maximum of the fluorescence spectrum in CH_2Cl_2 solution lies at 424 nm (fluorescence quantum efficiency: 57%)[2].
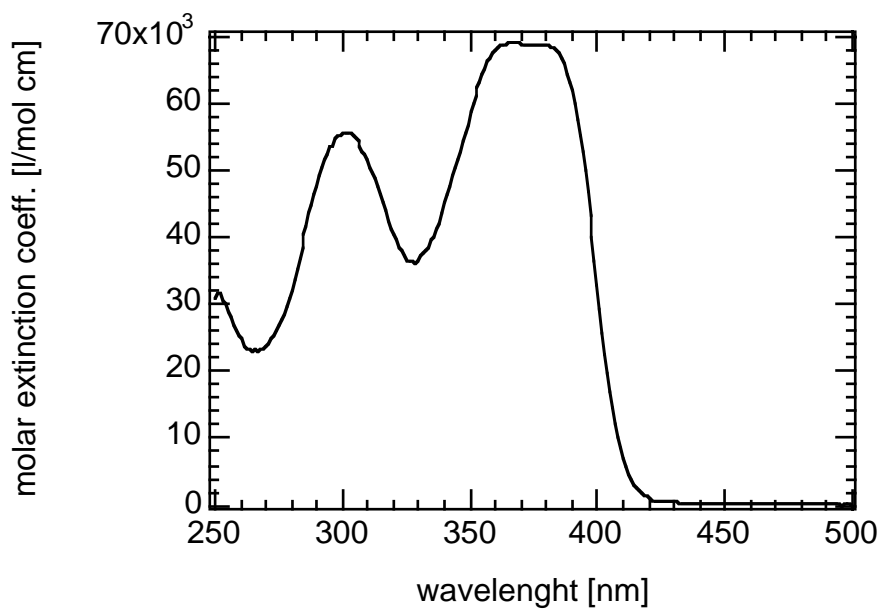
Figure 4.2 Optical absorption of *spiro*-OMeTAD in chlorobenzene.
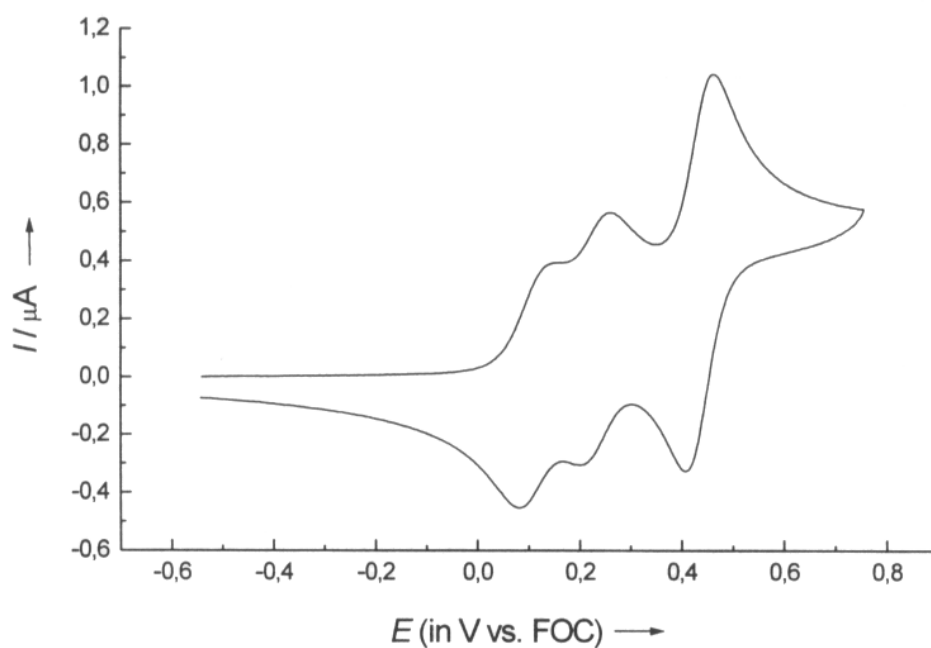
Figure 4.3 Cyclic voltammogram of *spiro*-OMeTAD in CH_2Cl_2 / 0.1 M $[N(n\text{-}C_4H_9)_4](PF_6)$ in dichloromethane versus $[Fe^{II}(Cp)_2/Fe^{III}(Cp)_2]$ at room temperature; scan rate 100 mV/s.

4.1.3   Electrochemistry

Figure 4.3 shows the cyclic voltammogram of *spiro*-OMeTAD in dichloromethane. The reference is the ferrocene redox couple (the redox potential of ferrocene $E[Fe^{II}(Cp)_2/Fe^{III}(Cp)_2]$ in organic solvents is typically 700 mV vs. NHE). Two one-electron oxidations and a two electron oxidation can be observed at 118 (1e$^-$), 232 (1e$^-$) and 436 mV (2e$^-$) vs. ferrocene (respectively 818, 932 and 1136 mV vs NHE). Each oxidation wave is fully reversible on the time scale of the experiment.

4.2   Charge transport in doped films

The conductivity of pure *spiro*-OMeTAD films is very low. For a 2 µm thick film of *spiro*-OMeTAD resistances of several $M\Omega/cm^2$ can be measured. The intrinsic state of this material can therefore not be used as hole conductor in solar cells, which typically have thicknesses of several microns and generate current densities of several mA/cm^2. Experiments confirmed this assumption, indicating that the photodoping of the organic charge transport material is not sufficient to support high current densities. The conductivity κ itself is a function of the charge carrier mobility µ and the charge carrier density N_h (e = 1.6022 x 10^{-19} C):

$$\kappa = \mu \; N_h \; e \qquad\qquad\qquad (4.1)$$

While the mobility of a pure material is a given material constant the charge carrier density can easily be controlled via doping. This concept is long known and is generally applied to improve the performance of organic thin film solar cells[3-5].

4.2.1   Doping with [N(*p*-C$_6$H$_4$Br)$_3$][SbCl$_6$]

Abkowitz and Pai[6] found a way to continuously increase the dark conductivity of TPD by progressive chemical incorporation of the TPD radical cation. These radical cations are produced by the one-electron transfer oxidation of TPD using tris(p-bromophenyl)ammoniumyl hexachloroantimonate [N(*p*-C$_6$H$_4$Br)$_3$][SbCl$_6$]. In this work it was found that *spiro*-OMeTAD films can be doped accordingly. The chemical reaction proceeding is:

[N(*p*-C$_6$H$_4$Br)$_3$]$^+$ [SbCl$_6$]$^-$ + *spiro*-OMeTAD

$$\longrightarrow \quad spiro\text{-OMeTAD}^+ + [\text{SbCl}_6]^- + [\text{N}(p\text{-C}_6\text{H}_4\text{Br})_3] \qquad (4.2)$$
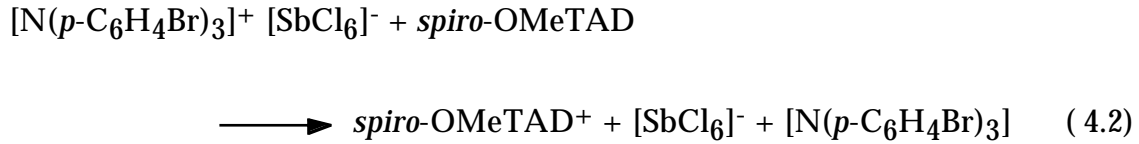
Figure 4.4 shows the current-voltage characteristics of two *spiro*-OMeTAD films, sandwiched between two ohmic contacts. While the undoped film does not show any significant conductivity on the mA/cm^2 scale, introduction of 0.18 mol % [N(*p*-C$_6$H$_4$Br)$_3$][SbCl$_6$] to the spin-coating solution prior to the film formation increased the conductivity by many orders of magnitude.

From the surface area and the thickness of the device one can determine the charge carrier mobility via:

$$\mu = \frac{\kappa}{N_e \cdot e} = \frac{l}{R \cdot A \cdot N_e \cdot e} \qquad (4.3)$$

R = series resistance of the device

A = surface area of the device

l = thickness of the *spiro*-OMeTAD layer
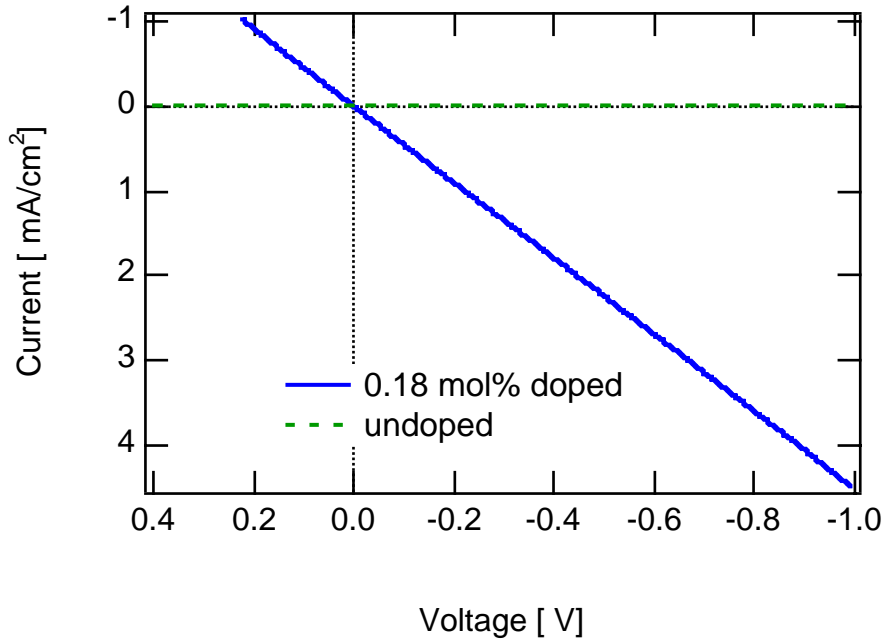
Figure 4.4 Current-voltage characteristics of thin *spiro*-OMeTAD films, sandwiched between a SnO_2 and a gold electrode. One of the films was doped by adding 0.18 mol % [N(p-C$_6$H$_4$Br)$_3$][SbCl$_6$] to the spin-coating solution (full line).

A doping concentration of 0.18 % translates into a charge carrier concentration N_h of 1.08×10^{18} holes/cm^3. From the thickness (2 μm) and the current-density of the device at –1 V (5 mA/cm^2) one can derive a hole mobility of 1.5×10^{-6} cm^2/Vs. Doping of the *spiro*-OMeTAD bulk also introduces an anion concentration of 1.08×10^{24} m^{-3}. These anions disturb charge transport through the bulk, so that the hole mobility inside an undoped film can be expected to be significantly higher. However in view of a final practical application the mobility in the *doped* system is much more relevant. It has to be pointed out that the presented mobility estimation is only of a preliminary nature, neglecting possible charge injection barriers at the contacting interfaces. Four-point measurement techniques like the van der Pauw method[7] are more suitable to probe the contribution of the bulk to the overall resistively of the sample. Furthermore the temperature dependent analysis of the conductivity could help to reveal the mechanism of charge transport. However these studies could not be realized in the time frame of this work.

The doping proved to be reasonably stable over a long period. The decrease in conductivity of an unsealed $[N(p\text{-}C_6H_4Br)_3][SbCl_6]$ doped sample, exposed to ambient oxygen and moisture was less than 10 % over a period of three weeks and about 50 % over a period of two years. Substantial increase in stability should further be gained by encapsulation of the device or by use of a more stable counterion. Further evidence is given in chapter 5.

4.2.2   Influence of the purity on the conductivity of doped films

The conductivity properties of two different batches of OMeTAD were compared. One (synthesized in a 100g batch at Aventis[©]) was classified as 99.7% pure according to HPLC analysis while a second refined batch with >99.9% was used for comparison. Thin $[N(p\text{-}C_6H_4Br)_3][SbCl_6]$ doped films of *spiro*-OMeTAD on SnO_2 were made via the classical spin coating procedure and thin gold contacts evaporated on top. The resistances measured for both devices did not show any significant difference (576 ± 2 Ω/cm^2 for 99.7 % and 586 ± 7 Ω/cm^2 for 99.9 %+), indicating that the impurity level does not influence the charge transport characteristics of the doped layer. This observation stands in contrast to what is generally observed for intrinsic organic semiconductor applications (xerography, OLEDs) where material purity has a major influence on the device properties down to impurity concentrations of much less than 0,1 %[3]. This is most likely due to the fact that minor impurities, representing deep traps, will trap a considerable fraction of those few charge carriers present in an *undoped* device under space-charge limited current conditions, while in a *doped* device they will only reduce the concentration of charge carriers introduced via chemical doping, which is much higher than the concentration of the deep trap impurities themselves. An important consequence from this observation is that no sophisticated purification steps are necessary to obtain applicable materials for device manufacture, keeping production costs low.

### 4.2.3   Higher oxidation states of *spiro*-OMeTAD

All four oxidation states of *spiro*-OMeTAD can be obtained via chemical oxidation with $[N(p\text{-}C_6H_4Br)_3][SbCl_6]$. Figure 4.5 shows the spectral changes induced by addition of small aliquots of a $[N(p\text{-}C_6H_4Br)_3][SbCl_6]$ solution. Each *spiro*-OMeTAD molecule contains two identical, mutually perpendicular π-systems. The electronic interaction of the two moieties should therefore be small and the spectrum of *spiro*-OMeTAD^{2+} should show the same basic features, except that its molar extinction coefficient should be twice that of *spiro*-OMeTAD$^+$. Accordingly one can observe the steady rise of a new absorption bands at 511 nm and a shoulder around 700 nm, which grow as the absorption peak of the neutral compound at 380 nm decreases to a faint shoulder. Upon addition of more than 2 equivalents of $[N(p\text{-}C_6H_4Br)_3][SbCl_6]$ (Figure 4.5b) the new absorption peak at 510 nm decreases in favor of an absorption peak at 690 nm, which arises from the former shoulder, and a further new absorption peak around 900 nm. These findings are in excellent agreement with spectroelectrochemical data reported elsewhere[2]. According to this reference the diradical cation of *spiro*-OMeTAD shows absorption maxima in CHCl$_3$ at 511 nm ($\varepsilon = 40100$) and 1400 nm ($\varepsilon = 32200$; not shown) while *spiro*-OMeTAD^{4+} exhibits an absorption maximum at 865 nm ($\varepsilon = 118000$). A further indication of a clean oxidation process is the presence of perfect isosbestic points in both graphs.

a)

b)
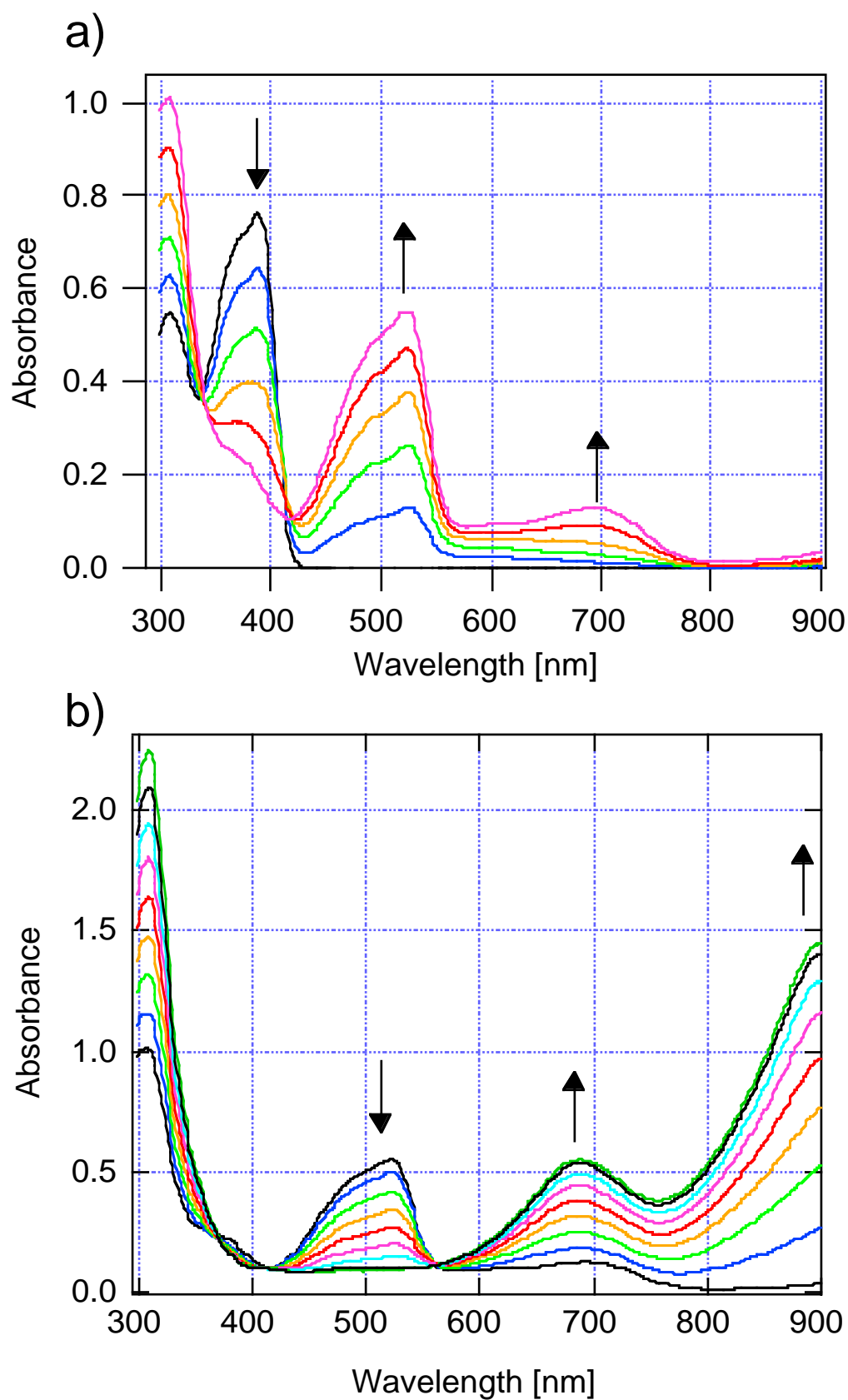
Figure 4.5 Stepwise oxidation of a 1.05 x 10^{-5} M *spiro*-OMeTAD solution with [N(*p*-C$_6$H$_4$Br)$_3$][SbCl$_6$]. a) Formation of *spiro*-OMeTAD^{2+} from *spiro*-OMeTAD. b) formation of *spiro*-OMeTAD^{4+} from *spiro*-OMeTAD^{2+}.

4.2.4   Doping with benzoquinone and iodine

Another class of dopants, which are successfully used to achieve p-doping are benzoquinones. The conductivity of 2,3-Dichloro-5,6-dicyano-1,4-benzoquinone doped films showed to be about a factor of 3 smaller than $[N(p\text{-}C_6H_4Br)_3][SbCl_6]$ doped films with the same molar doping level. This despite the fact that benzoquinones are two-electron acceptor. Addition of 2,3-dichloro-5,6-dicyano-1,4-benzoquinone to a solution of *spiro*-OMeTAD gave rise to the typical dark-red color, which is observed upon its oxidation with $[N(p\text{-}C_6H_4Br)_3][SbCl_6]$. However, when diluted solutions containing a 1:1 molar ratio of *spiro*-OMeTAD and 2,3-Dichloro-5,6-dicyano-1,4-benzoquinone were spread out on a surface a dramatic increase in the overall absorption was observed when the solvent evaporated from the solution.
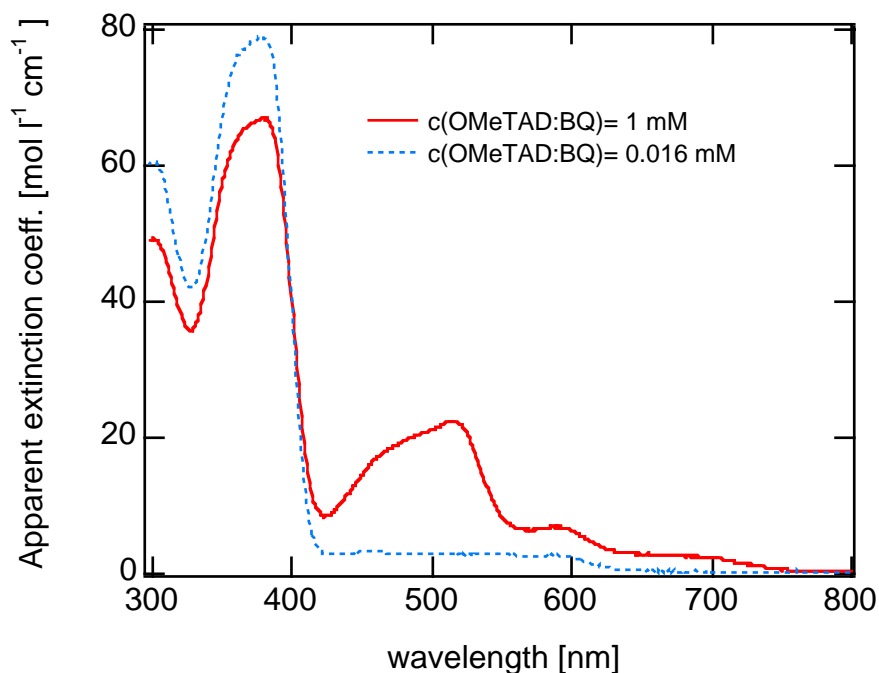
Figure 4.6 Apparent extinction coefficient measured for a 1:1 molar mixture of *spiro*-OMeTAD and 2,3-Dichloro-5,6-dicyano-1,4-benzoquinone for different concentrations. A 80:20 mixture of acetonitrile:chlorobenzene was used as solvent.

This effect could be verified by measuring the UV/VIS spectra of *spiro*-OMeTAD : benzoquinone (1:1) solutions of different concentrations. In Figure 4.6

two different examples are given. To illustrate the spectral change the *apparent* molar extinction coefficient of the 'adduct' *spiro*-OMeTAD : benzoquinone are shown – neglecting that the redox reaction or adduct formation might be incomplete. Figure 4.7 shows the apparent extinction coefficient of the absorption peak at 515 nm, which is congruent with the absorption peak of *spiro*-OMeTAD$^+$, as a function of the concentration. The disappearance of the 515 nm absorption can be observed on dilution of the solution, indicating that dilution induces a shift of the chemical equilibrium. Two possible equilibrium reactions might proceed: an incomplete oxidation reaction (a) or the formation of a charge transfer (CT) complex of *spiro*-OMeTAD and the benzoquinone (BQ) (b).
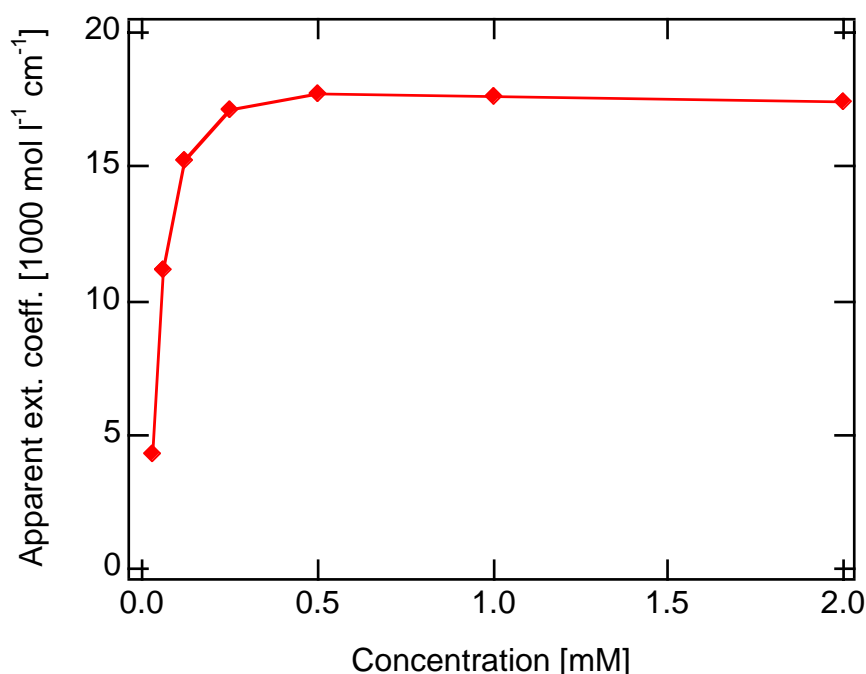
Figure 4.7 Apparent extinction coefficient of the absorption peak at 515 nm, measured for a 1:1 molar mixture of *spiro*-OMeTAD and 2,3-Dichloro-5,6-dicyano-1,4-benzoquinone for different concentrations. A 80:20 mixture of acetonitrile:chlorobenzene was used as solvent.

Spiro-OMeTAD + BQ $\rightleftarrows$ *spiro*-OMeTAD$^+$ + BQ$^-$ (a)

$$K = \frac{[OMeTAD^+] \cdot [BQ^-]}{[OMeTAD] \cdot [BQ]}$$

Spiro-OMeTAD + BQ $\rightleftarrows$ *spiro*-OMeTAD : BQ (b)
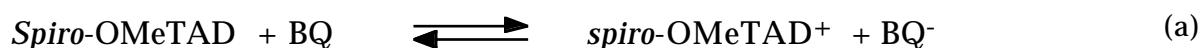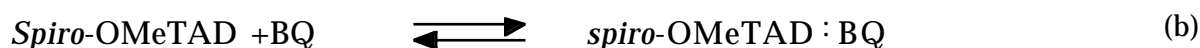
$$K = \frac{[OMeTAD:BQ]}{[OMeTAD] \cdot [BQ]}$$

As can be seen from above equations the back reaction is of second order in the case of the oxidation reaction (a), while it is of first order in case of the dissociation of a CT complex (b). As a consequence the two reactions can be distinguished upon their behavior upon dilution. 50 % dilution of system (a) will introduce a factor 0.5^2 in the numerator as well as in the denominator of equation (a). The system stays in equilibrium. In the case of the CT complex formation, K will change upon a 50 % dilution by a factor $0.5/0.5^2 = 2$; the system is out of its equilibrium. Subsequently some of the CT-complex will dissociate in order to reach equilibrium conditions. As a consequence the ratio of [*spiro*-OMeTAD$^+$] : [*spiro*-OMeTAD] decreases upon dilution for reaction (b), while it stays constant in case of reaction (a).

The spectral observations therefore suggest that doping of *spiro*-OMeTAD with 2,3-dichloro-5,6-dicyano-1,4-benzoquinone is based on the formation of the charge transfer complex. The reaction equilibrium was also not affected by the presence or absence of protons, which determine the redox potential of benzoquinones.

The conductivity of *spiro*-OMeTAD films, doped with I_2 also showed to be about a factor of 4 smaller, than that of [N(p-C$_6$H$_4$Br)$_3$][SbCl$_6$] doped films with the same molar doping level. The underlying doping mechanism was therefore no longer examined.

4.2.5 Doping with *spiro*-OMeTAD^{++}[PF$_6^-$]$_2$

Due to some concern about the stability of the SbCl$_6^-$ ion and the [N(p-C$_6$H$_4$Br)$_3$] in [N(p-C$_6$H$_4$Br)$_3$][SbCl$_6$] doped films a pure form of the hexafluorophosphate salt of *spiro*-OMeTAD^{++} was synthesized and isolated (see experimental). The diradical cation was chosen, as it was easier to isolate in a crystalline form then the monoradical cation. The two positive charges are located on the two different benzidine moieties of the *spiro*-OMeTAD molecule. Interaction of the two chromophoric systems is therefore very weak. This is confirmed by the

observation that no change in the VIS absorption (> 420 nm) is observed upon addition of *spiro*-OMeTAD to a solution of *spiro*-OMeTAD^{++}[PF$_6^-$]$_2$.

As will be seen in the following chapter thin films of *spiro*-OMeTAD doped with *spiro*-OMeTAD^{++}[PF$_6^-$]$_2$ show a very slow 'recovery behavior' after the evaporation of the gold layer. However, the conductivity of *spiro*-OMeTAD^{++}[PF$_6^-$]$_2$ doped films was found to be equal to those of [N(p-C$_6$H$_4$Br)$_3$][SbCl$_6$] doped films.

A major advantage of *spiro*-OMeTAD^{++}[PF$_6^-$]$_2$ is its inertness towards the presence of lithium salts, which is a prerequisite for high efficiency solid-state solar cells. Spincoating solutions of *spiro*-OMeTAD containing Li[(CF$_3$SO$_2$)$_2$N] and [N(p-C$_6$H$_4$Br)$_3$][SbCl$_6$] darkened with time, suggesting that a slow oxidation of *spiro*-OMeTAD proceeded after the spin-coating solution was prepared. This can be seen in graph 4.8, showing the time dependence of the peak absorption of *spiro*-OMeTAD$^+$ in Li$^+$ containing chlorobenzene/acetonitrile solutions of *spiro*-OMeTAD. Both solutions shown contain the same oxidation equivalents – which is supposed to be one for each ([N(p-C$_6$H$_4$Br)$_3$][SbCl$_6$] molecule and two for each *spiro*-OMeTAD^{++}[PF$_6^-$]$_2$ molecule. In *absence* of the lithium salt both solutions indeed showed the same initial adsorption of 0.61 which after 48 hours changed to 0.67 when doped with [N(p-C$_6$H$_4$Br)$_3$][SbCl$_6$] and to 0.57 when doped with *spiro*-OMeTAD^{++}[PF$_6^-$]$_2$. In the *presence* of the lithium salt the time dependence of the peak adsorption is dramatically different, depending on the dopant used. The presence of lithium ions catalyzed a subsequent slower oxidation process in the presence of [N(p-C$_6$H$_4$Br)$_3$][SbCl$_6$], which proceeds on the time scale of one hour. This results in a peak adsorption, which is about three times that of its initial value (0.60). The relative spectral shape of the UV/VIS absorption did not change upon this reaction, indicating that the change in absorptivity is due to an additional formation of *spiro*-OMeTAD$^+$.

Similar results were obtained, when other lithium salts like LiClO$_4$ were used instead of Li[(CF$_3$SO$_2$)$_2$N]. However, when *spiro*-OMeTAD^{++}[PF$_6^-$]$_2$ is used as
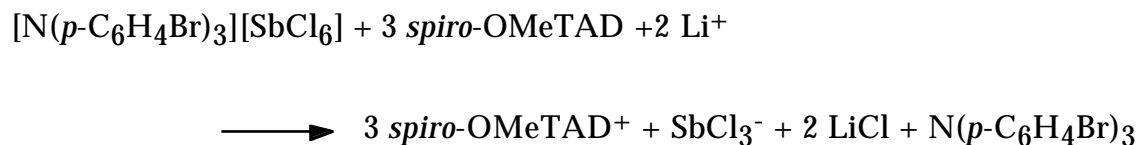
dopant no subsequent oxidation process can be observed in presence of lithium. Control experiments also showed that no oxidation products of *spiro*-OMeTAD could be detected after 48 hours, when $Li[(CF_3SO_2)_2N]$ was added to a *spiro*-OMeTAD solution in absence of dopants. These observations suggest that the $SbCl_6^-$ counterion might act as an oxidizing agent. A linear time dependence was observed when the logarithm of [peak absorption(t) - final peak absorption(t=∞)]was plotted against the reaction time, indicating that the proceeding reaction is of first order. This is as expected for an oxidation process involving $SbCl_6^-$ in a large (20fold) excess of *spiro*-OMeTAD.
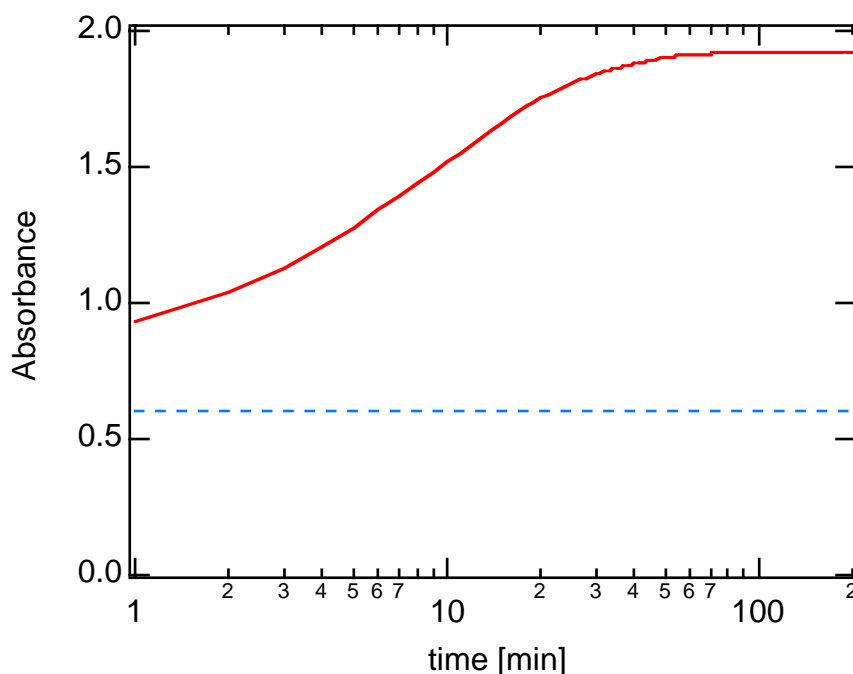
Figure 4.8 Time development of the *spiro*-OMeTAD$^+$ peak absorption (523 nm) of two different solutions. Solution a) (dotted line) contained *spiro*-OMeTAD^{++}[PF$_6^-$]$_2$ (1.07 x 10^{-5} M) and an excess of *spiro*-OMeTAD (2.35 x 10^{-4} M), and $Li[(CF_3SO_2)_2N]$ (15 mM) in chlorobenzene (+ 5 % acetonitrile). The absorption was stable over the observed time range. Solution b) (plain line) contained [N(*p*-C$_6$H$_4$Br)$_3$][SbCl$_6$] (2.13 x 10^{-5} M) and an excess of *spiro*-OMeTAD (2.35 x 10^{-4} M), and $Li[(CF_3SO_2)_2N]$ (15 mM) in chlorobenzene (+ 5 % acetonitrile). The initial absorption immediately after mixing the starting materials was measured to be 0.64. Due to the configuration of the data acquisition program the initial steep rise of the absorption is not shown in this graph.

The redox, hydrolysis and coordination chemistry of Sb(V) halides is very complex[8]. In organic chemistry they are known to be strong chlorination agents[9]. The $SbCl_6^-$ ion is therefore likely to be a source of two additional redox

equivalents. Lithium might catalyze this reaction by withdrawing chloride ions out of the chemical equilibrium:

$[N(p\text{-}C_6H_4Br)_3][SbCl_6]$ + 3 *spiro*-OMeTAD +2 Li^+

$$\longrightarrow \quad 3 \text{ } spiro\text{-OMeTAD}^+ + SbCl_3^- + 2 \text{ LiCl} + N(p\text{-}C_6H_4Br)_3$$

The formation of $SbCl_3^-$ gives rise to further concerns, as it is known to form strong adducts with bipyridyls[9]. For the sake of the stability of the ruthenium(II)bipyridyl sensitizers it is therefore not desirable to contaminate the cell with antimony compounds.

4.2.6   EPR-spectra of *spiro*-OMeTAD$^+$ and *spiro*-OMeTAD^{++}

EPR spectra were recorded to characterize *spiro*-OMeTAD$^{++}[PF_6^-]_2$. Comparison of Figure 4.9 a) and b) reveal a somewhat similar hyperfinestructure for TPD$^+$ and *spiro*-OMeTAD^{++}, exhibiting a sequence of three positive and three negative peaks which are comparable in height. Comparison of spectra i) and ii) (Figure 4.9a) suggests that the TPD$^+$ spectrum can be rationalized on the basis of the hyperfine coupling of two nitrogen nuclei (a_N = 4.45 G) and an unresolved proton couplings with Gaussian line shape of ΔH_{pp} = 4.15 G. From the peak-to-peak distance in the spectrum of *spiro*-OMeTAD^{++} we derive a hyperfine coupling constant of a_N = 2.35 G . The lower coupling constant of the nitrogen nuclei in *spiro*-OMeTAD^{++} might be rationalized in terms of a stronger delocalization of the spin density due to the electron withdrawing properties of the methoxy substituents. The poorer resolution of the hyperfine structure in the *spiro*-OMeTAD spectrum is mainly due to the weaker coupling.

When an equimolar amount of *spiro*-OMeTAD is added to a solution of *spiro*-OMeTAD^{++} the basic spectral features do not change significantly, suggesting that the two orthogonal spin systems in *spiro*-OMeTAD do not significantly interact. For both systems (*spiro*-OMeTAD^{++} and *spiro*-OMeTAD$^+$) degassing of the

sample by bubbling with argon was essential to resolve the hyperfine structure, indicating that the presence of molecular oxygen dissolved in acetonitrile causes a significant line broadening. The hyperfine structure also remained unresolved in more concentrated solutions of *spiro*-OMeTAD (c = 3.3 10^{-2} M). The same effect was observed for TPD[+] and explained by motional exchange narrowing. In *spiro*-OMeTAD[++] electron-electron interaction of the spins located in direct vicinity on the two molecule moieties might lead to an additional contribution to the homogenous line broadening, while in *spiro*-OMeTAD[+] this could be caused by fast hole exchange between the two π-systems. However the contribution of these effects seems to be minor, as no significant increase in linewidth could be observed, compared to TPD[+].
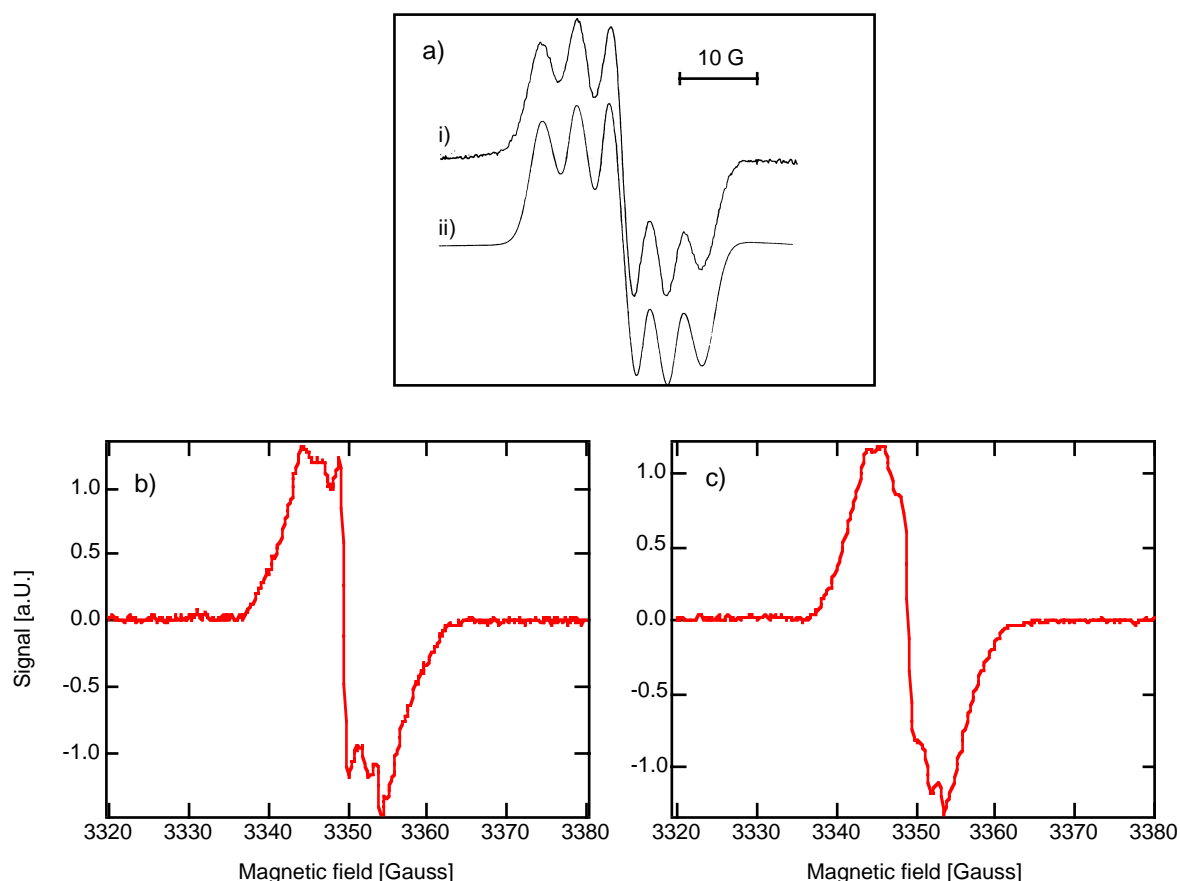
Figure 4.9 a) ESR spectrum of TPD[+] in diluted dichloromethane solution at room temperature, according to reference[10]. Spectrum i) as measured ([TPD] = 8*10-3 M; [TPD[+]] = 8 10-4 M) and spectrum ii) as simulated with hyperfine couplings to two nitrogen nuclei: a_N = 4.45 G and unresolved proton couplings with Gaussian line shape of ΔH_{pp} = 4.15 G. b): ESR spectrum of OMeTAD[++]$(PF_6)_2$ in acetonitrile (c = 3.3 10^{-4} M, modulation amplitude = 0.3 G, T = 295 K)
    c) ESR spectrum of OMeTAD[+]$(PF_6)_2$ in acetonitrile (c = 6.6 10^{-4} M, modulation amplitude = 0.5 G, T = 295 K).

References

1) Weissörtel, F. Synthese und Charakterisierung spiroverknüpfter niedermolecularer Gläser für optoelektronische Anwendungen; University of Regensburg: Regensburg, 1999.

2) Weissörtel, F. Amorphe niedermolekulare Ladungstransportmaterialien für nanokristalline Solarzellen, Diplomarbeit; Universität Regensburg:, 1996.

3) Meier, H. Organic Semiconductors; Verlag Chemie: Weinheim, 1974.

4) Yamashita, K.; Harima, Y.; Matsubayashi, T. J. Phys. Chem. **1998**, 1989, 5311-5315.

5) Hiramoto, M.; Kishigami, Y.; Yokoyama, M. Chem. Lett. **1990**, 119-122.

6) Abkowitz, M.; Pai, D. M. Phil. Mag. B **1986**, 53, 193.

7) Pauw, L. J. v. d. Phil. Res. Rep. **1958**, 13, 1-9.

8) Baila, J. C. Comprehensive Inorganic Chemistry; Pergamon Press: Oxford, 1973; Vol. 2, pp 547-685.

9) Holleman-Wiberg Lehrbuch der anorganischen Chemie; Walter de Gruyter: Berlin, 1976; Vol. Berlin, pp 480-482.

10) Veregin, R. P.; Harbour, J. R. J. Phys. Chem. **1990**, 94, 6231-6237.

Chapter 5

Contact behavior of *spiro*-OMeTAD

5.1 The necessity of rectifying contacts

Materials used as charge collection electrodes for pn-heterojunctions have to fulfill different requirements. Ohmic contacts have to be formed between the anode and the n-type material, as well as between the cathode and the p-type material of the junction[2]. This is necessary to avoid injection barriers, impeding efficient charge collection. In addition to this, one of the materials needs to be at least semitransparent, acting as window material for the solar cell. In layered structures, where no contact between cathode and *n-type* material or anode and *p-type* material occurs these requirements are sufficient. However, as soon as such contacts exist with significant contact areas they need to be blocking in order to avoid internal short circuits. In nanocrystalline photoelectrochemical solar cells a large contact area exists between the iodine/iodide electrolyte and the contacting SnO_2 electrode. Fortunately iodine/iodide has a strong overpotential at SnO_2 glass, thereby avoiding an internal short circuit due to the reduction of iodine at the SnO_2 surface. Unfortunately *spiro*-OMeTAD and SnO_2 form a contact which is perfectly ohmic (see Figure 4.4). Formation of a nanocrystalline dye-sensitized heterojunction of *spiro*-OMeTAD and TiO_2 with SnO_2 as working electrode

---

[2] In the following the terms anode (working electrode) and cathode (counter electrode) shall be extended to the materials which *contact* the n- and p-type material.

material would therefore lead to an intrinsically inefficient solar cell device, as a large fraction of the photogenerated charge carriers would recombine at the SnO_2/*spiro*-OMeTAD interface.

Two alternative approaches can be pursued to solve this problem. The first one is to protect the transparent working electrode material with a thin film of TiO_2, thereby inhibiting direct contact of the hole conductor and the collecting electrode. This approach implies several advantages, as commercially available window material substrates like SnO_2 or ITO can be used, which combine excellent transparency over a wide spectral range with good electric conductivity.

The second approach is to replace the SnO_2 electrode with a material that exhibits a blocking contact to *spiro*-OMeTAD. Doped metal oxide films present themselves as excellent window materials for solar cells; however all of the tested samples (SnO_2, ITO or conducting ZnO glass) formed ohmic contacts to *spiro*-OMeTAD. Thin, semitransparent metal films forming Schottky contacts with *spiro*-OMeTAD might also be used as alternative anode window material. When a transparent counter electrode is used the solar cell might also be directly assembled on bulk metal substrates, a device architecture which might be very interesting for certain applications.

5.2. Blocking TiO_2 films

Different methods can be used to deposit thin compact films of TiO_2. Among those are reactive sputtering of titanium, sputtering of TiO_2, MOCVD[1], electrochemical deposition of titanium(III) precursors[2] or spray pyrolysis[3-5]. The coating of glass surfaces with thin (typically 50 nm thickness) TiO_2 films is a common industrial large scale process known as 'titanizing'. The main purpose of coating glass is to increase its physical strength, although TiO_2 coatings are sometimes applied to improve resistance to acids and alkalis or hot alkali vapour, to provide a heat reflecting layer or to absorb UV radiation[6]. Furthermore TiO_2

coatings are used as adhesion-promoting primers or as antireflection coatings[6]. The methods applied on an industrial scale can be classified as MOCVD or spray pyrolysis. These techniques are therefore of major interest in view of future series production of solid-state dye-sensitized solar cells, as the technical problems of large-scale production are solved and the process is cheap and fast.

Various methods can be applied to check the blocking character of thin TiO_2 films. Typically electrochemical methods like cyclic voltammetry are used to characterize the blocking properties of such films. However in view of its application in the solid-state dye-sensitized solar cell it is much more appropriate to directly form a diode of layered structure: [SnO_2/TiO_2(dense)/*spiro*-OMeTAD /Au] and to measure its current-voltage characteristic. As gold is known to form an ohmic contact the introduction of an efficient, pinhole free coating will be reflected in a classical diode behavior of the device. While the p-*spiro*-OMeTAD/n-TiO_2 heterojunction is blocking in reverse bias the diode current in the forward bias mode increases exponentially, until the cell current is limited by the ohmic resistances of the cell components.

5.2.1. Reactive sputtered TiO_2 layers

In a first attempt dense TiO_2 layers were formed via reactive sputtering in collaboration with Hoecht AG (Frankfurt/Germany). Films from 100 to 300 nm thickness were deposited onto SnO_2 glass (Asahi and LOF). Figure 5.1 shows the current-voltage characteristic of devices with and without a sputtered 200 nm TiO_2 layer.
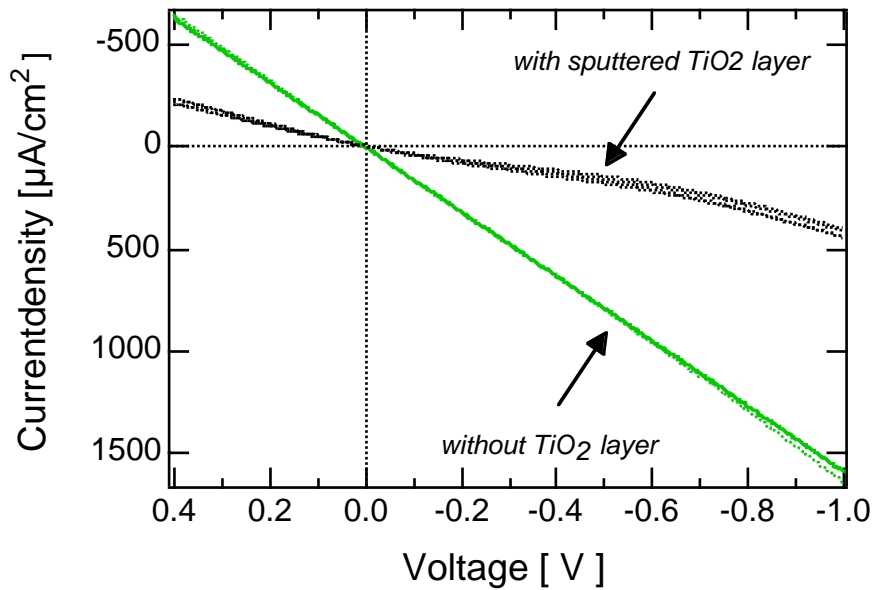
Figure 5.1 Current-voltage characteristics of SnO_2/TiO_2(sputtered)/*spiro*-OMeTAD/Au Schottky diodes in comparison to SnO_2/*spiro*-OMeTAD/Au devices of similar geometry. The TiO_2 layer was formed by a reactive sputtering process of titanium in presence of partial pressures of oxygen, yielding a TiO_2 layer of 200 nm thickness.

The introduction of the thin TiO_2 layer did not result in a notably rectifying behavior of the device. However it increased the ohmic resistance of the device by nearly a factor 4. This dramatic increase in series resistance is undesirable for the application in a solar cell. At higher thicknesses of the TiO_2 layer an increase in ohmic resistance was even more pronounced while the current-voltage characteristic did not reveal a significant rectification behavior. This can be explained by the presence of pinholes or cracks inside the TiO_2 layer, exposing bare SnO_2 to the spincoated film of *spiro*-OMeTAD. The presence of cracks on the nanometer scale was confirmed by transmission electron microscopy studies (see Figure 5.2). X-ray and STM analysis revealed the predominantly amorphous nature of the TiO_2 film, in the presence of some $3-10$ nm sized rutile nanoparticles.
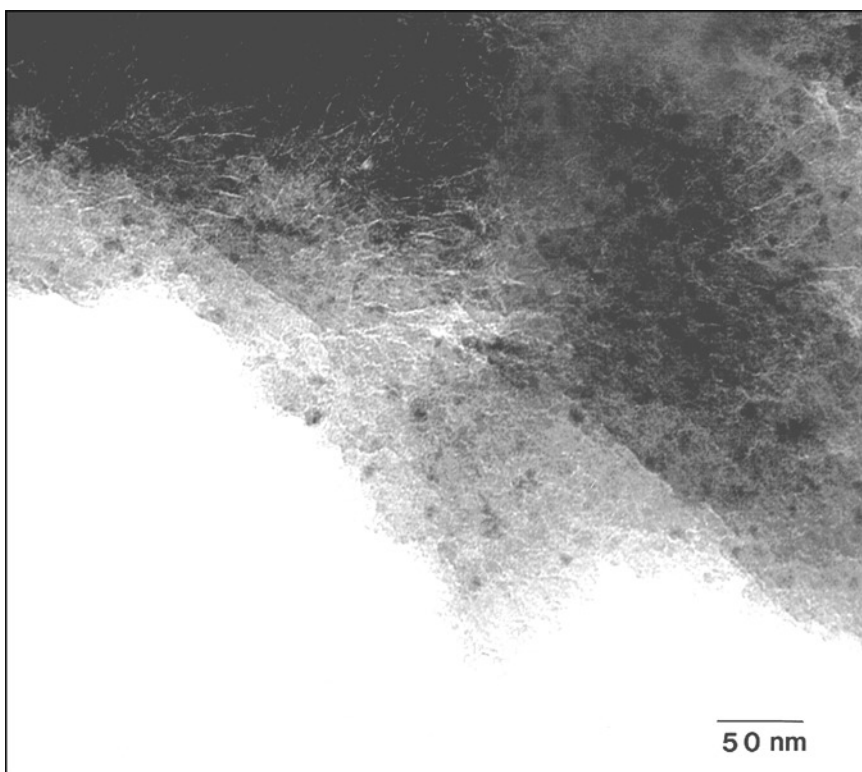
Figure 5.2 TEM microgaph of a reactively sputtered TiO_2 layer clearly showing a large number of cracks, with lengths of several tens of nm and widths in the nm range.

The attempt to form blocking TiO_2 layers via reactive sputtering of titanium was abandoned as soon as films made via spray pyrolysis showed to provide the desired diode behavior.

5.2.2   Dense TiO$_2$ layers made via spray pyrolysis

Kavan et al.[5] proposed a method to form thin films of TiO_2 on SnO_2 glass by pyrolysis of ethanolic solutions of di-iso-propoxy titanium-bis(acetylacetone) [$Ti(acac)_2(i-C_3H_7O)_2$] in aerosol form. Films formed via this method exhibited a highly rectifying character, when used in conjunction with *spiro*-OMeTAD. Rectifying properties in those junctions were excellent, with current densities in reverse bias of less than 100 nA/cm^2 (at 0.2 V), while the currents above –800 mV in the forward bias region were mainly limited by the ohmic resistance of the organic layer (see Figure 5.3). A striking feature of films made via this method is the good reproducibility of their electronic properties. This is even more

remarkable in view of the rather simple setup and the poor control of the preparation conditions (spraying angle, aerosol volume, gas flux, solution flux, etc.; see experimental). To illustrate this, 3x4 diode characteristics are shown, which represent TiO$_2$ layers that were made with three different numbers of repetitive spraying cycles (5x, 10x and 20x). Not only the 4 individual diode contacts of each sample coincide, but also the thickness of the as prepared film seems to leave the electronic properties of the junction unaltered. Similar to this insensitivity to the layer thickness, the deposition temperature proved to be uncritical for the electronic properties of the final heterojunction device in a range of 400 to 500 °C. This excellent reproducibility is a prerequisite to study small changes in the junction characteristics induced e.g. by surface modification with self assembled monolayers.
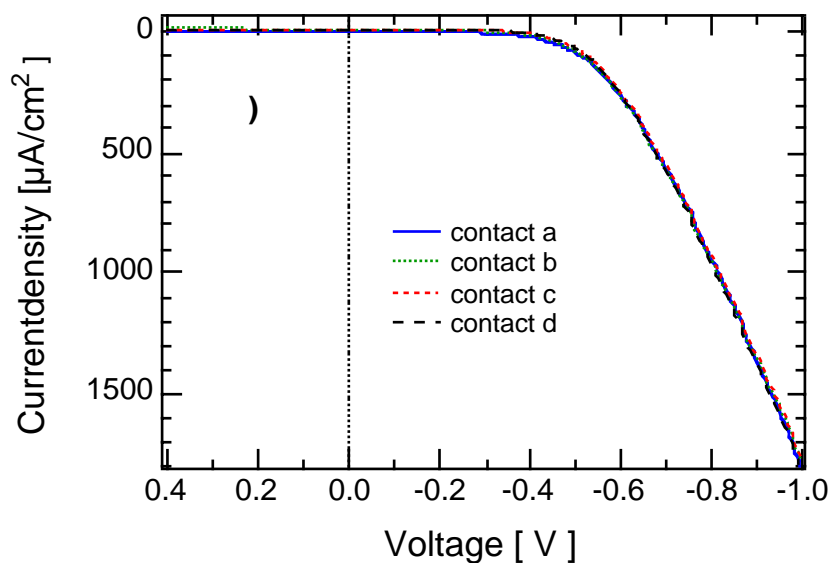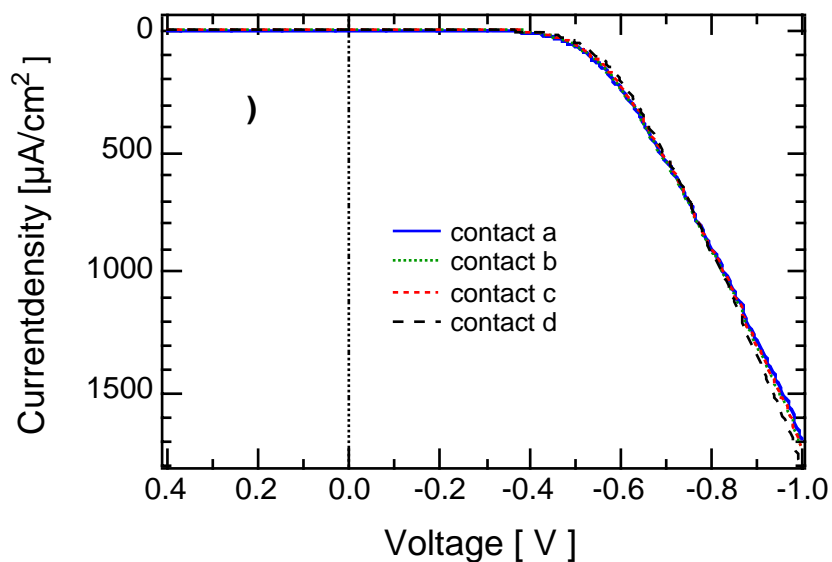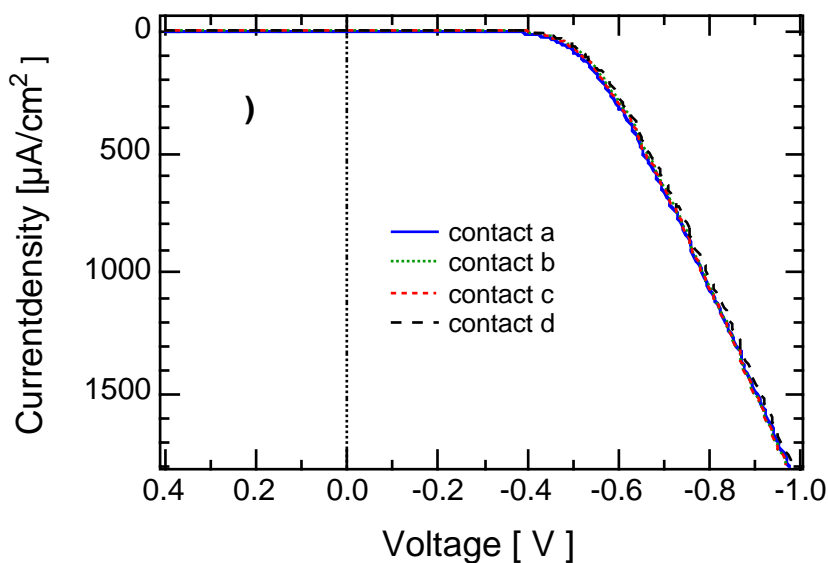
Figure 5.3 Current-voltage characteristics for three different devices of the structure SnO_2/TiO_2(spraypyr.)/*spiro*-OMeTAD/Au. Four individual electrodes were deposited on each device and characterized separately. The *spiro*-OMeTAD film was doped with 0.18 mol% [N(*p*-$C_6H_4Br)_3$][$SbCl_6$]. The TiO_2 films made from 5 (a), 10 (b) and 20 (c) consecutive spraying cycles, corresponding to layer thicknesses of about 30, 60 and 120 nm.

The TiO_2 layer properties were extensively analyzed via transmission electron microscopy, SEM, AFM, x-ray analysis and elipsometry. The films consisted of a compact assembly of anatase particles with diameters of typically 50 nm. Results from elipsometric measurements confirmed the density of the TiO_2 film to be identical with that of bulk anatase substrates. Figure 5.4 shows a typical AFM image of a spray pyrolysed TiO_2 layer on glass, which clearly reveals the polycrystalline nature of the film. These findings are in good correlation with similar experiments by Kavan et al.[5], who observed the formation of 49-56 nm anatase particles upon spray pyrolysis of a 0.2 M [Ti(acac)$_2$(i-$C_3H_7O)_2$] solution at a substrate temperature of 400 – 450 °C.
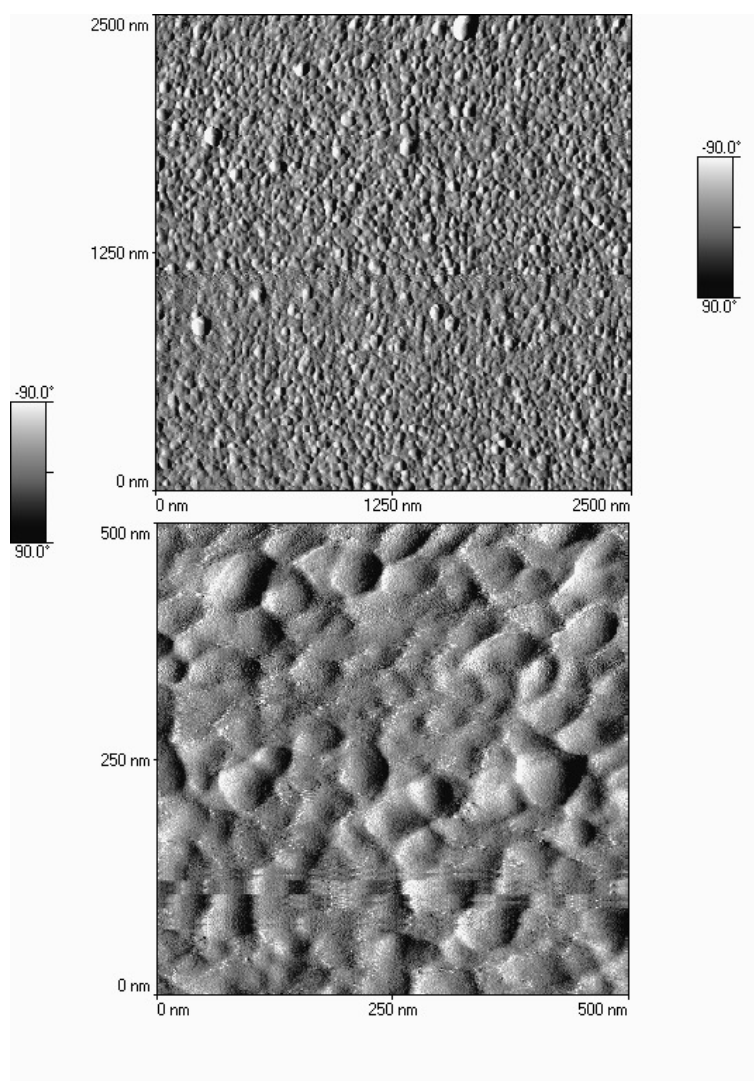
Figure 5.4 AFM micrograph of a TiO$_2$ layer on glass made via spray pyrolysis.

Spray pyrolysis using an ultrasonic nozzle

In order to get better control over the deposition parameters a spray pyrolysis set-up was developed, which allowed to control separately the precursor flux and the carrier gas flow, while the spraying direction and distance was kept constant (see experimental). About 100 individual diodes formed with TiO$_2$ layers prepared with this set-up were realized and characterized, spanning a wide range of layer thickness, deposition rates and precursor/reaction gas fluxes. Despite the strict control over the experimental parameters the so-prepared TiO$_2$/*spiro*-OMeTAD junctions did not result in reproducible current-voltage characteristics. Only four

out of 100 diodes showed a rectifying character comparable to those made via handheld spray pyrolysis. Differences might arise due to the difference in speed of the droplets heading towards the surface, which is significantly higher in case of the handheld device. Droplets might therefore reach the SnO_2 surface prior to their evaporation, while this might not be the case, when the ultrasonic nozzle is applied (also due to smaller droplet size). Another principal difference is that in case of the handheld device the exposure of the precursor solution to the surface is pulsed, while the alternative method represents a continuous process. Pulsed operation of the ultrasonic nozzle might give rise to more reproducible results. Also unclear is the role of water and oxygen in the pyrolysis process. Results from MOCVD of $Ti(acac)_2(i-C_3H_7O)_2$ vapors suggest that the presence of water and oxygen is indispensable for the formation of blocking TiO_2 layers (see below).

5.2.3   Dense TiO_2 layers made via MOCVD

The formation of thin TiO_2 layers via MOCVD of organic, volatile Ti(IV) compounds is a common technique to form thin TiO_2-layers on an industrial scale ('titanizing') and has been extensively described in literature[1,6]. We formed thin TiO_2 layers by ambient pressure MOCVD of either $[Ti(acac)_2(i-C_3H_7O)_2]$ or titanium (IV) isopropanolate $[Ti(i-C_3H_7O)_4]$. The aim of this feasibility study was to show the applicability of MOCVD techniques to passivate SnO_2 electrodes with a thin TiO_2 film.

Thin TiO_2 films made via MOCVD of [Ti(i-C_3H_7O)$_4$]
Highly rectifying TiO_2 films could be formed on SnO_2 substrates via MOCVD of $Ti(i-C_3H_7O)_4$ vapors in presence of oxygen. For security reasons argon was used as carrier gas, saturated with the precursor. The oxygen and argon flows were unified just before they entered the reaction chamber. The exact experimental set-up is described in detail in the experimental chapter.

Table 5.1 shows the resulting diode parameters of 4 different sets of $SnO_2/TiO_2(MOCVD)/$*spiro*-OMeTAD $/Au$ diodes which were derived from

experimental curves according to the Schockley equation. With increasing deposition time a gradual improvement of the junction performance can be observed. The shunt resistance, most likely due to bare SnO_2 surfaces exposed to the hole conductor, increases by two orders of magnitude when the reaction time is increased from 10 minutes to 40 minutes. At the same time the diode saturation current I_0 decreases by more than two orders of magnitude, while the ideality factor of the junction improves from 2.5 to 1.3. The series resistances show no clear trend. However the increase in layer thickness seems not to be accompanied by a significant increase in series resistance. Further more the junction properties become much more reproducible with increasing layer thickness.

Reaction time	10 min	20 min	30 min	40 min
R_{shunt} $[k\Omega/cm^2]$	34	67	145	3100
R_{series} $[\Omega/cm^2]$	594	592	541	616
I_0 $[\mu A/cm^2]$	0.47	0.13	0.050	0.0012
Ideality factor	2.5	1.8	1.6	1.3
Variance [%]	20	18	3	6

Table 5.1 The current-voltage characteristics of 4x4 SnO_2/TiO_2(MOCVD)/*spiro*-OMeTAD/Au diodes were analyzed accoding to the Schockley equation. The values shown are averages of 4 individual contacts. Four different deposition times were used to form the TiO_2 layers. The carrier gas flows were 15 ml/sec for argon/Ti(i-C_3H_7O)$_4$ and 15 ml/sec for oxygen. Argon was saturated with Ti(i-C_3H_7O)$_4$ by bubbling the carrier gas through a stirred solution of Ti(i-C_3H_7O)$_4$ at 85 °C. The hotplate on which the substrates were placed was at 450 °C. (general set-up see experimental).The value given as variance is the standard deviation of the current density at a forward bias of 500 mV), weighted with the median of the current density. It is given as an estimate for the reproducibility of the device characteristics.

Figure 5.6 shows the current-voltage characteristic of a diode made with 40 min deposition time, exhibiting comparable junction properties to devices made via spray pyrolysis (manual set-up). When the deposition time is further increased a detrimental effect is observed. Important shunt currents can be observed for samples based on TiO_2 layers with more than 40 minutes deposition time. Furthermore the series resistance of the device increases and the current-voltage characteristics show a s-shaped curve.
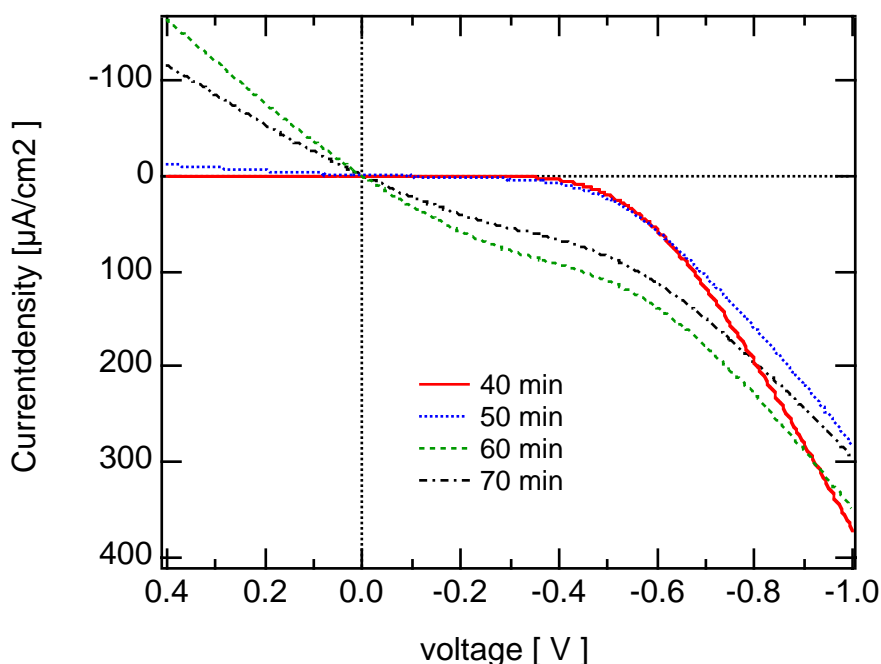
Figure 5.6 The current-voltage characteristics of four SnO_2/TiO_2(MOCVD)/*spiro*-OMeTAD/Au diodes assembled with TiO_2 layers produced with different deposition times. The MOCVD conditions were equivalent to those of 10/20/30/40 min deposition times series described above (see table legend 5.1).

The S-shaped curve might be explained by the presence of thin pinholes in the TiO_2 film. In reverse bias mode the SnO_2 electrode is biased positively. Hole conductor molecules in the pinhole, close to the SnO_2 surface get oxidized and diffuse through the pinhole to the bulk of *spiro*-OMeTAD. The stronger the positive bias, the more radical cations of *spiro*-OMeTAD will be formed, and the steeper the *spiro*-OMeTAD$^+$ gradient in the pinhole will be. A linear (ohmic) dependence of pinhole current and bias voltage is expected. In the forward bias

mode *spiro*-OMeTAD$^+$ will be reduced at the bottom of the pinholes. As the forward bias is increased a radical cation gradient is formed, with the *spiro*-OMeTAD concentration decreasing towards the bottom of the pinhole. Above a certain bias, the rate constant, with which *spiro*-OMeTAD$^+$ is reduced at the bottom of the pores, will be diffusion limited and therefore independent of the bias voltage. The current passing through the pinhole will thereby saturate. The superposition of such a 'pinhole-characteristic' and the original diode characteristic will give rise to the observed S-shape of the current-voltage characteristics[7].

In films with more than 40 min deposition time thin cracks were observed by STM imaging techniques. This confirms the interpretation made above.

It could be shown that MOCVD of $Ti(i\text{-}C_3H_7O)_4$ vapors is a convenient method to coat SnO_2 glass with TiO_2, thereby forming a pinhole free, highly rectifying junction with *spiro*-OMeTAD. The deposition time and thereby the layer thickness proved to be a critical parameter. Pinholes effects occurred at low TiO_2 coverage due to incomplete surface coverage as well as at high TiO_2 layer thickness due to the appearance of cracks. This high sensitivity towards the layer thickness was not observed for TiO_2 films made via spray pyrolysis (manual set-up). Analysis of the temperature dependence revealed that substrate temperatures of at least 300 °C are necessary to form rectifying junctions.

Thin TiO_2 films made via MOCVD of $Ti(acac)_2(i\text{-}C_3H_7O)_2$

Thin layers of TiO_2 were deposited onto SnO_2 substrates by MOCVD of $Ti(acac)_2(i\text{-}C_3H_7O)_2$ under various conditions. The experimental setup was identical to the one used for the MOCVD of $Ti(i\text{-}C_3H_7O)_4$ (see experimental). $Ti(acac)_2(i\text{-}C_3H_7O)_2$ saturated argon was produced by bubbling the carrier gas through a heated and stirred solution of the precursor. Parameters varied were the precursor and substrate temperatures, the precursor flow rate, the deposition time and the presence or absence of oxygen or water vapors.

TiO_2 films prepared in presence of oxygen *and* water vapors showed rectifying junction behavior towards *spiro*-OMeTAD. In absence of one of the two no blocking characteristics could be observed. The argon flux was saturated with water and $Ti(acac)_2(i-C_3H_7O)_2$ vapors by bubbling them first through water and then through heated TAA . Oxygen and the precursor flux were mixed just before the injection into the deposition chamber. Blocking diodes with shunt resistances of 100 kΩ/cm^2 and higher were obtained with a substrate temperature of 450 °C, a TAA temperature of 80 °C, carrier gas fluxes of 15 ml/sec for argon/$Ti(acac)_2(i-C_3H_7O)_2$ and 3 ml/sec for oxygen and deposition times of 15 to 25 minutes. However reproducibility of these results was problematic, as shunt resistances of 10 kΩ/cm^2 and less were obtained when attempting to reproduce the experiment under identical conditions.

All in all 60 individual diode contacts were analyzed. Due to the poor performance and reproducibility observed for this deposition methods it was abandoned in favor of other techniques. Additional experiments including detailed surface analytical methods like elipsometry, AFM and SEM would be necessary to analyze the encountered problems in more detail.

5.3. Titanium/*spiro*-OMeTAD Schottky diodes

Thin sputtered films of titanium, which were heated under oxygen formed rectifying Schottky contacts with *spiro*-OMeTAD. The heat treatment was crucial for this contact behavior, thereby suggesting that the presence of a thin oxide layer on top of the titanium surface is responsible for the observed contact behavior (metal-insulator-semiconductor junction).

Transmission electron microscopy and x-ray defraction analysis, conducted on sintered titanium films showed that the TiO_2 layer formed on top of the metal surface was of nanocrystalline nature, consisting of rutile particles of 10 – 50 nm.
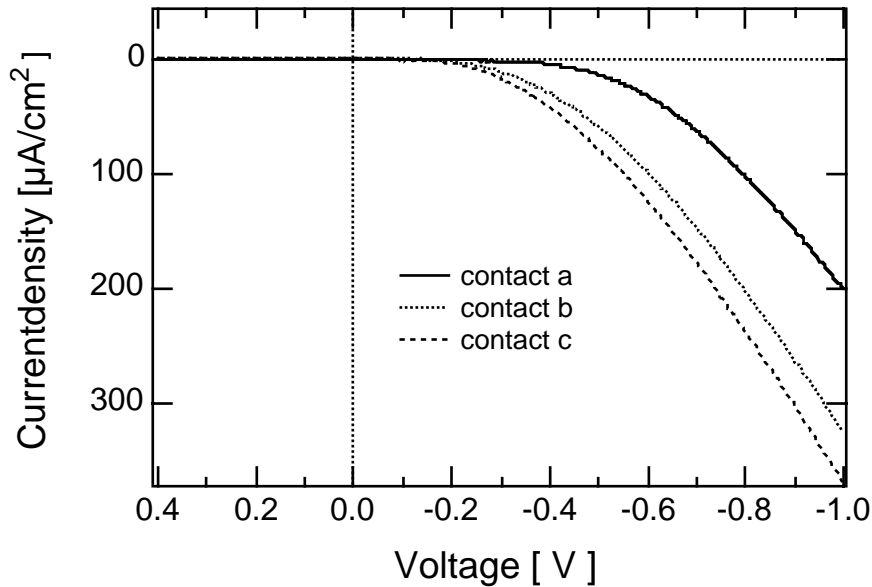
Figure 5.7 Current-voltage characteristics of three diodes: Ti/*spiro*-OMeTAD/Au. The 300 nm thick titanium layer, sputtered on a glass substrate, was heated in oxygen at 500 °C for 30 minutes prior to the diode fabrication.

Figure 5.7 shows the current-voltage characteristics of 3 individual diodes Ti/*spiro*-OMeTAD/gold. Compared to diodes made on spray pyrolized TiO_2 substrates the charateristics show a much stronger dispersion and a higher series resistance (about 1500 Ω/cm^2 compared to 830 Ω/cm^2). The stronger dispersion indicates increased inhomogenity of the oxidized metal surface, while the increase in series resistance could be due to a significant series resistance of the oxide layer itself. It was also observed that it was difficult to establish a good contact to the oxidized titanium with contact pins (gold). This might be an additional source for the observed increase in series resistance.

5.4. Time evolution of the *spiro*-OMeTAD/gold contact

The contact established between *spiro*-OMeTAD and gold upon evaporation of gold on top of $[N(p-C_6H_4Br)_3][SbCl_6]$ doped *spiro*-OMeTAD layers evolved from blocking to ohmic with time[8]. The rectification behavior was inverse to that observed for TiO_2/spiro-OMeTAD-junctions, suggesting that the *spiro*-

OMeTAD/gold contact rather than the SnO_2/*spiro*-OMeTAD was responsible for the observed rectification. This was supported by the observation that the time dependence was clearly triggered by the moment of the gold evaporation, while 'aging' of the SnO_2/*spiro*-OMeTAD junction after spin-coating had no effect. We further observed that the time evolution could be drastically slowed down by storing the devices in an argon atmosphere, suggesting that the presence of either oxygen or moisture was essential for the observed effect. In parallel to our observations Ionnidis and co-workers[9] reported on the time evolution of evaporated gold contacts on TPD/polycarbonate matrixes, evolving from blocking to ohmic over time. They explained their results in terms of damage to the TPD surface induced by the harsh conditions of the evaporation process, followed by a 'surface repair process'. Interdiffusion of gold and TPD as mechanism, leading to an ohmic contact was ruled out on the basis of TEM studies.

To further elucidate the underlying mechanisms a series of SnO_2/*spiro*-OMeTAD/Au devices were made and stored under different conditions. Further more the influence of the dopant was studied, comparing *spiro*-OMeTAD^{++}(PF$_6^-$)$_2$ with [N(*p*-C$_6$H$_4$Br)$_3$][SbCl$_6$] (see Figure 5.8).

Immediately after the gold evaporation all samples showed a rectifying behavior the current was blocked upon negative polarization of the SnO_2 electrode. The rectifying character showed a wide variance for both dopants. Current densities at –1.0 V ranged from several hundred $\mu A/cm^2$ to a few $\mu A/cm^2$. The time development of the devices stored under argon was drastically different, depending on which dopant was used. In case of [N(*p*-C$_6$H$_4$Br)$_3$][SbCl$_6$] doped samples the contact very slowly evolved to ohmic, more than one week being necessary to accomplish this change. Furthermore it is interesting to note that the conductivity of the device decreased over the observed time period (compare the slopes of the characteristic after *5 days* and *40 days* in Figure 5.8.a). When *spiro*-OMeTAD^{++}(PF$_6^-$)$_2$ was used as dopant the rectifying character of the devices slightly *improved* over the observed time period, while the conductivity (as

analyzed from the slope of the current-voltage characteristics upon positive polarization of the SnO_2 electrode) did not show any remarkable change.

When stored in dry oxygen the devices modified with either dopant evolved from rectifying to ohmic. The $[N(p\text{-}C_6H_4Br)_3][SbCl_6]$ doped samples evolved faster than those using $spiro\text{-}OMeTAD^{++}(PF_6^-)_2$. The latter increased their conductivity slightly over 40 days, while the former suffered some losses in conductivity. In presence of water vapors the samples of both dopants evolved from blocking to ohmic. The kinetics is however slower than in presence of oxygen. Another stunning feature, which can be read out of Figure 5.8.e) and f), is the severe loss in conductivity for all samples. This effect is most striking for the $[N(p\text{-}C_6H_4Br)_3][SbCl_6]$ doped sample, which lost about two thirds of its conductivity after 40 days, compared to the sample stored under argon. Along with the degradation of the conductivity we observed that the devices were mechanically unstable when stored over water, with parts of the organic film peeling away from the SnO_2 surface. The strong affinity of water to the SnO_2 surface could explain this observation. To distinguish between the effects of *condensed water* on the sample surface (induced by daily fluctuations in temperature) and *water vapor* the experiment should be repeated, storing the samples over an aqueous salt solution at constant temperature.

Summarizing the observed effects it should be concluded that

-   Devices, containing a doped *spiro*-OMeTAD layer as electrically active component should be sealed off or stored away from ambient moisture.
-   Samples using $spiro\text{-}OMeTAD^{++}(PF_6^-)_2$ as dopant exhibit a much better longterm stability than their $[N(p\text{-}C_6H_4Br)_3][SbCl_6]$ doped analogues. While exhibiting similar conductivities just after the evaporation the conductivity after 40 days (stored in oxygen) is about twice as high for the $spiro\text{-}OMeTAD^{++}(PF_6)_2$ doped sample.
-   Interdiffusion of gold and *spiro*-OMeTAD as underlying mechanism for the development of an ohmic contact is unlikely, as this process should be independent of the presence or absence of oxygen or moisture.

- The repair mechanism postulated by Ionnidis also stands in contrast to the observed influence of oxygen. A possible explanation which takes the effect of oxygen into account might be that only *doped* films exhibit ohmic contact to gold. The evaporation conditions might lead to a depletion of molecularly dissolved oxygen inside the organic layer and to undoping of a thin film of *spiro*-OMeTAD under the influence of the high thermal energy of the arriving gold atoms. A thin, fully undoped film of *spiro*-OMeTAD might be formed hereby, which shows a blocking behavior towards gold. In case of the $[N(p\text{-}C_6H_4Br)_3][SbCl_6]$ doped films stored under argon the potential oxidation power of the $SbCl_6^-$ ions might be the reason why these samples recover even in absence of oxygen, while *spiro*-OMeTAD$^{++}(PF_6^-)_2$ doped samples show no such tendency.
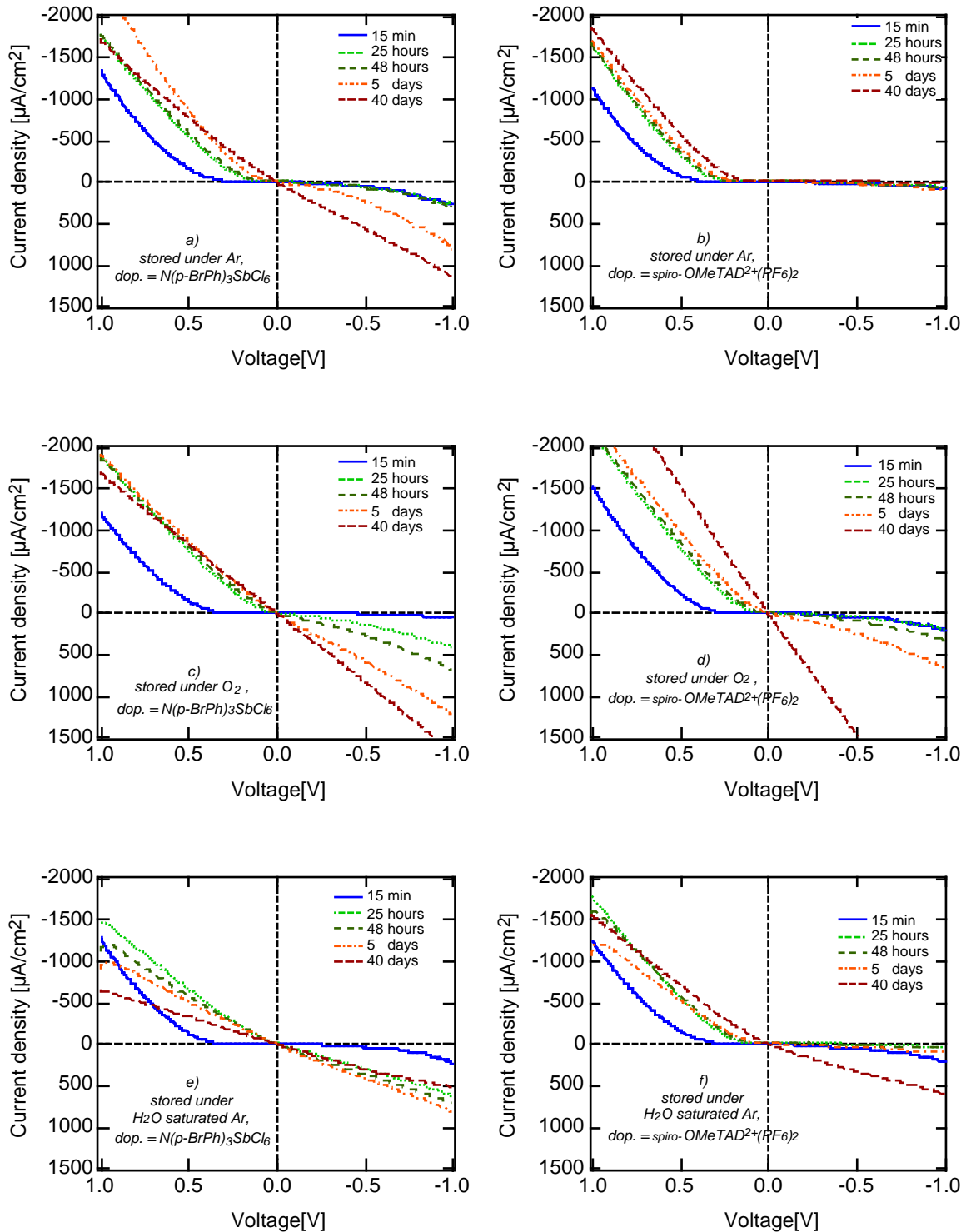
Figure 5.8 Time evolution of the current-voltage characteristics for SnO_2/*spiro*-OMeTAD/Au devices. Samples a), c) and e) were doped with 0.088 mol% [N(p-C_6H_4Br)$_3$][SbCl$_6$]; samples b), d) and f) with 0.044 mol% *spiro*-OMeTAD^{++}(PF$_6$)$_2$. Samples a) and b) were stored in the glove-box under argon atmosphere, sample c) and d) under pure oxygen and sample e) and f) under water-saturated argon. The samples were measured immediately after the gold evaporation, 24h, 48 hours, 5days and 40 days after the gold evaporation. For each measurement a representative characteristic out of four characterized samples is shown.

References

1) Boschloo, G. K.; Gosssens, A.; Schoonman, J. *J. Electrochem. Soc.* **1997**, *144*, 1311-1317.

2) Kavan, L.; O'Regan, B.; kay, A.; Grätzel, M. *J. Electroanal. Chem.* **1993**, *346*, 291-307.

3) Okuya, M.; Prokudina, N. A.; Mushika, K.; Kaneko, S. *J. Euro. Cer. Soc.* **1999**, *19*, 903-906.

4) Yanagi, H.; Ohoka, Y.; Hishiki, T.; Ajito, K.; Fujishima, A. *Appl. Surf. Sci.* **1997**, *113/114*, 426-431.

5) Kavan, L.; Grätzel, M.; *Electrochimica Acta* **1995**, *40*, 643.

6) Tilcom Chemicals, *Technical Bulletin TIL IIC; Organic titanates, their chemistry and industrial application* London.

7) *Brian O'Regan is gratefully acknowledged for helpful discussions concerning the s-like shape of these curves.* .

8) Krüger, J. *Modification von Titandioxid-Halbleiterschichten für die Anwendung in der hybriden Solarzelle*; master thesis; University of Heidelberg: Heidelberg, 1998.

9) Ioannidis, A.; Facci, J. S.; Abkowitz, M. A. *J. Appl. Phys.* **1998**, *84*, 1439-1444.

Chapter 6

Photovoltaics

6.1 Analysis of photoresponse spectra

6.1.1 External charge carrier collection efficiencies

A cascade of multiple electron transfer steps has to proceed to convert a photon incident on a dye-sensitized solar cell into an electron in the external circuit. If only one of these steps is inefficient the whole cascade is interrupted, resulting in low external quantum efficiencies (IPCEs). Equation 6.1 shows, how the IPCE can be split up into the product of a series of individual probabilities and quantum efficiencies[3].

$$IPCE = \prod_i \Phi_i = \Phi_{trans} \cdot \Phi_{lh} \cdot \Phi_{inj} \cdot \Phi_{reg} \cdot \Phi_{cc} \tag{6.1}$$

ϕ_{trans}	=	probability for the photon to reach the photovoltaic junction
ϕ_{lh}	=	probability for the photon to be absorbed by the sensitizer[1]

---

[3] It should be noted that equation 6.1 implies the simplification that the individual probabilities are independent of each other; an assumption which does not necessarily hold.

[1] the n-type and p-type semiconductors forming the heterojunction also may adsorb light and also may thereby contribute to the photocurrent. To simplify matters we shall only consider photons

ϕ_{inj} = quantum efficiency for photoelectron injection from the excited sensitizer

ϕ_{reg} = quantum efficiency for the hole transfer from the sensitizer to the hole conductor

ϕ_{cc} = quantum efficiency for collecting an initially formed electron hole pair $[e^-_{TiO2} \cdot h^+_{holeconcuctor}]$ in the external circuit

The probability of light harvesting ($\phi_{trans} * \phi_{lh}$) can be determined from the optical characteristics of the different cell components. Optical losses occur already before the light reaches the photovoltaically active layer (ϕ_{trans}). They are due to adsorption and back reflection of the cell's window materials. Reflection losses can be controlled by a refractive index matching of the different optical layers ("antireflection coating") or by reducing the haze of the conducting metal oxide layer. Absorption losses can be limited by tuning the thickness of the conducting layer d. This usually means a trade off between its conductivity (proportional to d) and its transparency (proportional to e^{-d}). As these optical losses are relatively easy to quantify one can already consider them by defining a so-called *transmission corrected photoresponse* (IPCE^{corr}):

$$IPCE^{corr} = \frac{IPCE}{\Phi_{trans}} \qquad (6.2)$$

A further correction step is to define a quantum efficiency, which only considers the conversion of photons absorbed inside the photovoltaically active layer. This so-called adsorbed photon-to-electron quantum efficiency (APCE) can be defined as:

$$APCE = \frac{IPCE}{\Phi_{trans} \cdot \Phi_{lh}} \qquad (6.3)$$

Considering an ideal solar cell, showing unity quantum efficiency for the initial formation of the charge separated state ($\phi_{inj} * \phi_{reg}$) and unity charge carrier

---

with an energy smaller than the smallest bandgap of the two semiconductors. Furthermore the optical absorption of dopants shall not be considered.

collection efficiency (ϕ_{cc}) we would expect the APCE to be 100% throughout the total spectral absorption range of the absorber. As losses, due to bad transmission of the window materials and low light harvesting can be quite substantial, APCEs can reach 100 %, even though the measured IPCE is much lower. Calculation of the APCE or further analysis of the spectral photoresponse is therefore a prerequisite in order to determine the predominant loss mechanism in a photovoltaic device. In the following a simple method shall be presented, which allows the retrieval of information on the quantum efficiency of the individual electron transfer steps. It therefore represents an independent method to the direct measurement of the electron transfer rate constants via transient laser spectroscopy.

6.1.2 A simple model approach to probe and quantify charge recombination from IPCE spectra

As discussed in the previous section, an APCE value smaller than unity can either be due to an incomplete formation of the initial charge separated state [e^- $_{TiO_2}$: h^+ $_{spiro\text{-}OMeTAD}$] (*injection limited*) or to the recombination of the initially formed charge carriers during the collection process (*collection limited*). In the following we shall see that from the shape of frontside and backside illumination action spectra we can conclude, whether the photocurrent of a given solar cell is *injection* or *collection* limited. In chapter 5 we learned that the dense TiO_2 layer efficiently blocks direct contact of *spiro*-OMeTAD and SnO_2. Furthermore we derived from SEM pictures at device cross-sections that a bulk *spiro*-OMeTAD layer located between the heterojunction and the gold electrode impedes direct contact of gold and TiO_2, thereby restricting charge recombination to the TiO_2/*spiro*-OMeTAD interface (see Figure 6.1).
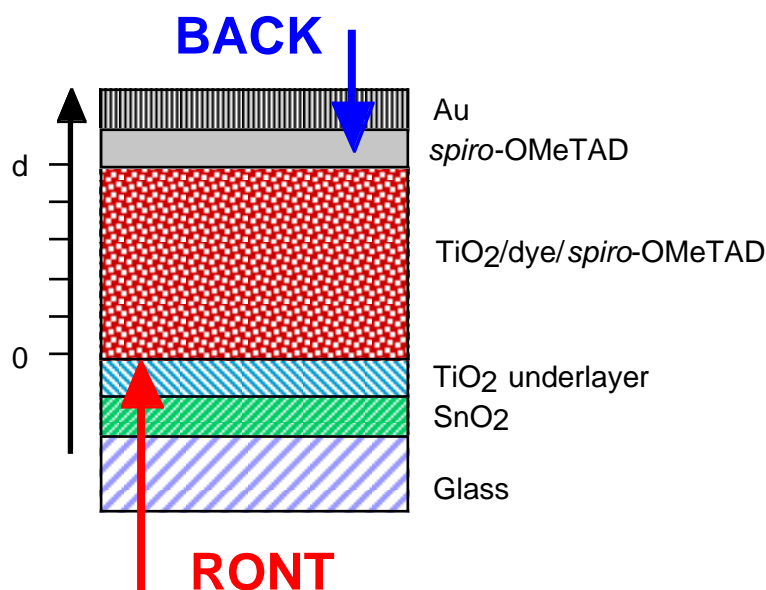
Figure 6.1 Definition of front- and backside illumination and the coordinate x, describing the location inside the film.

Figure 6.2 shows a typical example for a set of IPCE spectra obtained upon frontside and backside illumination, compared to the absorptivity of the sensitized TiO_2 layer. At the point of maximum absorptivity of the dye layer (560 nm; A $\approx$ 3.0) the IPCE^{front} spectrum exhibits a *maximum*, while the IPCE^{back} spectrum exhibits a *minimum*. Even when corrected for the transmission losses of the SnO_2 and gold electrode respectively the IPCE values under backside illumination mode is up to more than one order of magnitude smaller, than the corresponding value for IPCE^{front}. Thus electrons generated close to the gold electrode have a much smaller probability of reaching the SnO_2 electrode than those, which are generated in its close vicinity. This finding clearly indicates that recombination of photo-generated electrons while migrating towards the collecting electrode is a major loss mechanism. In the following a model shall be discussed, which allows to quantify the recombination process by analysis of the spectral shape of IPCE^{front} and IPCE^{back}.
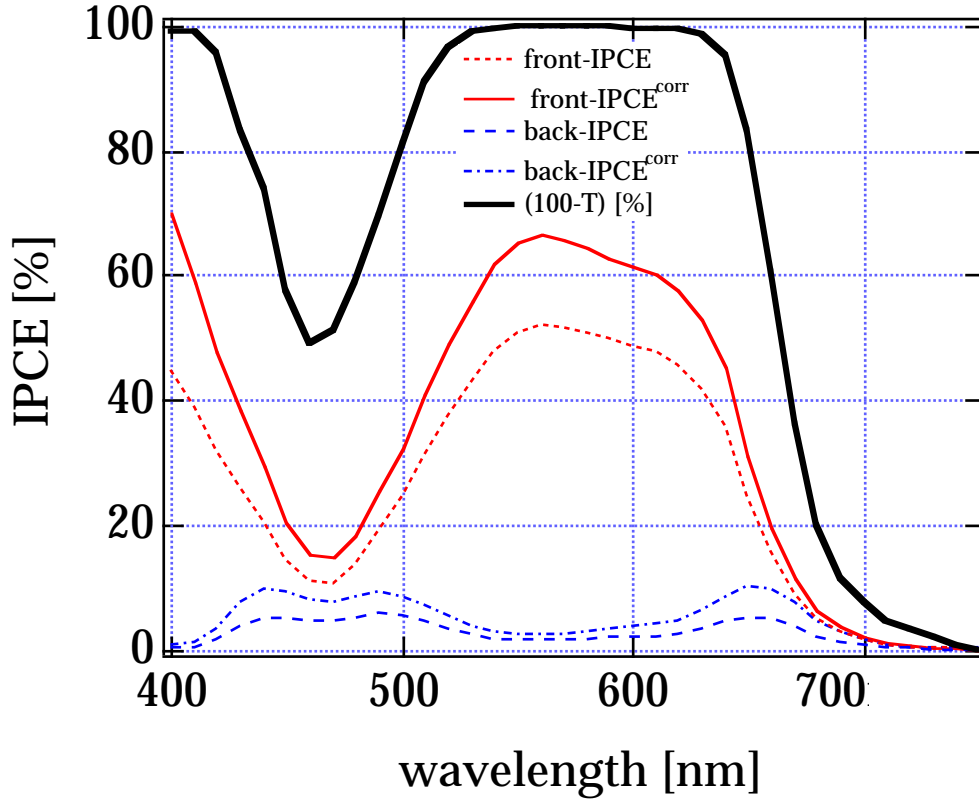
Figure 6.2 Frontside/backside illumination photoresponse spectra for a 4 µm thick solid-state solar cell, sensitized with a merocyanine dye (Mc3). The IPCE spectra are shown as measured (front-IPCE, back-IPCE) and corrected for the transmission of the SnO_2-substrate (front-IPCE^{corr}) and the 10 nm thick gold electrode (back-IPCE^{corr}) respectively (details see below). For comparison the absorptivity spectrum of the dye-sensitized layer is shown. It corresponds to the IPCE spectra expected for $(\phi_{trans}*\phi_{inj}*\phi_{reg}*\phi_{cc}) = 100\,\%$.

In a solid-state dye-sensitized solar cell with a moderately doped hole conducting layer (>0.01 mol%) the concentration of holes will not significantly change at illumination intensities typical for action spectra measurements (the conductivity of the film is much higher than its photoconductivity). In a first approximation the concentration of holes in the hole conductor can therefore be considered as constant over the total width of the film. The TiO_2 is assumed to be an intrinsic semiconductor, with the concentration of the photo-injected electrons being much higher than the equilibrium concentration of electrons in the conduction band in the dark. This also implies that the concentration of the photogenerated electrons inside the TiO_2 is much smaller than the concentration of holes in the hole conductor. In a second approximation, the presence of electric fields inside the nanoporous TiO_2 network shall be neglected.

To quantify the recombination we assume that each electron is subject to the same probability of charge recombination, when traveling the distance *dx* towards the collecting electrode, so that recombination is proportional to *dx* and constant throughout the total film thickness. The probability of charge collection for an electron generated at distance x from the collecting electrode is therefore given as:

$$\phi_{cc}(x) = e^{-\beta x} \tag{6.4}$$

Where β is a constant describing the recombination probability with β^{-1} being equivalent to the mean free path length of the electron.

The quantum efficiency of light harvesting neglecting any sort of reflection phenomena (for a film of thickness *d* at a given wavelength λ) can be expressed as the integral of the *differential quantum efficiency of light harvesting* from zero to d:

$$\Phi_{lh}(d) = \int_0^d \phi_{lh}(x)dx = 1 - e^{-\alpha d} \tag{6.5}$$

According to Lambert-Beer ϕ_{LH} for front- and backside illumination are defined as:

$$\phi_{lh}^{front}(x) = \alpha \cdot e^{-\alpha x} \tag{6.6}$$

$$\phi_{lh}^{back}(x) = \alpha \cdot e^{-\alpha(d-x)} \tag{6.7}$$

With α corresponding to the absorption coefficient[4].

IPCE^{corr} can then be expressed as:

---

[4] Extinction coefficients and absorbance generally refer to the *decadic* values, according to the definition introduced by Lambert-Beer. In this section however the *natural logarithm* shall be used.

$$IPCE^{corr} = \Phi_{inj} \cdot \Phi_{lh} \cdot \Phi_{cc} = \Phi_{inj} \cdot \int_0^d \phi_{lh}(x) \cdot \phi_{cc}(x) dx \qquad (6.8)$$

respectively for front- and backside illumination:

$$IPCE_{corr}^F = \Phi_{inj} \cdot \int_0^d \alpha \cdot e^{-\alpha x} \cdot e^{-\beta x} dx \qquad IPCE_{corr}^B = \Phi_{inj} \cdot \int_0^d \alpha \cdot e^{-\alpha(d-x)} \cdot e^{-\beta x} dx \qquad (6.9)$$

$$IPCE_{corr}^F = \Phi_{inj} \cdot \frac{\alpha}{\alpha+\beta} \cdot \left(1 - e^{-(\alpha+\beta)d}\right) \qquad IPCE_{corr}^B = \Phi_{inj} \cdot \frac{\alpha}{\alpha-\beta} \cdot \left(e^{(\alpha-\beta)d} - 1\right) \cdot e^{-\alpha d} \qquad (6.10)$$

For the ratio of IPCE front to back we therefore obtain:

$$ratio^{IPCE} = \frac{IPCE_{corr}^F}{IPCE_{corr}^B} = \frac{\alpha-\beta}{\alpha+\beta} \cdot \frac{\left(1 - e^{-(\alpha+\beta)d}\right)}{\left(e^{(\alpha-\beta)d} - 1\right) \cdot e^{-\alpha d}} \qquad (6.11)$$

It is very important to note that the $ratio^{IPCE}$ is independent of the injection quantum efficiency and simply a function of alpha and beta. Therefore, at each wavelength a beta value can be obtained, when the IPCE ratio and the absorption of the sample are known.

Corrections for transmission and reflection

In order to consider the more complex optical structure of our solar cell devices further corrections have to be introduced. Therefore the solid-state solar cell and its components were thoroughly characterized, using a UV/VIS spectrometer, equipped with an integrating sphere. The aim was to determine (1) the absorptivity of the sensitized layer and (2) the transmission and reflection losses brought about by the window materials, in order to calculate IPCE[corr] and (3) the fraction of light, which is backreflected into the dye-sensitized junction (e.g. from the gold electrode in the frontside illumination mode). The latter will give rise to an additional photocurrent contribution to the term derived for the front and backside illumination IPCE according to

$$IPCE_{corr}^{F} = \Phi_{inj} \cdot \left[\frac{\alpha}{\alpha+\beta} \cdot \left(1 - e^{-(\alpha+\beta)d}\right) + R_{Au} \cdot \frac{\alpha \cdot e^{-2\alpha d}}{\alpha-\beta} \left[e^{(\alpha-\beta)d} - 1\right] \right] \qquad (6.12)$$

$$IPCE_{corr}^{B} = \Phi_{inj} \cdot \left[\frac{\alpha}{\alpha-\beta} \cdot \left(e^{(\alpha-\beta)d} - 1\right) \cdot e^{-\alpha d} + R_{SnO_2} \cdot \frac{\alpha \cdot e^{-\alpha d}}{\alpha+\beta} \cdot \left(1 - e^{-(\alpha+\beta)d}\right) \right] \qquad (6.13)$$

With R_{Au} and R_{SnO2} standing for the reflections of the gold and SnO$_2$ electrode respectively. The expression for ratio^{IPCE} changes accordingly.

$$ratio^{IPCE} = \frac{\dfrac{\alpha}{\alpha+\beta} \cdot \left(1 - e^{-(\alpha+\beta)d}\right) + R_{Au} \cdot \dfrac{\alpha \cdot e^{-2\alpha d}}{\alpha-\beta} \left[e^{(\alpha-\beta)d} - 1\right]}{\dfrac{\alpha}{\alpha-\beta} \cdot \left(e^{(\alpha-\beta)d} - 1\right) \cdot e^{-\alpha d} + R_{SnO_2} \cdot \dfrac{\alpha \cdot e^{-\alpha d}}{\alpha+\beta} \cdot \left(1 - e^{-(\alpha+\beta)d}\right)} \qquad (6.14)$$

Reflection losses occurring in a layered structure will depend on the matching of the spectral indexes of the successive layers. This has to be taken into consideration, when characterizing the optical properties of single components of the cell. When determining the transmission of the SnO$_2$ glass and the dense TiO$_2$ layer we therefore accounted for the influence of the contacting nanocrystalline TiO$_2$ layer by characterizing a series of devices [glass/SnO$_2$/TiO$_2$(dense)/TiO$_2$(nanocrystalline)] exhibiting different thickness of the nanocrystalline layer (1.4; 2.3 and 3.9 µm), with regards to their total/diffuse/direct reflection and transmission. The effective total transmission in a wavelength domain of 400 to 900 nm in the *absence* of the TiO$_2$ layer was then determined via linear extrapolation of the values received for the three nanocrystalline samples to a thickness of zero.

No corrections were made to consider the presence of the hole conductor and the dye at the interface. Filling of the nanoporous TiO$_2$ structure with *spiro*-OMeTAD might significantly reduce light scattering due to the resulting refraction index matching. Neglect of this effect might lead to a small overestimation of the corrected front-IPCE and of β. A more exact optical characterization of the SnO$_2$/TiO$_2$/dye/*spiro*-OMeTAD interface should be the main objective for future improvements of this data analysis.

During each gold evaporation procedure a blank gold film was evaporated on plain glass. In prior experiments it was found that the transmission and reflection of glass/gold samples are very similar to those of glass/*spiro*-OMeTAD/gold exhibiting an identical gold layer thickness. As the presence of the thin *spiro*-OMeTAD layer (applied via spin coating prior to the evaporation) induced strong interferences the gold layer was characterized preferably on glass. The absorptivity of the dye-sensitized layer was characterized *after* the spin-coating procedure. Small errors are introduced hereby, as the absorption of the dopant, present in the hole conductor will also slightly contribute to the overall absorption. Therefore IPCE values should, if possible, be analyzed at wavelengths above 540 nm, beyond the *spiro*-OMeTAD$^+$ absorption. The UV/VIS characterization was nevertheless performed *after* the spin coating, as the latter was often accompanied with large spectral shifts of the dye absorption (20 nm for Mc3) Figure 6.2 shows a typical example for the transmission and reflection spectra obtained.
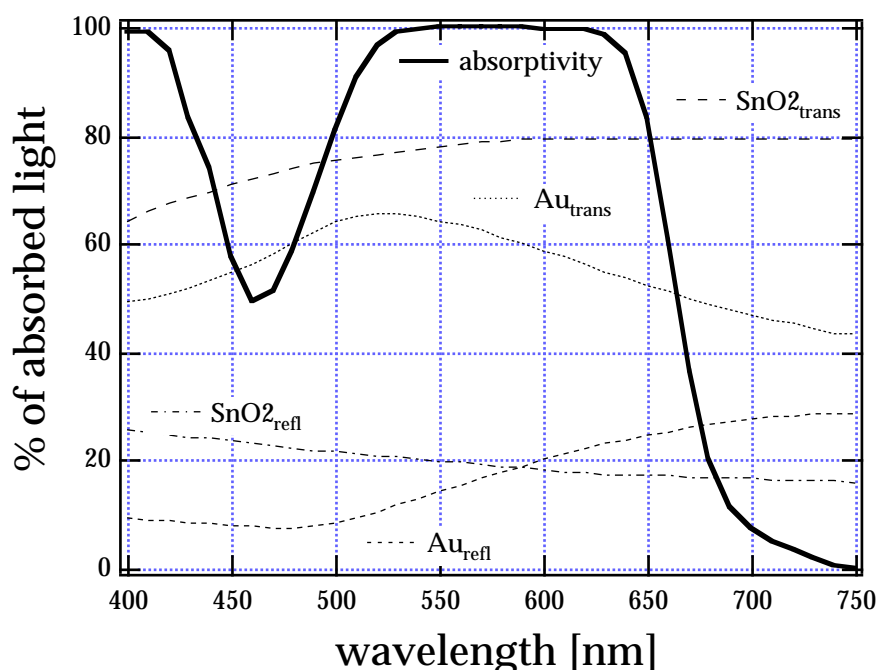
Figure 6.2 Transmission and reflection of the different optical components/interfaces of the solar cell for Asahi SnO_2 glass, covered with a 50 nm thick dense TiO_2 layer and a gold layer of 10 nm thickness. The optical absorption of a 4 μm thick nanocrystalline TiO_2 film, sensitized with the merocyanine dye Mc3 is also shown (absorptivity).

The data shown in Figure 6.2 was used to calculate IPCE^{corr} under front and backside illumination conditions. It can also be used to calculate the APCE values according to the equation given above. An example is given in Figure 6.3.
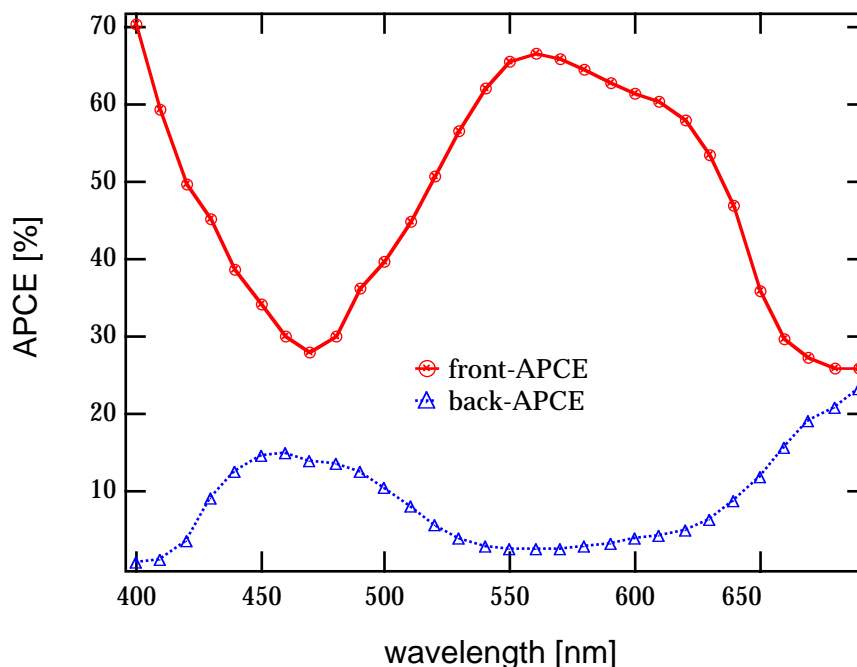
**Figure 6.3** APCE spectra for the same device as in Figure 6.2.

The APCE spectra show a strong resemblance to the IPCE spectra, giving further indication that the location of photon absorption inside the film is important for the yield of its conversion into an electron in the external circuit. If the photocurrent would be injection rather than collection limited, the APCE for frontside and backside illumination should be constant and wavelength independent over the observed spectral range. From 500 to 650 nm the frontside-APCE resembles strongly the absorption spectrum of the dye-sensitized layer, while it appears to reach a constant value of about 25 % at longer wavelengths. This constant value is also reached for the *backside*-APCE in this wavelength domain. This is plausible, as in weakly absorbing films the number of photons absorbed per film volume becomes independent of the position inside the film and on the illumination mode (front/back). The strong decrease of the backside-APCE below 450 nm is most likely due to the strong absorption of a thin *spiro*-

OMeTAD layer between the gold contact and the dye-sensitized heterojunction. At 400 nm it drops to 0 %, while the front APCE reaches 70 % at this wavelength. However, the optical density of the dye layer at 400 nm of about 0.7 (decadic) is much smaller than the peak absorption at 560 nm (A = 3.0; decadic). This is a very interesting observation, as it gives an indication that the hole conductor located inside the pores is photovoltaically active, otherwise it would exhibit an inner filter effect, decreasing the efficiency, instead of increasing it. The effect can be clearly assigned to *spiro*-OMeTAD, as the absorption of TiO_2 at 400 nm is still very weak. As a consequence one can conclude that doped organic films can exhibit high conductivities *and* exciton diffusion lengths comparable to the average pore size of the TiO_2 film. This is a prerequisite for future work, to realize solid-state solar cells in which the hole conductor takes over the function of the sensitizer.

Data analysis

Different approaches can be made to determine values for β and Φ_{inj}.

I)   From each set of IPCE^{corr} (front&back) and α at a given wavelength one can determine values for β and Φ_{inj} according to equation 6.14. Figure 6.4 shows an example for such an analysis, conducted by means of a computer program. In the wavelength range from 540 to 640 nm the analysis at each data point yields values of about 4 for β and slightly more than 1 for Φ_{inj}. Above 640 nm the fitting results deviate from this value, exhibiting a strong rise till 660 nm and falling down to zero for higher wavelengths. However, according to our model, β and Φ_{inj} should be independent of the wavelength. The deviations observed above 640 nm might be explained in terms of the sharp drop of the merocyanine's absorption around 660 nm (from 83% to 20 % absorptivity within 30 nm) effecting the data analysis in this region to be very sensitive to very small spectral shifts. Further explanations for the apparition of this artifact are discussed below.
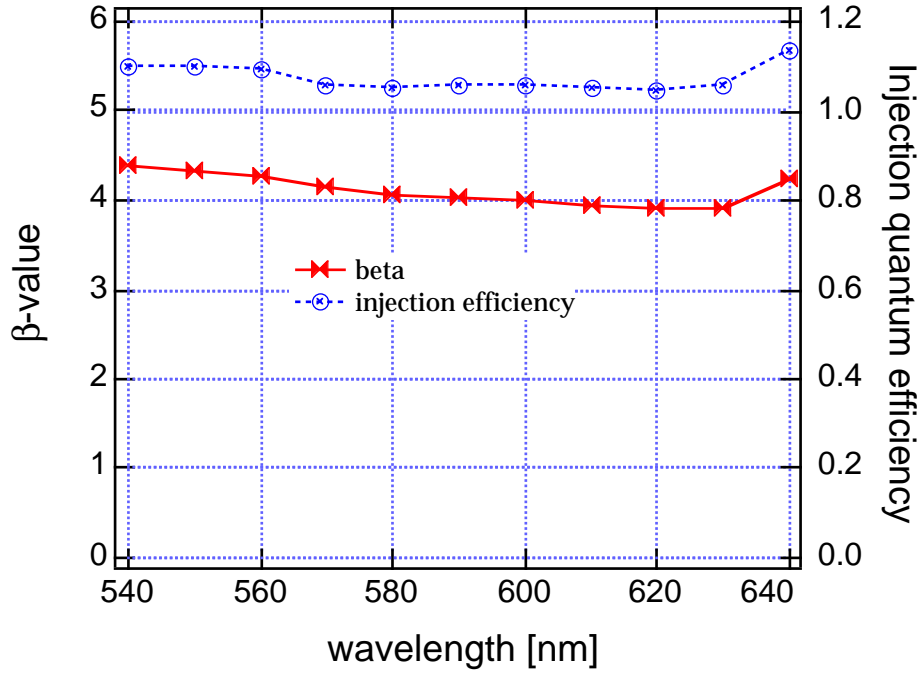
Figure 6.4 Values for β and Φ_{inj} derived via analysis of the frontside and backside IPCE, according to equations 6.14, based on the data shown in Figure 6.2. As the thickness of the film was set to one for simplicity reasons the diffusion length of the electron with β=4 and d= 4 μm will be 1 μm.

II)   To determine β it might also be convenient to calculate a set of ratio$^{IPCE}(\lambda)$ based on the known absorption of the dye-sensitized film α and a set of β values. The β value giving rise to the best fit of calculated and measured ratio^{IPCE} will then be chosen as output parameter for β. Φ_{inj} is then accessible as the proportionality factor converting the calculated front-IPCE$^{corr}(\lambda)$ into the measured IPCE$^{corr}(\lambda)$. Figure 6.5 shows a typical example. The shape of calculated and measured curves agree well, confirming the assumptions of the model . Again, comparison of the curves in the wavelength range of 540 – 640 nm suggests values of about 4 to 4.5 for β. Deviations occur at wavelengths shorter than 550 nm. This might be induced by to the absorption of *spiro*-OMeTAD$^+$. SEM pictures showed that solar cells to which the hole conductor is applied via a spin coating procedure exhibit a thin film (in the order of one micron) of doped hole conductor matrix on top of the nanocrystalline film. This layer acts as inner filter, further reducing the back-IPCE, thereby resulting in an increase in ratio^{IPCE} at wavelengths shorter than 540 nm. Above 650 nm a certain

mismatch of calculated and measured data points can be observed. According to equation 6.12 ratio^{IPCE} will converge to 1.0 for small values of α. As back reflection effects of the gold layer and the SnO_2 substrate are also taken into consideration this calculated boundary value is slightly larger than one (above 600 nm the gold layer is a better reflector than SnO_2). However the experimental value is still larger, suggesting that the optical characterization of the solar cell device still has to be refined. The derivation observed at about 650 nm might be either due to small spectral shifts of the absorption spectrum, between the moment, when the cells absorption was characterized and when its photoresponse was measured or to small errors concerning the wavelength calibration of the IPCE set-up. Indeed the monochromator employed in the IPCE setup was found to exhibit a wavelength dependent offset, leading to very small deviations around 470 nm (where it was frequently calibrated) and larger derivations in the bathochromic region, where the offset increased linearly. However the measured IPCE spectra are already corrected with regards to this. Another effect, which might explain the difference between calculated and measured spectra is the spectral bandwidth of the monochromatic measuring light. It was determined to exhibit a peak halfwidth of about 10 to 15 nm (by measuring the broadened photoresponse of a silicon cell, which was combined with small bandwidth interference filters of known transmission behavior). Convoluting the product of the calculated IPCE spectra with a gaussian distribution having this halfwidth accounted for some of the observed experimental features.

III)   Another way to analyze IPCE data is to display the IPCE ratio as a function of the optical absorption of the sensitized film at the observation wavelength, as shown in Figure 6.6. This is convenient to compare solar cell devices, which exhibit different spectral shapes.
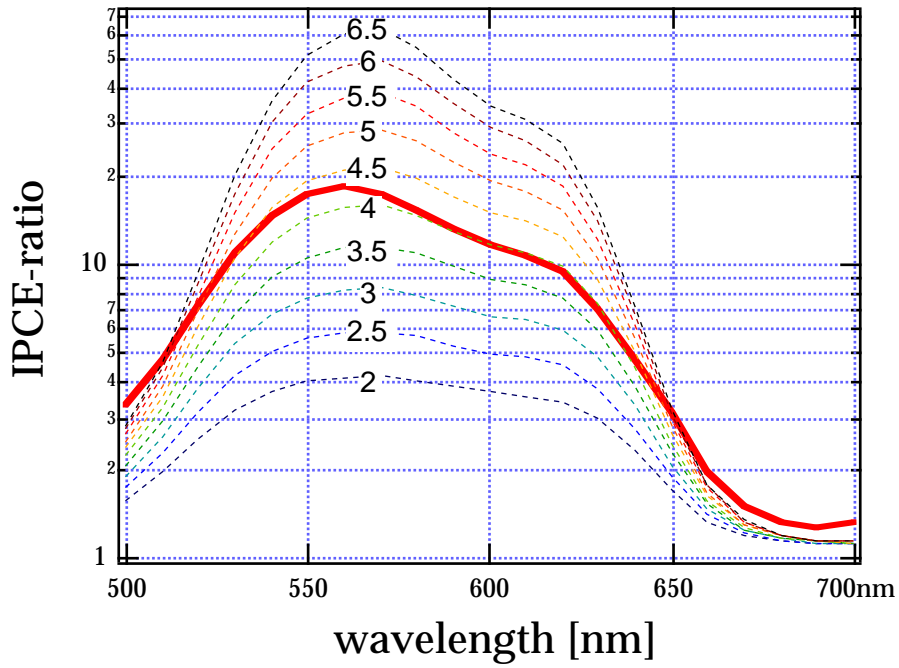
Figure 6.5 Measured (plain line) and calculated values (dotted line) for the ratio of front- to backside IPCE, based on the data shown in Figure 6.2. Different values for β were used to calculate ratio^{IPCE} (see numbers in Figure).
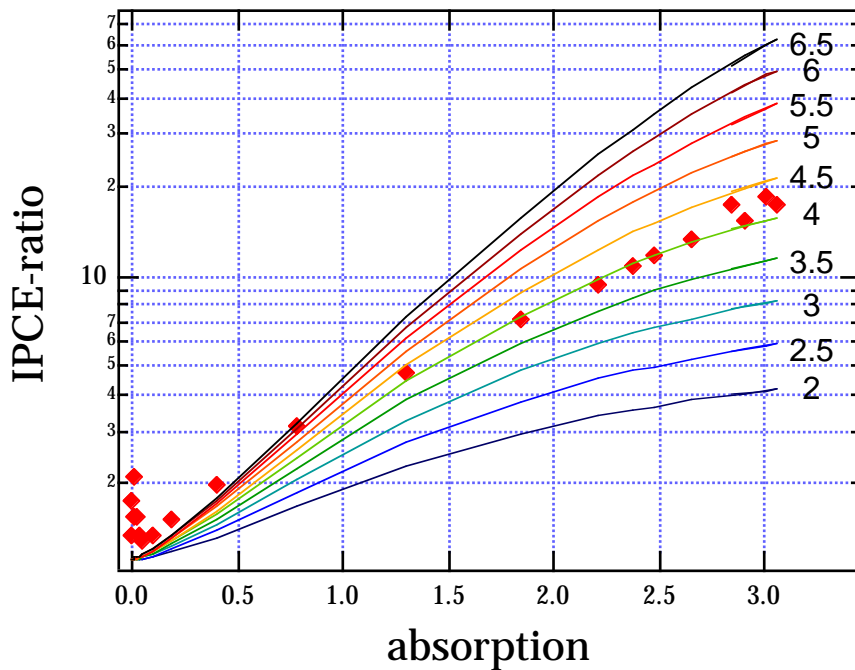

Figure 6.6 Measured (dots) and calculated (lines) IPCE ratio as a function of the optical absorbance (decadic, according to Lamber-Beer) of the sensitized film. Values for β between 2.0 and 6.5 were used to calculate ratio^{IPCE}.

The data analysis shown above yields a value for beta of about 4.0 ± 0.5. From Table 6.1 we can conclude that an injection efficiency of 106 % is needed, to superimpose the calculated and measured front-IPCE spectra. This is slightly above the theoretical limit of 100 % and might well be explained by minor experimental errors or limitations, due to the strong simplifications used in this model.

β	Φ_{inj} (calculated [%])	$Max(IPCE_{corr}^{F})$ for $\Phi_{inj} = 100\%$
2	87	77.8
2.5	91	73.8
3	96	70.1
3.5	101	66.8
4	106	63.7
4.5	111	61
5	115	58.4
5.5	120	56.1
6	125	54
6.5	130	52

Table 6.1 indicates for each of the chosen beta values the injection quantum efficiency, needed to mach the peak value of the *calculated* front-IPCE spectrum with the peak value of the *measured* front-IPCE spectrum. For comparison the maximum peak values for the calculated front-IPCE are given, assuming 100 % injection efficiency.

Figure 6.7 finally shows the calculated front- and backside IPCE, using the fit results of 4.0 for β and an injection efficiency of 100 %. Both, the calculated front- and back-IPCE are in very good agreement with the experimental data. This confirms the assumption that **charge recombination occurring during the charge collection process is the main loss mechanism in solid-state dye-sensitized solar cells and charge injection and dye regeneration proceed with quantum yields close to unity.**
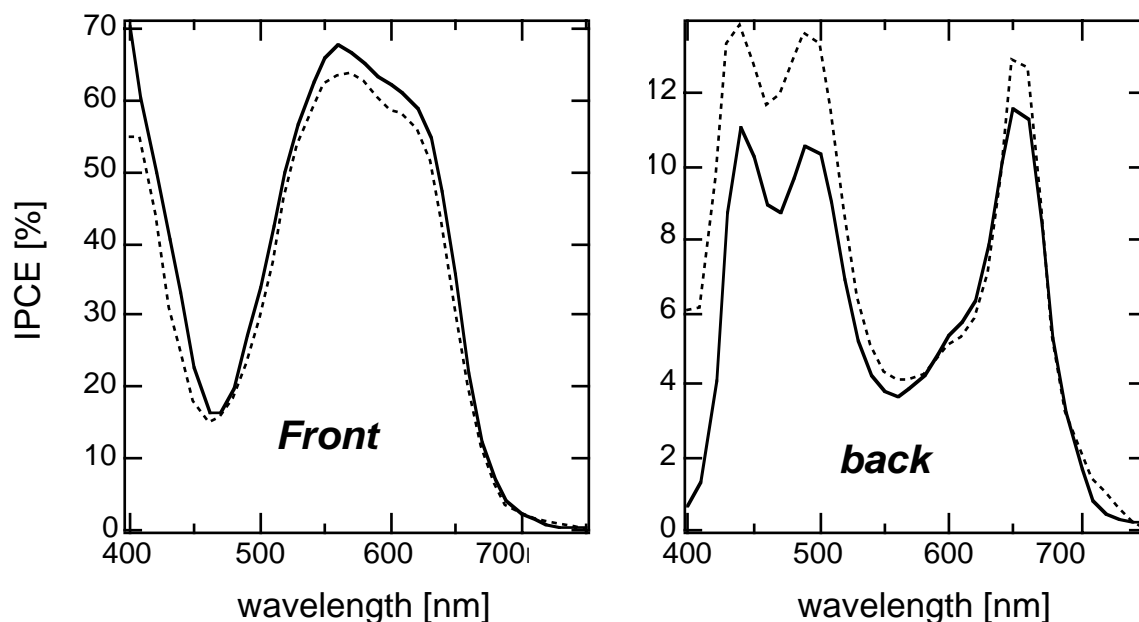
Figure 6.7 *Front-* and *back*side (b) illumination IPCE, as measured (plain line) and as calculated (dotted line) based on a value of 4.0 for β and an injection efficiency of 100 %. Beyond 550 nm the measured backside IPCE might be reduced due to the absorption of *spiro*-OMeTAD$^+$ in the *spiro*-OMeTAD matrix. The values shown are corrected for reflection and transmission losses caused by the window materials.

The IPCE spectra analysis and data processing was performed by means of a computer program (Igor pro, Wavemetrics). Input parameters were front-IPCE, back-IPCE, total transmission of the dye-sensitized film, total transmission and total reflection of the gold layer and the total transmission and reflection of the SnO_2 substrate. From these input parameters the corrected IPCE and APCE spectra were calculated as described before and the result displayed in a layout. In a second layout spectra according to the data analysis described in section I), II) and III) were calculated and displayed, allowing for the free choice of different input values for β in order to compare simulated and measured data.

From the layer thickness of 4.0 μm an electron diffusion length of 1 μm ± 12 % was derived. This indicates that it should be possible to improve the photovoltaic performance by suppressing the dark current or by using thinner films in combination with a diffuse reflector, placed behind the gold electrode. In the latter case the light would be backreflected into the photovoltaically active area of the cell,

instead of being absorbed in a region of minor photovoltaic activity. Figure 6.8 shows the calculated front-IPCE spectra for different device thicknesses, assuming a constant electron diffusion length of 1 µm and a back contact that reflects 100 % of the transmitted light. The spectra exhibit a striking similarity, showing that even with a 0.5 µm thick TiO_2 film comparable efficiencies can be obtained as with 4 µm thick films. A device based on a film thickness of about 1 µm seems to exhibit a slightly favorable photovoltaic performance, compared to thicker or thinner films. In addition to this thinner films would lead to devices with reduced series resistances and higher open circuit voltages.
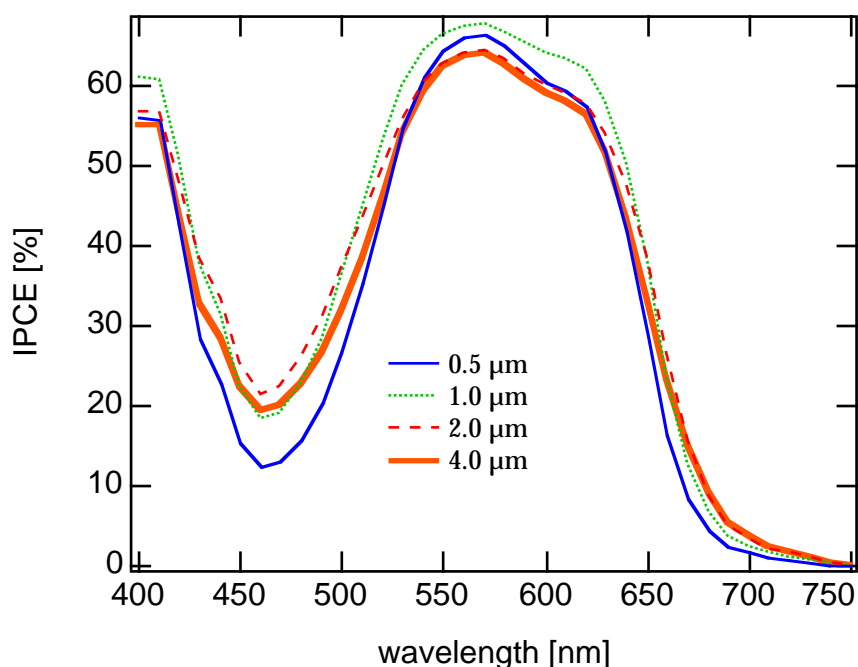
Figure 6.8 Calculated transmission-corrected front-IPCE spectra for different device thickness, assuming a constant electron diffusion length of 1 µm and a backcontact that reflects 100 % of the transmitted light. The calculations are based on the absorption spectrum of the device shown in Figure 6.2 (merocyanine Mc3 as sensitizer), assuming the same degree of dye loading (dye molecules adsorbed per unit surface area).

Quantification of β simply from the location of the back-IPCE maximum.

At the beginning of this chapter it could be seen that the maxima of the back-IPCEs do not necessarily correspond to the wavelength at which the devices show

their highest optical absorption. This is due to strong recombination inside the heterojunction. Photons, which are strongly absorbed by the film, will generate electron-hole pairs close to the back contact and far away from the SnO_2 electrode. However this region is not photovoltaically active as the recombination probability for the electrons on their long way to the working electrode is close to unity. At wavelengths of smaller optical densities the photons can penetrate deeper into the heterojunction, and finally reach the photovoltaically active region closer to the SnO_2 electrode, giving rise to an increase in the monochromatic photocurrent. However, at even lower optical densities the gain which is due to the more favorable distribution of electron-hole pair formation throughout the film is compensated by the general decrease in absorptivity inside the photoactive layer. Based on the simple recombination model (equation 6.14) we can now calculate the back-IPCE values for different values of beta as a function of the optical absorption of our sensitized heterojunction.

Figure 6.9 shows that the back-IPCE peaks at a defined absorption value for each β. The position of this maximum is independent of the efficiency of the initial charge carrier generation, which only influences its magnitude. Figure 6.10 shows the absorption, which gives rise to the highest back-IPCE as a function of β. At β values close to zero (negligible recombination) the back-IPCE does not show a maximum but rises constantly with increasing absortivity of the film. At very high β values the photovoltaically active area gets restricted to a very thin film in close vicinity to the SnO_2. In this case, the back-IPCE becomes proportional to the *transmission* of the device (which determines how much of the incident light intensity can reach the SnO_2 electrode) and its *absorbance* (which determines the capability of the thin photoactive area itself to absorb the remaining transmitted light):

$$IPCE^{back} \propto \left(A \cdot T = A \cdot 10^{-A} \right) \tag{6.15}$$

In this case the back-IPCE shows a maximum at a (decadic) absorption of $A = (Ln10)^{-1} = 0.434$ ($\alpha = 1$), which is the threshold for high beta values.
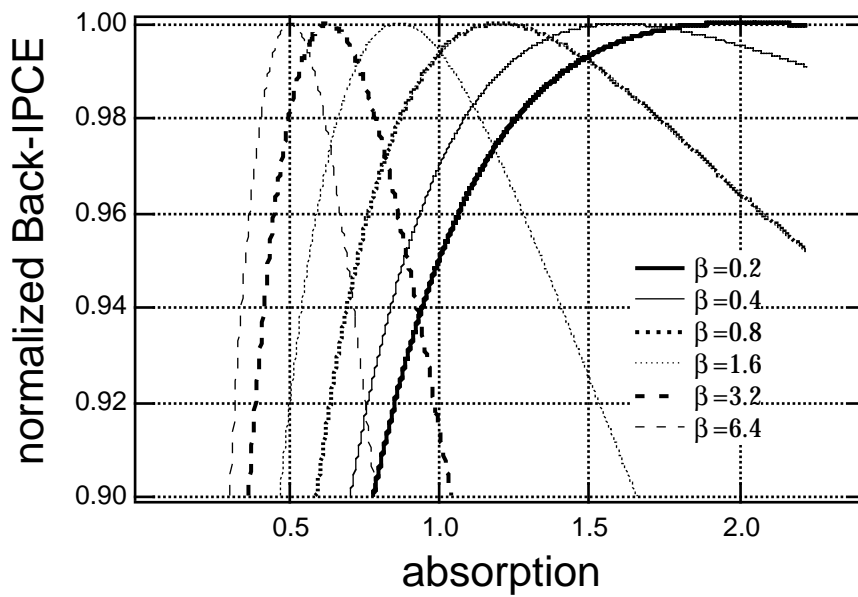
Figure 6.9 Normalized back-IPCE spectra, calculated via the simple recombination model, assuming a reflectivity of the SnO_2 electrode of 20%. For each beta value the maximum back-IPCE occurs at a defined absorption (A = alpha/Ln10) of the sensitized heterojunction, independent of the injection efficiency.
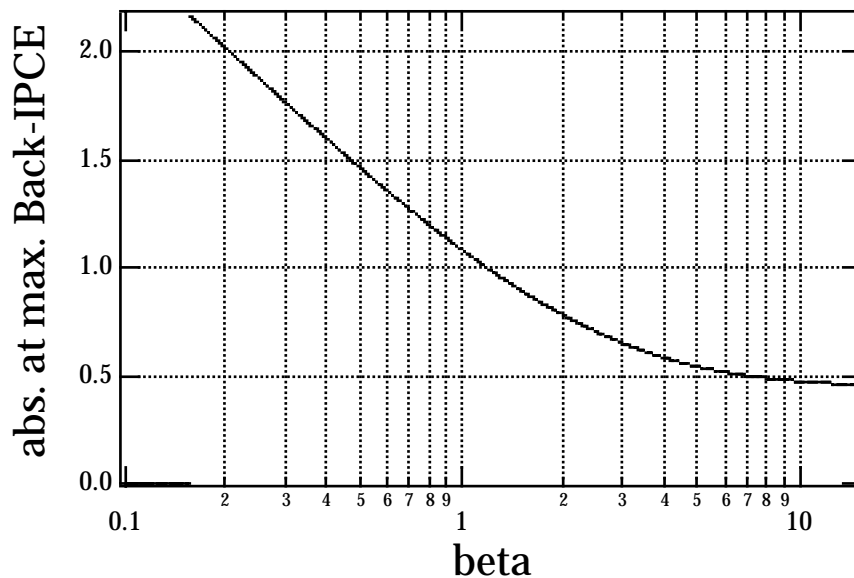
Figure 6.10 Absorption of the sensitized heterojunction layer at which the back-IPCE reaches its maximum as a function of the beta value. The values were derived from simulated curves as shown in Figure 6.9.

Especially if the β values range between 0.2 and 2 it should be possible to estimate them just from the optical absorption at which the maximum in the back-IPCE arises.

6.2 Comparison of different sensitizers

The sensitizer sets several limits to the overall photovoltaic performance. Its redox potentials $E(D/D^+)$ and $E(D^*/D^+)$ need to match the positions of the conduction band edge of TiO_2 and the redox potential of the hole conductor in order to allow for high quantum efficiencies of charge injection and dye regeneration (see Figure 1.3).

In contrast to classical photoelectrochemical solar cells weak absorption behavior of the sensitizer cannot be compensated by increasing the device thickness to about 10 – 20 µm. This, as the photovoltaically active layer in the cell is limited to a thickness of only about one micron. High light harvesting therefore requires sensitizers with high molar extinction coefficients over a wide spectral region of the solar spectrum and dense packing, when self-assembling on the semiconductor surface. In the following we will see that merocyanines are adequate sensitizers to meet these requirements.

In an ideal solar cell the bandgap of the absorber is equal to the cells built-in field (multiplied with e). Examples for such ideal behavior of organic solar cells can be found in literature[1]. Dye-sensitized photoelectrochemical solar cells however, show an unideal behavior in this respect, as 900 nm (about 1.4 eV) is currently the absolute absorption threshold, yielding an open-circuit voltage for an optimized device of 794 mV[2]. Despite an intense research effort within the last years no efficient IR sensitizer has been developed nor could the open circuit voltage be raised to more than 1.0 V. $Ru(dcbpy)_2(SCN)_2$ and $Ru(ctpy)(SCN)_3$ (tctpy = 4,4',4''-tricarboxy-2,2':6'2''-terpyridine) are still the most efficient sensitizers in photoelectrochemical solar cells up to date[2] (chemical structures see appendix).

In the following, a choice of sensitizers are compared, concerning their photovoltaic performance in solid-state dye-sensitized solar cells. Besides the commonly used ruthenium(II)polypyridyl sensitizers a series of merocyanine dyes was investigated. These dyes were thoroughly characterized, concerning their photophysical properties in the work of Frank Nüesch[3]. Their high molar

extinction coefficients, and quantitative injection efficiency in conjunction with TiO_2 made them very promising candidates for their application in the solid-state device.

Dye	$IPCE^{max}$ [%]	$\lambda(IPCE^{max})$ [nm]	I^{int} [mA/cm^2]
Mc2	50 ± 2	560	6.4 ± 0.2
Mc3	53 ± 0.6	560	6.3 ± 0.1
Mc4	37 ± 1.7	560	3.9 ± 0.15
perylene	23 ± 0.9	430	1.4 ± 0.09
Z636	44 ± 1.5	490	4.7 ± 0.15
$Ru(dcbpy)_2(SCN)_2$	42 ± 1.4	520	5.7 ± 0.2
$Ru(ctpy)(SCN)_3$	11 ± 0.4	600	2.3 ± 0.08

Table 6.2 Maximum IPCE-values measured under frontside illumination without any corrections concerning reflection and absorption losses due to the SnO_2 substrate. Furthermore the wavelength of the maximum IPCE and the short circuit current I^{int} calculated by convolution of the IPCE spectra with the solar spectrum (AM 1.5; 100 mW/cm^2) are indicated. However, the short-circuit currents measured under AM 1.5 conditiones were significantly smaller then I^{int}, as the maximum device currents were limited by the cells series resistances. To give an estimation of the reproducibility the standard deviation (σ_x^{n-1}) over four samples is indicated (±). Chemical structures of the dyes see appendix.
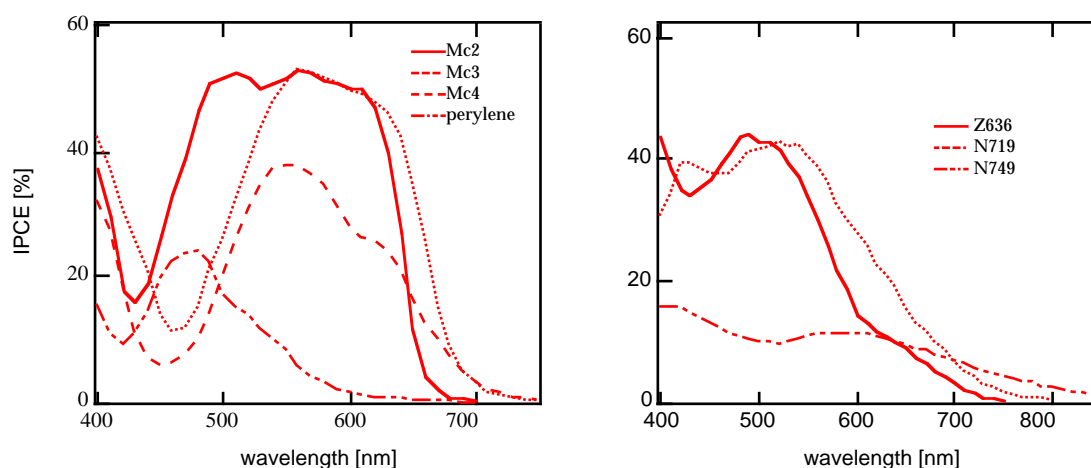
Figure 6.11 Uncorrected IPCE spectra measured under frontside illumination, using different sensitizers: Mc2 (0.053 mg/ml ethanol), Mc3 (0.028 mg/ml ethanol), Mc4 (0.027 mg/ml ethanol), perylene (0.026mg/ml CH_2Cl_2), Z636 (90% ethanol:10% DMSO), N719 (0.61 mg/ml tBuOH:CH3CN = 1:1) and N749 (1.03 10^{-3} M methoxyacetonitrile). The dyes were absorbed from above solutions for 48 hours at room temperature. All devices are based on 4 μm thick nanocrystalline TiO_2 electrodes and *spiro*-OMeTAD as hole conducting layer (0.070 mol% *spiro*-OMeTAD^{++}(PF$_6$)$_2$/*spiro*-OMeTAD, the spincoating solution contained 15 mM Li[(CF$_3$SO$_2$)$_2$N]). The counter electrode was a 10 nm thick gold layer.

Indeed the IPCEs having the highest peak values were measured with merocyanine dyes, resulting in the highest values in integrated current (see table 6.2). $Ru(dcbpy)_2(SCN)_2$ can partly compensate its somewhat lower peak-IPCE by the fact that its absorption spectrum extends further into the near infrared region. However, its integrated current is still about 10 % smaller, compared to Mc2 and Mc3.

The IPCE analysis derived in the previous chapter was applied to the above devices. Figure 6.12 shows the relation of frontside to backside IPCE as a function of the optical absorption, which the sensitized film exhibited at the IPCE observation wavelength. This graphical representation brings about the advantage that the recombination behavior of different dyes can be compared in a single graph, despite their completely different absorption features. Furthermore the data can be compared (as measured) without the implementation of any theoretical model – just by comparing the slopes. Table 6.3 shows the final result of the IPCE analysis. The Z636 sensitized device shows the least recombination effects with a mean free diffusion length of more than one micrometer, followed by the merocyanine dyes Mc2 and Mc3, with diffusion lengths of slightly less than one micron. Mc4 and the perylene dye show substantially stronger recombination, deteriorating the photovoltaic performance. Despite low recombination in Z636 sensitized devices their photovoltaic output is by far inferior to the merocyanine-based devices. This is mainly due to the much weaker light harvesting properties. While a 1 μm thick nanocrystalline TiO_2 film sensitized with Mc2 or Mc3 absorbs about 80 % of the incident light the same film sensitized with Z636 absorbs only 50 % (at the wavelength of their absorption maxima).

The calculated injection quantum efficiencies are all slightly larger than 100 %, indicating that electron injection and dye regeneration proceed with a quantum efficiency of unity. The fact that they extend 100 % is interpreted as an artifact (see above). The only dye showing low injection efficiencies is the perylene. Here the

analysis of the injection quantum efficiencies suggests that the formation of the initial electron-hole pair proceeds with a quantum efficiency of less than 80 %.
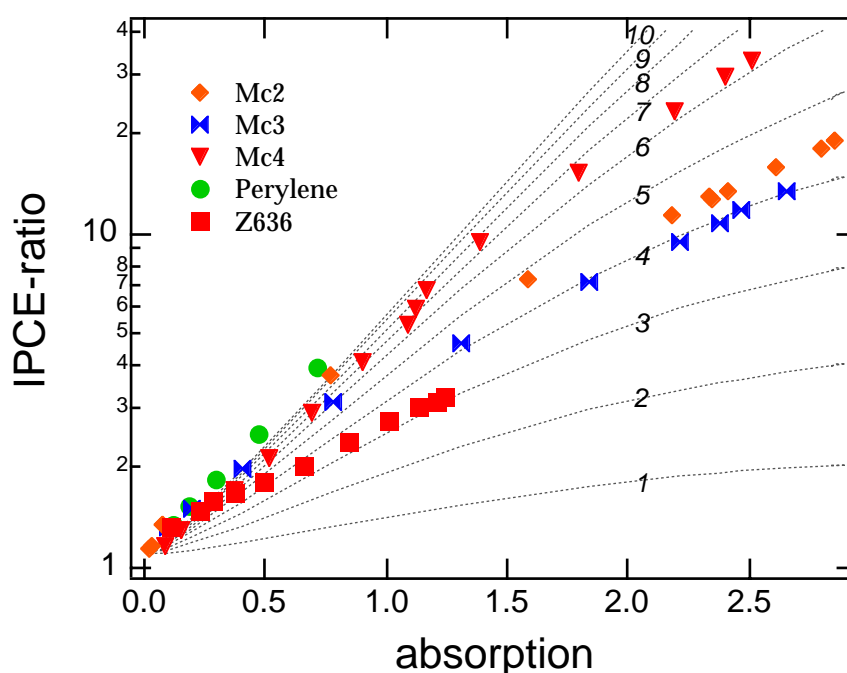
Figure 6.12 Ratio of (reflection & transmission corrected) frontside to backside IPCE for some of the dye-sensitized solar cells shown in Figure 6.11. The dotted lines represent the calculated dependence of absorption and IPCE-ratio, based on different values of β (as indicated).

From the above analysis we can conclude that the nature of the applied sensitizer does have a significant influence on the recombination kinetics, while almost all of the examined dyes showed unity quantum efficiency for the formation of the initial charge separated state. The fact that β depends on the nature of the sensitizer indicates that the presence of the dye molecules at the interface modulates charge recombination processes, following charge injection.

sensitizer	β	D [μm]	Φ_{inj}
Mc2	4.5	0.88	105 %
Mc3	4	1.0	106 %
Mc4	6 - 8	0.5 – 0.67	98 – 109 %
perylene	> 10	< 0.4	77 %
Z636	3 - 4	1 - 1.3	> 110 %

Table 6.3 Results yielded from backside/frontside IPCE analysis for different dyes. β represents the recombination parameter, D the free electron diffusion length resulting from β and the injection efficiency needed to superimpose calculated and measured front-IPCE spectra.

Possible mechanisms, explaining this observation are the interaction of the dye molecule with TiO_2 surface states, which play an important role in dye recombination. Further more the macroscopic dipole field resulting from the self-organized molecular dipoles at the interface was shown to effect charge recombination (for more details see chapter 7).

Figure 6.13 shows the comparison of three of the dye-sensitized solid-state devices introduced above with their photoelectrochemical counterparts. In order to create comparable conditions the photoelectrochemical cells were cut from the same substrates, which were used for the solid-state devices. For the assembly of the liquid junction dye-sensitized cells a lithium iodide/propylenecarbonate electrolyte was used which is generally known to strongly favor the electron injection behavior of sensitizers. The maximum IPCE of the solid state junction reaches about 72 % of the value of the photoelectrochemical cell in case of Mc2 and about 63 % for Z636 and N719 sensitized cells. This confirms the excellent photovoltaic performance of the solid-state analogues, which is comparable to that of photoelectrochemical cells.
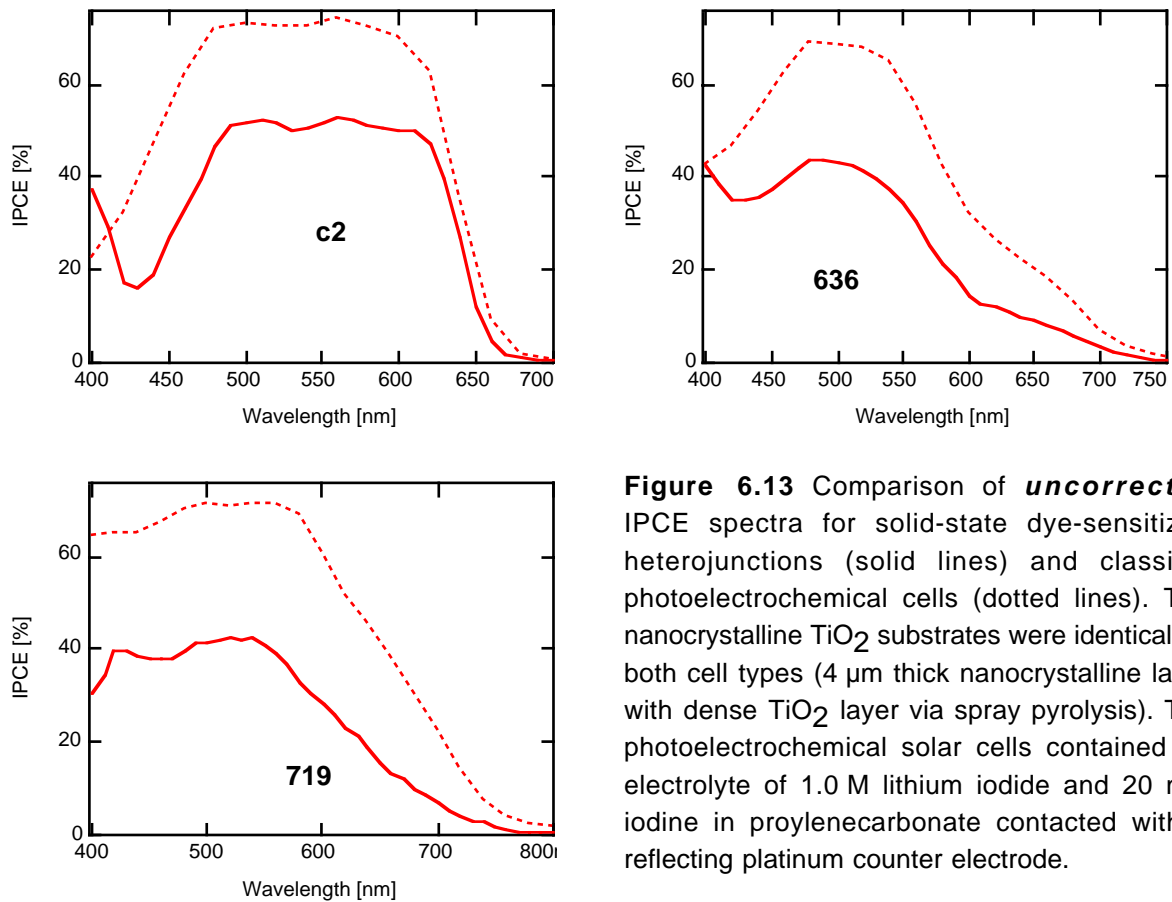
Figure 6.13 Comparison of *uncorrected* IPCE spectra for solid-state dye-sensitized heterojunctions (solid lines) and classical photoelectrochemical cells (dotted lines). The nanocrystalline TiO_2 substrates were identical for both cell types (4 μm thick nanocrystalline layer with dense TiO_2 layer via spray pyrolysis). The photoelectrochemical solar cells contained an electrolyte of 1.0 M lithium iodide and 20 mM iodine in proylenecarbonate contacted with a reflecting platinum counter electrode.

Interplay of doping concentration and recombination

The interfacial recombination of an electron in the conduction band of TiO_2 and a positive charge, sitting on a hole conductor molecule should be of first order with respect to both, electron and hole concentration. In solid-state dye-sensitized solar cells the concentration of *holes* should primarily be given by the degree of doping. The recombination probability of an electron migrating a distance dx towards the SnO_2 electrode should be proportional to the concentration of holes, so that

$$\beta \propto c(spiro - OMeTAD^+)$$

(6.16)

Figure 6.14 gives an example of how the doping concentration can influence the recombination in a solid-state dye-sensitized solar cell. Both, front- and back-IPCE significantly decrease upon an increase in dopant concentration. Figure 6.15

illustrates that the observed change can clearly be assigned to an increase in recombination occurring inside the cell while the injection efficiency remains unaltered. Analysis of the data yielded values of $\beta = 4.5$; $\Phi_{inj} = 105\%$ for $c(OMeTAD^{++}(PF_6)_2) = 0.070$ mol% and $\beta = 13\text{-}16$; $\Phi_{inj} = 100 - 120\%$ for $c(OMeTAD^{++}(PF_6)_2) = 0.24$ mol%.

The above findings suggest that IPCE values might be improved by a further decrease of the dopant concentration. However already 0.07 mol% doping with $OMeTAD^{++}(PF_6)_2$ had detrimental effects on the device performance under full AM 1.5 conditions (100 mW/cm^2). This was due to the high internal series resistance of the cell. The doping concentration therefore has to be optimized for each device thickness and the envisaged potential application (indoor/outdoor).
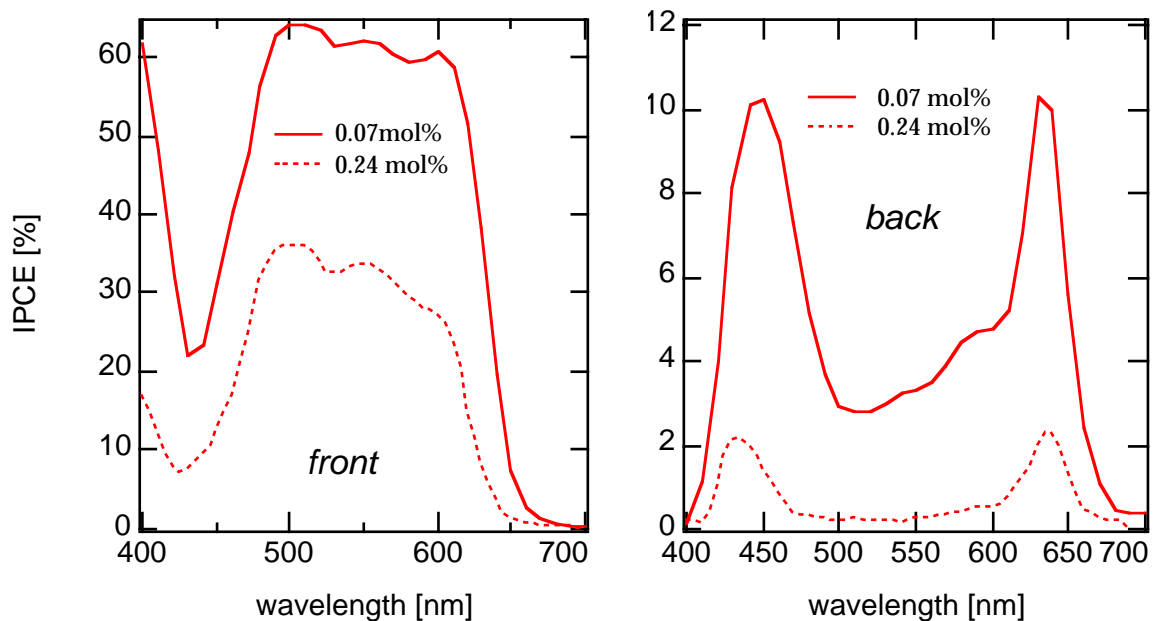
Figure 6.14 Frontside and backside illumination IPCEs (transmission corrected for optical losses due to the window materials) for two solid-state Mc2-sensitized solar cells, exhibiting different degrees of molecular doping with $OMeTAD^{++}(PF_6)_2$. The thickness of the nanocrystalline TiO$_2$ layer was 4 μm.
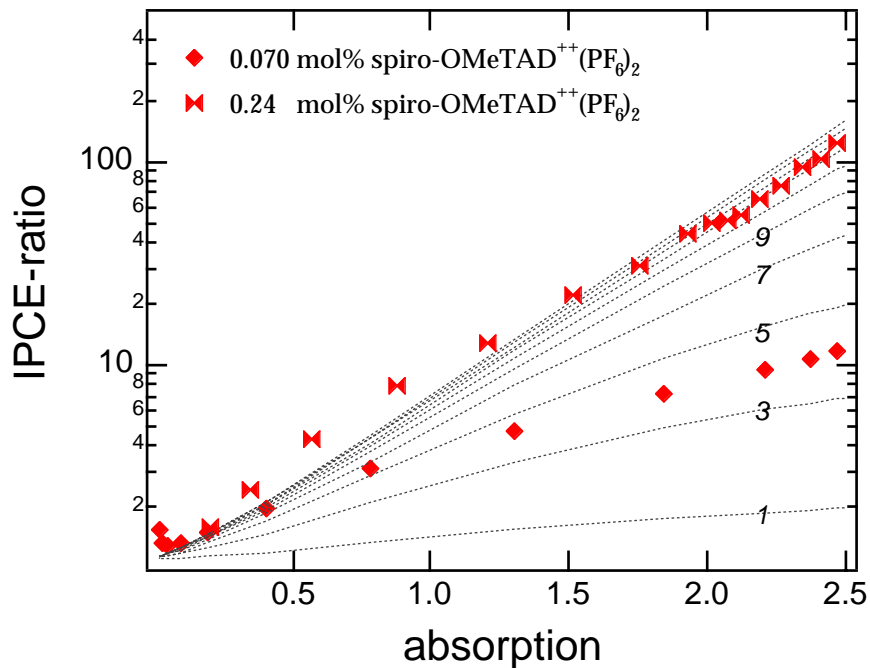
Figure 6.15 Ratio of (reflection & transmission corrected) frontside to backside IPCE for two Mc2 sensitized solar cells, exhibiting two different degrees of molecular doping with OMeTAD^{++}(PF$_6$)$_2$. The dotted lines represent the calculated dependence of absorption and IPCE-ratio, based on different values of β (as indicated).

6.3 Probing pore filling

There is some concern, whether and to what extent regions inside the porous TiO$_2$ layer remain unfilled after the spin coating procedure. As the spin-coated solution penetrates the TiO$_2$ film from its top, regions close to the SnO$_2$ surface might specifically suffer from poor pore filling (see Figure 6.16). SEM pictures at device cross sections gave some indication for this assumption, however they were not conclusive. In the following we shall see that analysis of the shape of the IPCE spectra is a powerful tool to conclude on whether regions close to the SnO$_2$ electrode remain unfilled.

oleconductor (+ TiO$_2$)

iO$_2$

upport
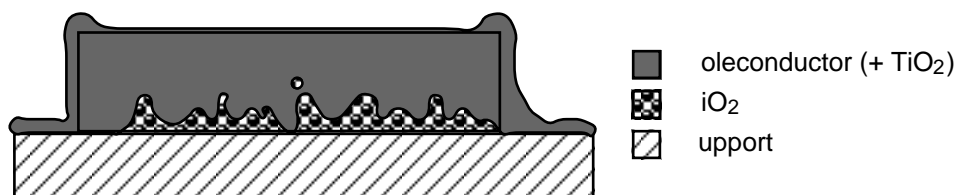
Figure 6.16 Cross section scheme of a dye-sensitized solid-state solar cell exhibiting unfilled pores close to the SnO$_2$ back contact.

A simple model shall be used to describe the phenomenon of incomplete pore filling where the hole conductor matrix only penetrates down to a certain depths of the film, leaving a fraction γ of the total TiO$_2$ film thickness d unfilled. Comparing the IPCE of the partially filled structure with a fully filled structure the following relation will be valid:
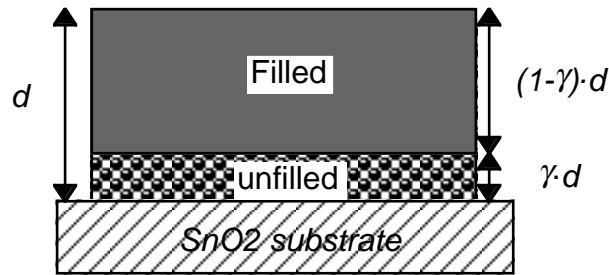
Figure 6.17 Simplified cross section scheme according to the model assumptions

$$IPCE = IPCE(\alpha') \cdot e^{-\gamma\alpha} \tag{6.17}$$

$$\alpha' = \alpha \cdot (1 - \gamma) \tag{6.18}$$

$\alpha =$ absorption of the photovoltaically active film according to T $=$e$^{-\alpha}$
$\alpha' =$ absorption of the filled part of the film
$\gamma =$ fraction of the film which stays unfilled

This relation contains two corrections. First of all the absorption of the photovoltaically active film, which is proportional to the thickness, will decrease by a factor (1-γ) and second, the unfilled fraction of the film, close to the SnO$_2$ surface will act as an inner filter and reduce the incident light intensity by a factor of e$^{-\gamma\alpha}$ (front side illumination mode). For a given degree of γ this inner filter effect gains in influence the stronger the absorption of the film is. To illustrate this two experimental IPCE curves were measured and simulated according to the model described in section 6.1.2. The dotted curve shows the experimental data (corrected for the absorption of the SnO$_2$ glass) while the curve labeled 100% corresponds to the best fit resulting from the frontside/backside IPCE analysis. Equation 6.16 was now used, to calculate the IPCE spectra, which would result from an incomplete pore filling of the device. Figure 6.18 shows this data for a

solar cell based on a 4 μm thick TiO_2 film, sensitized with a merocyanine dye. As could already be seen in the previous chapter, there is an impressive agreement between the experimental data and the obtained fit, clearly demonstrating the strong influence of charge recombination on the photovoltaic performance. It also shows drastically, how the spectral shape of the IPCE, as well as its magnitude would change upon minor irregularities of the pore filling. Already if 7.5 % of the pores would remain unfilled a minimum instead of a maximum would be expected at the point of maximum absorption of the film (570 nm), while already changes as small as 2.5 % would lead to a distinct derivation in the spectral shape of the IPCE. It is also important to point out that incomplete pore filling and the presence of recombination influence the spectral shape towards different extremes. In *absence* of recombination the IPCE curve would exhibit a plateau between 520 and 630 nm, as the absorptivity of the film is superior to 95 % over this whole range. Recombination however limits the photovoltaically active region in the film to a thin layer close to the SnO_2. The absorption of this thin layer is much smaller than that of the total width of the film (maximum decadic absorbance less than 1). This results in a well-defined maximum in the front-IPCE spectrum. It is interesting to note that recombination and incomplete porefilling influence the shape of the front IPCE spectrum towards two different extremes.

Figure 6.19 illustrates that the expected spectral change upon imperfect porefilling is much less obvious if the test cell exhibits a much weaker absorption. The maximum (decadal) absorbance of the Mc3 sensitized junction was A = 3.0, while only reaching 1.2 for the Z636 sensitized cell. The calculated spectra for the Z636 junction does not exhibit a local minimum at the point of maximum absorption, even when 15 % of the pores stay unfilled. Again strongly absorbing films are shown to be highly sensitive, allowing the analysis of the smallest deviations in the structure and property of the junction. The examples shown above clearly indicate that incomplete porefilling which affects areas very close to the SnO_2 surface can be ruled out as loss mechanism. Incomplete pore filling which is distributed *homogeneously* over the whole junction area can not be probed with the method shown above. However IPCE values of nearly 70 %, and the fact that

charge recombination could be clearly specified as an important loss mechanism does not leave much space for arguing for incomplete pore filling. In particular as the analysis of frontside/backside IPCE's yields values for the charge injection efficiency close to unity.

The argument carried out above is only valid under the assumption that lateral hole transfer inside the sensitized layer is not efficient enough to completely mask the effect of incompletely filled pores. However if this was true porefilling would be no longer a loss mechanism in the cell. But still devices based on dye-sensitized TiO_2 films (4 μm) sandwiched between a SnO_2 and a gold electrode do not give rise to significant cell currents, suggesting that 2-dimensional hole hopping inside the dye layer is not efficient over larger distances.
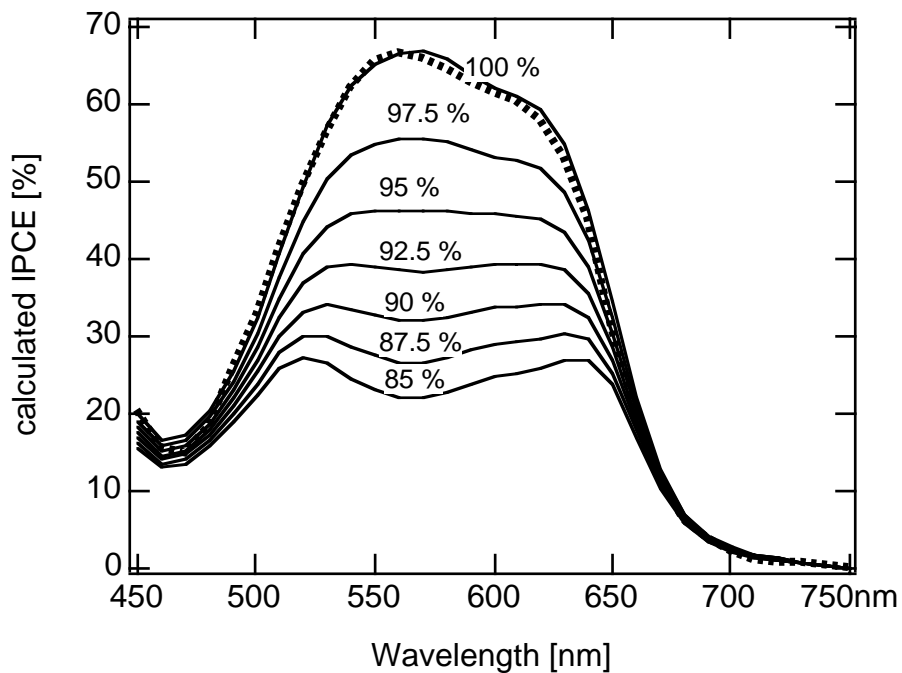
Figure 6.18 IPCE spectrum of a dye-sensitized solar cell based on a 4 μm thick TiO_2 film, coated with a merocyanine dye (Mc3, dotted line) and calculated IPCE spectra, assuming different penetration depths of the hole conductor matrix. 90 % corresponds to 10 % of the layer thickness being unfilled in close vicinity to the SnO_2 contact, while the top 90 % of the film are completely filled. The calculations are based on the UV/VIS spectrum of the Mc3 derivatized TiO_2 layer after spin coating, a mean free electron path length of 1.1 μm and an injection efficiency of 100 %. Transmission losses due to the SnO_2 glass and reflections at the gold back contact were also considered.
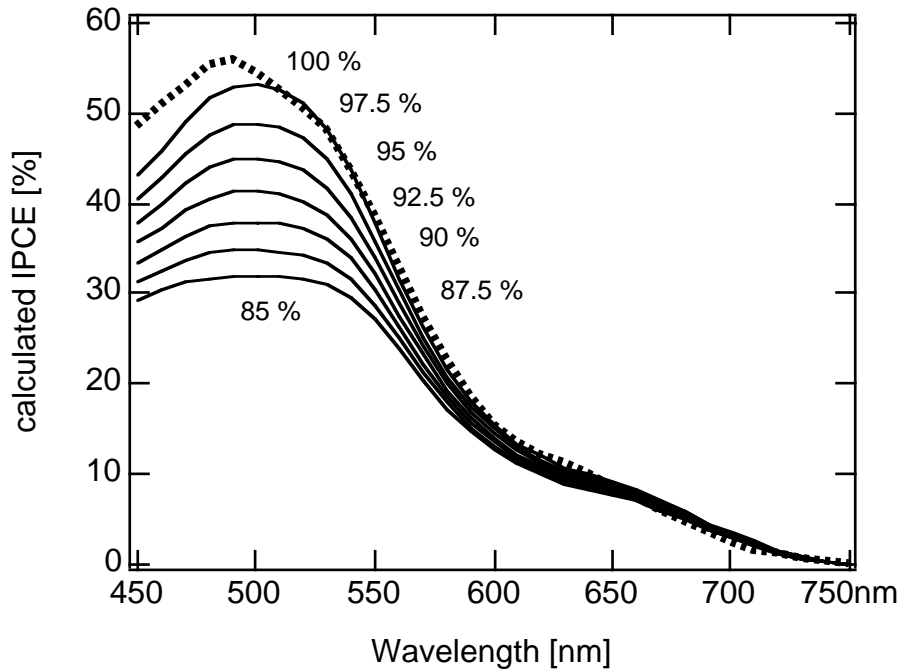
Figure 6.19 Measured and calculated IPCE spectra for a solid-state solar cell based on the dye Z636. All conditions are analog to the data shown in Figure 6.18 except for the mean free electron path length being 1.6 μm.

6.4   White-light response

Figure 6.20 and Table 6.4 show typical current-voltage characteristics for a solid-state dye-sensitized solar cell under different illumination conditions. The short-circuit current I_{sc} exhibits a linear dependence on the illumination intensity ($power_{in}$), except for very low illumination intensities, where a slightly superlinear behavior is observed. The open-circuit voltage V_{oc} shows a logarithmic dependency of the incident light power, with an increase of 70 mV per decade ($\frac{\delta V_{oc}}{\delta \ln(Power_{in})} = 30.5 \ mV$). The fill factor (FF) clearly decreases at illumination intensities close to one sun. Figure 6.20 shows that this can clearly be assigned to the high series resistance of the cell. The sharp decrease in fill factor also causes a decrease in overall efficiencies at higher light levels. Reduction of the cell's resistance would therefore result in a significant improvement in cell performance. This can most advantageously be realized by reducing the film

thickness, rather than by increasing the doping concentration, as the latter showed to decrease the quantum efficiency of charge collection.
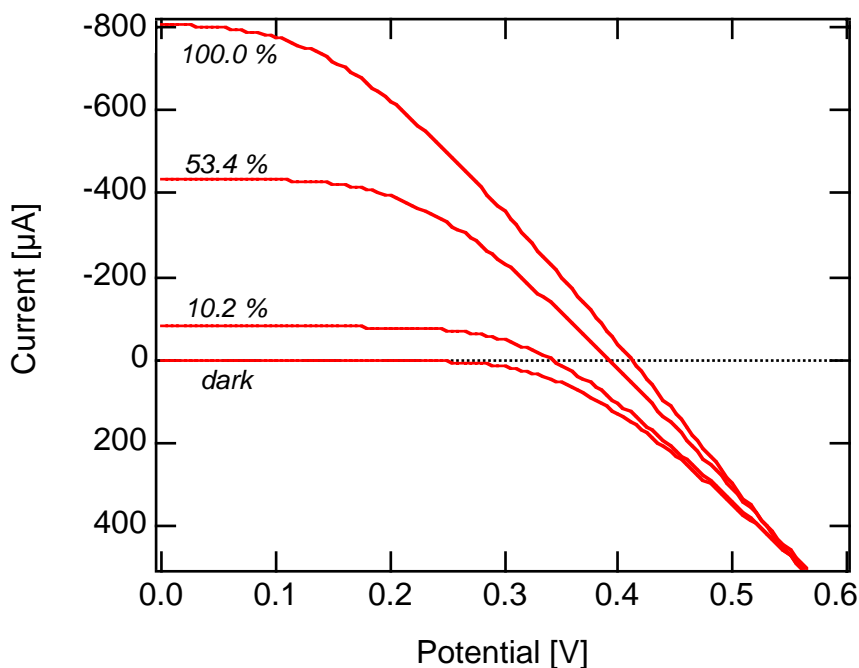
Figure 6.20 Current-voltage characteristics of a solid-state Mc2-sensitized solar cell at different light intensities (indicated in % of AM 1.5/100 mW/cm^2). The active surface area of the device was 0.18 cm^2. The cell is based on 4 µm thick nanocrystalline TiO$_2$ layers. The *spiro*-OMeTAD hole conductor matrix was doped with 0.18 mol% [N(p-C$_6$H$_4$Br)$_3$][SbCl$_6$]. The spincoating solution was 15 mM in Li[(CF$_3$SO$_2$)$_2$N]. The thickness of the counter electrode was 20 nm.

Power$_{in}$ [µW/cm^2]	I$_{sc}$ [µA/cm^2]	U$_{oc}$ [mV]	FF [%]	η [%]
0.89	37.43	267.5	64.5	0.73
10.2	450.38	341.9	65.3	0.99
53.4	2425	392.4	48.5	0.86
100.0	4480	411.8	38.2	0.70

Table 6.4 Photovoltaic data for the solid-state device shown above.

6.5 Controling the open circuit voltage using 4-tert-butylpyridine

Dye-sensitized photoelectrochemical solar cells have been shown to experience a considerable improvement in photovoltaic performance when 4-tert-butylpyridine was added to the electrolyte. The mechanism of this effect is not yet fully understood. Nazeerudin and co-workers[4] observed a shift in the dark current onset of 200 mV, when the sensitized electrodes were dipped for 15 min in 4-tert-butylpyridine. The open-circuit voltage (Voc) increased from 0.38 to 0.66 V while the short-circuit current (Isc) remained constant. The authors rationalized the effect in terms of 4-tert-butylpyridine adsorption at the TiO_2 surface blocking surface states that are active as intermediates in the interfacial charge recombination. They presumed that these sites are represented by Ti(IV) ions on the surface, which, due to their Lewis acidity, are prone to interact with the pyridine derivative. Similar results were obtained by Huang and co-workers[5], who attributed the observed increase in Voc to either a charging of surface states or a shift of the conduction band edge.

To study the influence of 4-tert-butylpyridine on solid-state dye-sensitized solar cells two different approaches were pursued – *pretreatment* of the sensitized electrodes with solutions of 4-tert-butylpyridine or direct addition (*co-treatment*) of 4-tert-butylpyridine to the spin-coating solution (results see Table 6.5).

A dramatic improvement in the photovoltaic performance is observed upon both, pre- and co-treatment. In case of the *pretreatment* Uoc increased by 77 mV, while Isc and the fill factor (FF) also showed small improvements. When 4-tert-butylpyridine is incorporated into the *spiro*-OMeTAD matrix a 16 % increase in short-circuit current can be observed, while Uoc more than doubles. Re-measuring the *co-treated* device, using a black mask to define the illuminated surface area yielded an efficiency of typically 1.75 %, showing that the general assumption (less the 10 % decrease due to surface area masking) is not valid for this sample. The best performance achieved with an appropriate mask was 1.83 %.

Electrode treatment	I_{sc} [μA/cm^2]	U_{oc} [mV]	FF [%]	η [%]
untreated	385±10	351±0.9	66±0.9	0.91±0.04
pretreated	399±25	428±14	69±0.7	1.23±0.11
co-treated	448±7	704±3.8	65±1.6	2.08±0.13

Table 6.5 Photovoltaic performances of three types of solid-state dye-sensitized solar cells at an illumination intensity of 1/10 sun (corresponding to AM1.5 10 mW/cm^2). The cells are based on 4 μm thick nanocrystalline TiO$_2$ layers sensitized with Ru(dcbpy)$_2$(SCN)$_2$. The *spiro*-OMeTAD hole conductor matrix was doped with 0.18 mol% [N(p-C$_6$H$_4$Br)$_3$][SbCl$_6$]. The spincoating solution was 15 mM in Li[(CF$_3$SO$_2$)$_2$N]. The thickness of the counter electrode was 20 nm.. The **pretreated** devices were exposed to a solution of 1.0 M 4-tert-butylpyridine in acetonitrile for 30 minutes, prior to the spin coating of the hole conductor. The **co-treated** samples contained 0.2 M 4-tert-butylpyridine in the *spiro*-OMeTAD spin-coating solution. The co-treated device was re-measured, using a black mask to control the illuminated surface area. The efficiency η measured under these corrected conditions was 1.75±0.11 %. To give an estimation of the reproducibility the standard deviation (σ_x^{n-1}) over four samples is indicated (±)

These are very exciting and encouraging results, especially in view of the very preliminary nature of these experiments. Questions concerning the influence on the cell stability and the underlying mechanistic effects will have to be addressed in the near future. Further optimization should allow for the development of solid-state dye-sensitized solar cells with overall efficiencies exceeding 2 % !

6.6 The Counter electrode

In pn-junction solar cells the contact materials of the junction need to provide ohmic contact to the p- and n-type material respectively. Once this requirement is fulfilled the built-in field of the junction and thereby the open circuit voltage should solely be determined by the workfunction differences of the p-type and n-type semiconductor. This stands in contrast to Schottky diode solar cells, where the actual workfunction of the *contacting metal* determines the built-in field of the junction[6-8]. To show the validity of this assumption a series of devices was made where gold and platinum are compared as contact materials of *spiro*-OMeTAD. The two metals exhibit a workfunction difference of about 550 meV (Au 5.1 eV; Pt 5.65 eV)[9]. However they both form ohmic contacts with *spiro*-OMeTAD, as could be seen from the current-voltage characteristics of SnO$_2$/*spiro*-OMeTAD/*metal* junctions. Table 6.6 compares the photovoltaic performances of devices with gold and platinum counter electrodes. The

differences in Isc, Uoc and the energy conversion efficiency are inside the experimental error. Only the fill factor seems to be slightly higher, when gold was uses as counter electrode.

Counter electrode	I_{sc} [$\mu A/cm^2$]	U_{oc} [mV]	FF [%]	η [%]
Pt	154±15	487±4	59±4	0.34±0.02
Au	143±2	481±9	65±1	0.34±0.01

Table 6.6 Comparison of two sets of solid-state $Ru(dcbpy)_2(SCN)_2$-sensitized solar cells, employing two different types of counter electrode materials: a) sputtered platinum (60 nm); b) gold (20 nm) deposited via thermal evaporation.

We therefore conclude that the open circuit voltage of solid-state dye-sensitized solar cells does *not* depend on the workfunction of the contacting metal, as long as this provides an ohmic contact. Further materials showing ohmic contact behavior to *spiro*-OMeTAD were graphite, silver and PEDOT (polyethylenedioxothiophene polystyrolesulfonate; *Baytron P*, Bayer AG/ Germany).

References

1)   Granström, M.; Petrisch, K.; Arias, A. C.; Lux, A.; Andersson, M. R.; Friend, R. H. *Nature* **1998**, *395*, 257-260.

2)   Grätzel, M. *Properties and Applications of nanocrystalline electronic junctions*; Nalwa, H. S., Ed.; Academic Press, 2000; Vol. 3, pp 527-541.

3)   Nüesch, F. A. *From monomer to the solid state. A photophysical investigation of a merocyanine dye*; Ecole Polytechnique Fédéral de Lausanne: Lausanne, 1995.

4)   Nazeeruddin, M. K. et al. *J. Am. Chem. Soc.* **1993**, *115*, 6382-6390.

5)   Huang, S. Y.; Schlichthörl, G.; Notzik, A. J.; Grätzel, M.; Frank, A. J. *J. Phys. Chem. B* **1997**, *101*, 2576-2582.

6)   Martin, M.; André, J.-J.; Simon, J. *J. Appl. Phys.* **1983**, *54*, 2792-2794.

7)   Simon, J.; André, J. J. *Molecular semiconductors*; Springer-Verlag: Berlin, 1985.

8)   Sze, S. M. *Physics of semiconductor devices*; John Wiley & Sons: New York, 1981.

9)   *Handbook of Chemistry anad Physics*; 57th ed.; CRC Press: Cleveland, 1976.

Chapter 7

Dipole modified junctions of *spiro*-OMeTAD & TiO$_2$

Metal and semiconductor surfaces modified with self-assembled monolayers of organic molecules exhibit work functions different to unmodified substrates. This observation was attributed to the presence of dipole fields, building up upon self-assembly of molecular dipoles on a surface (see Figure 7.1). In organic LEDs this effect is widely used to improve charge injection at metal/organic semiconductor interfaces[1,2]. The dipole modification diminishes the workfunction difference between the two materials, thereby removing charge injection barriers. So far this concept has never been applied to dye-sensitized heterojunctions and only once to pn-heterojunctions[3] (CdTe/CdS). An improvement of the photovoltaic performance is expected upon tuning of the built-in field by introduction of an organic dipole layer.

To show the feasibility of this approach the following strategy was pursued:

1) Selection of a series of similar molecules with dipole moments spanning over a wide range
2) Verification of the formation of an ordered self-assembled monolayer (adsorption isothermes)
3) Direct observation of the workfunction shift induced via the surface modification (Kelvin-Probe technique)
4) Preparation of dipole-modified heterojunctions to observe the effect of the dipole field on the current-voltage characteristics
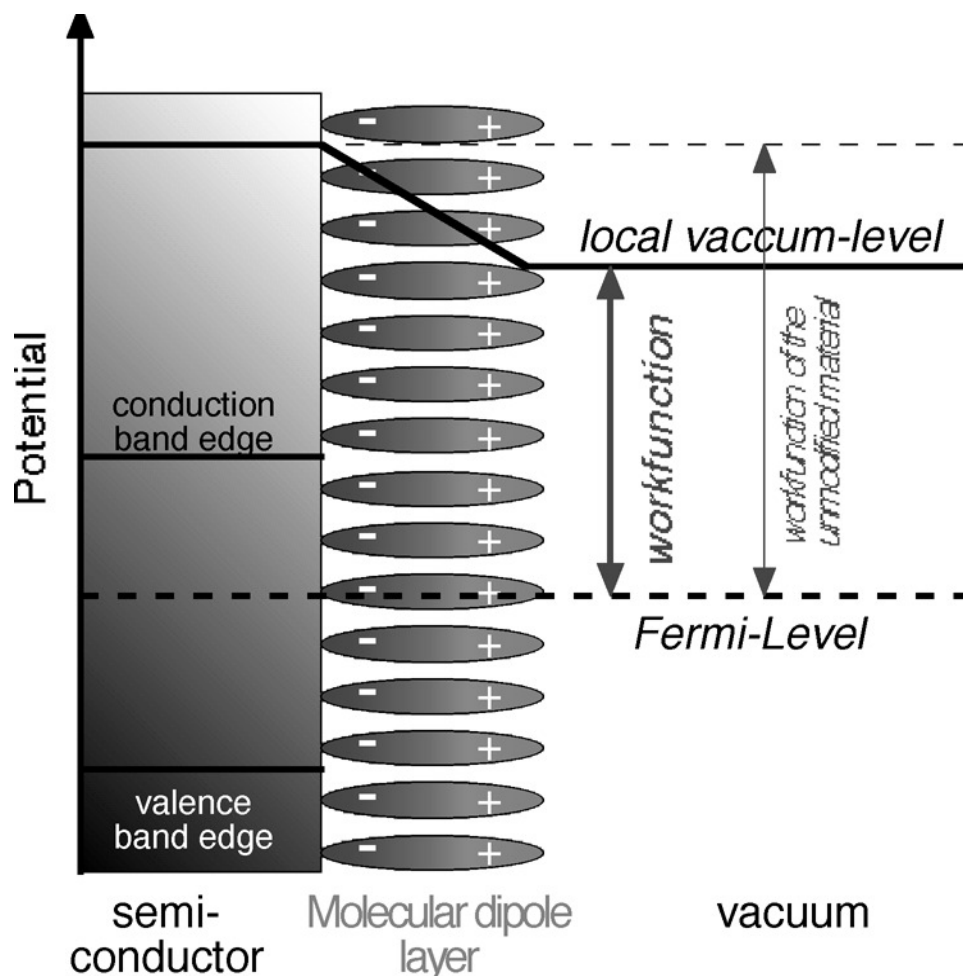
Figure 7.1 Band diagram of a semiconductor/vacuum junction modified with a molecular dipole layer. The workfunction difference between the modified and the unmodified junction corresponds to the potential drop induced by the dipole field.

Figure 7.2 shows the series of molecules which were chosen for the surface modification of TiO_2. Each of the para-substituted benzoic acids bears a carboxy group which is known to strongly interact with TiO_2 and a substituent in para-position which, by its electron withdrawing or electron donating character strongly affects the molecular dipole moment. The binding mode of carboxylic acids to TiO_2 was subject to contradictory proposals and discussions in literature. However recently low energy electron diffraction experiments (LEED) on formic acid adsorption conducted on anatase single crystals gave evidence for a dissociative mechanism, with the formate binding to a fivefold coordinated titanium atom, while the proton is transferred to a surface O_2^--site[4]. These observations were recently confirmed by density functional calculations[5]. The

relative difference in dipole moment for the surface adsorbed species is assumed to be equivalent to the ones calculated for the substituted benzenes, with the dipole contribution of the dissociated carboxylic acid being the same for all the molecules.
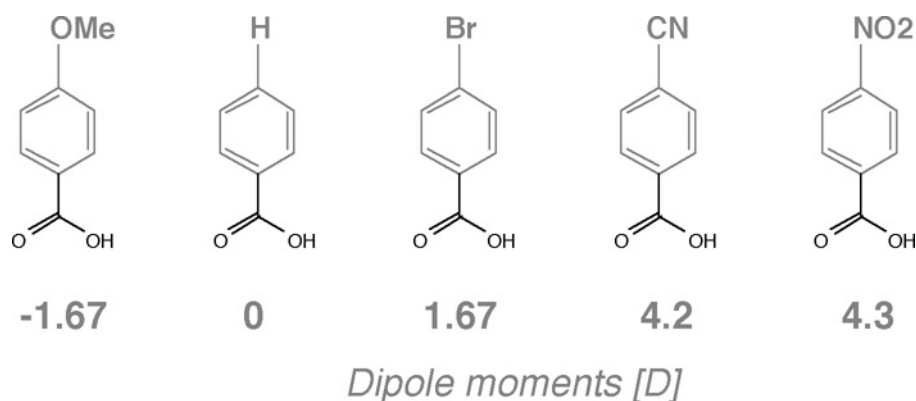
Figure 7.2 Structure formula of the benzoic acids used for surface modification. The dipole moments indicated are those, calculated for the substituted benzenes[6].

7.1   Adsorption behavior of benzoic acids on TiO_2

The formation of self-assembled monolayers upon absorption from solution was verified by recording absorption isotherms. Nanocrystalline TiO_2 films on glass were used as substrates. The specific surface area of the applied TiO_2 was calculated from the film volume and the specific surface area per film volume, derived from BET-measurements. The films were prepared as described elsewhere[7], heated in oxygen at 450 °C and exposed to the adsorbate solution for 24 hours (concentration: 1 mM; solvent acetonitrile p.a.). The ratio of TiO_2 to adsorbate solution was chosen differently for each concentration so that each time a change in concentration of about 40 – 60 % was induced. By this technique experimental errors could be minimized. Concentrations of the benzoic acids before and after the adsorption process were derived from the characteristic UV/VIS adsorption of the benzoic acid solutions. Nanocrystalline TiO_2 substrates proved to be superior over TiO_2 powders for these measurements, as they were easily removed from the solution, without leaving trace impurities of TiO_2

colloids. Such colloids can introduce a significant experimental error due to their strong absorption in the UV.

The amount of substance adsorbed per TiO_2 surface area as a function of the equilibrium concentration of nitrobenzoic acid is shown in Figure 7.3 a). The absorption isotherm saturates at higher concentrations showing no tendency to form double layer. When the ratio of equilibrium concentration to the amount of substance absorbed is plotted against the equilibrium concentration, as shown in Figure 7.3 b), a linear relation is observed, indicating Langmuir-type adsortion behavior. Analysing the adsorption isothermes according to the Langmuir formalism (see equations 7.1 – 7.3) yielded values for the adsorption equilibrium constant (K), the surface concentration of adsorbate (Γ_{max}) and the occupied surface area per adsorbed molecule (F_D) at monolayer coverage for methoxybenzoic acid and nitrobenzoic acid (see Table 7.1)[5].
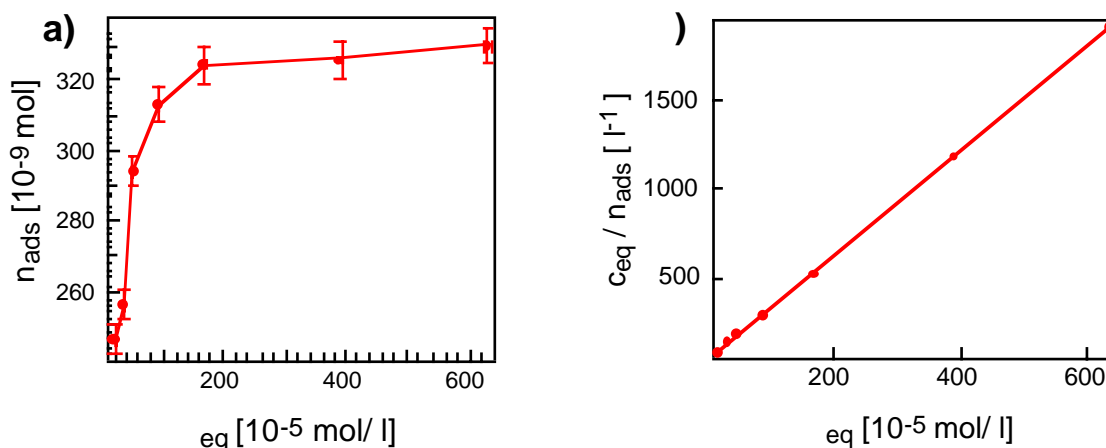
Figure 7.3 a) Adsorption isotherme for the adsorption of nitrobenzoic acid on nanocrystalline TiO_2 substrates from acetonitrile solutions. The amount of substance adsorbed and the equilibrium concentrations were derived from UV/VIS spectroscopy. b) The ratio of the equilibrium concentration to the amount of substance absorbed is plotted against the equilibrium concentration. Adsorption isothermes exhibiting Langmuir behavior show linear dependencies in this plot.

---

[5] The Langmuir isotherme is based on the assumption that a fixed number of identical adsorption sites compete for adsorption of an adsorbate from solution, leading to an adsorption/desorption equilibrium. The adsorption probability to an empty site is independent of the general surface coverage.

$$K = \frac{\vartheta}{(1-\vartheta) \cdot c_{eq}} \qquad (7.1)$$

$$\vartheta = \frac{n_{abs}}{n_0} = \frac{\Gamma}{\Gamma_{max}} \qquad (7.2)$$

$$\frac{c_{eq}}{n_{abs}} = \frac{1}{n_0 \cdot K} + \frac{1}{n_0} \cdot c_{eq} \qquad (7.3)$$

ϑ = degree of surface coverage
c_{eq} = equilibrium concentration of the adsorbate in solution
n_{abs} = adsorbed amount of substance per unit surface area
n_0 = adsorbed amount of substance per unit surface area at monolayer coverage

While the surface areas occupied per molecule are comparable for both substances the absorption constants differ by about one order of magnitude. While 50 % surface area coverage ($1/K$) for nitrobenzoic acid is already reached at an equilibrium concentrations of $7.5 \cdot 10^{-6}$ mol/l this coverage is established only at concentrations of 9.4×10^{-5} mol/l for methoxybenzoic acid. Differences in the acidity of the carboxy group of both components (about one pka unit) are likely to be the reason for the observed change in absorption energetics. Particularly as the absorption mechanism was postulated to be dissociative.

adsorbate	K [l/mol]	Γ_{max} [μmol/m^2]	F_D [Å^2]
methoxybenzoic acid	$1.06 \cdot 10^4$	5.1	32.6
nitrobenzoic acid	$1.34 \cdot 10^5$	5.4	30.8

Table 7.1 Adsorption equilibrium constant (K), surface concentration of adsorbate (Γ_{max}) and occupied surface area per adsorbate molecule (F_D) at monolayer coverage for two substituted benzoic acids as extracted from Langmuir plots as shown in Figure 7.3.

Adsorption of benzoic acid derivatives onto TiO_2 were found to obey the Langmuir isotherme. Under the adsoption conditions employed for the surface modification the formation of a complete monolayer can be presumed.

7.2   Workfunction changes induced by surface modification.

TiO$_2$ substrates were surface modified by immersing them in 1 mM solutions of the benzoic acid derivatives. Their contact potential differences were measured using a Kelvin probe apparatus[8], mounted in a glove box. A linear relationship was found between the observed workfunction change (equivalent to the observed change in contact potential difference) and the molecular dipole moment(see Figure 7.4). The change in surface potential induced by a self-assembled monolayer of dipolar molecules is a function of the molecular dipole itself (p), the surface coverage (Γ), the angle between the dipole and the surface normal (θ) and the permittivity of the organic monolayer ($\varepsilon\varepsilon_0$):

$$\Delta V = \frac{\Gamma \cdot p \cdot \cos\theta}{\varepsilon\varepsilon_0} \hspace{4cm} (7.4)$$

The linear relationship observed in Figure 7.4 proposes, that each of the benzoic acids adsorbed exhibits similar values for the surface coverage, the binding angle in respect to the surface and the net contribution of the dissociated carboxy group to the molecular dipole moment. Similar results were reported for the adsorption of benzoic acids on GaAs[9], CdTe[10] and ITO[11]. There is some concern, that the difference in acidity observed for the 5 benzoic acids (spanning the range of one pka unit) might contribute to some extend to the observed effects of surface modification. Such concerns are substantiated by the observed pH dependence of the flatband potential of TiO$_2$ (60 mV shift/pH unit)[12] and the experiments conducted by Nüesch et al.[13], who observed a workfunction change of ITO upon modification with acids and bases.
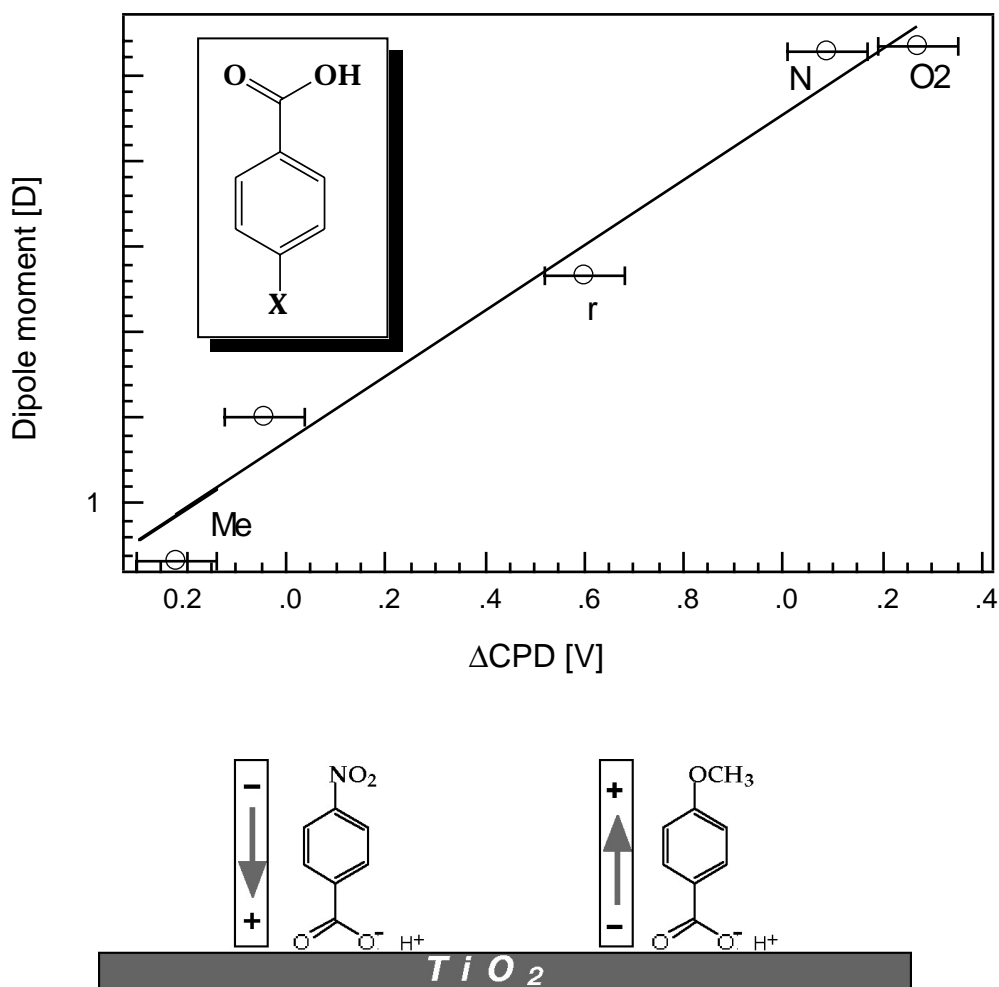
Figure 7.4 Workfunction changes (ΔCPD) of TiO$_2$ induced by surface modification with benzoic acid derivatives (x = OMe, H, Br, CN and NO$_2$). TiO$_2$ samples were immersed in the corresponding benzoic acid solutions (1 mM in acetonitrile for 24 h) and the workfunction shift measured relative to a reference sample, stored in pure acetonitrile. A Kelvin probe apparatus with a vibrating gold grid was used. The sample preparations and measurements were performed under argon atmosphere. The dipole moments indicated are equivalent to those shown in Figure 7.2. Below the direction of the molecular dipole moment of *p*-methoxy- and *p*-nitrobenzoic acid relative to the surface is shown schematically.

However the observed change in surface potential, differing by about 1.4 V from methoxybenzoic acid to nitrobenzoic acid can not be rationalized in terms of the marginal pka difference of one pka unit.

7.3 Diode modification of TiO$_2$/*spiro*-OMeTAD heterojunctions

Dipole modification with benzoic acids induced changes in the surface potential of TiO$_2$ of up to 1.4 V proving the presence of a strong dipole field. In the following section the influence of this dipole field on the electronic properties of a derivatized TiO$_2$/*spiro*-OMeTAD junction shall be discussed.
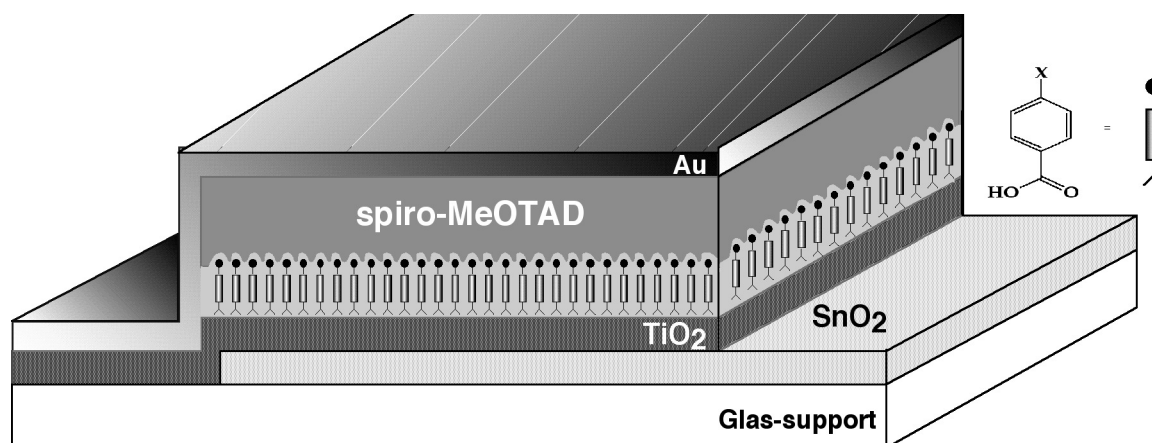
Figure 7.5 Scheme of the device geometry. A thin (50 nm) TiO$_2$ layer was applied on pre-structured SnO$_2$ glass via spray pyrolysis, immersed in the adsorbate solution for about 24 hours and spincoated with *spiro*-OMeTAD (2 μm) from a chlorobenzene solution. The backcontact was formed by evaporation of a 20 nm thick gold layer. The hole conductor layer was doped by adding 0.1 mol% N(*p*-C$_6$H$_4$Br)$_3$][SbCl$_6$ to the spin coating solution.

Thin films of TiO$_2$ were applied to SnO$_2$ electrodes via spray pyrolysis[14], forming a thin, pinhole free layer of TiO$_2$. The surfaces of these layers were modified using the corresponding benzoic acids from actonitrile solutions as already described in the previous chapter and a thin layer of *spiro*-OMeTAD applied via spin coating. An ohmic contact to *spiro*-OMeTAD was formed by final evaporation of a 20 nm thick gold layer (see Figure 7.5). Such modified heterojunction diodes were formed for all five benzoic acids and their current-voltage characteristics recorded. Figure 7.6 shows a set of typical current-voltage characteristics with and without correction for the series resistance of the devices. Analysis of the data revealed only minor differences in the series resistances remaining unaltered upon dipole modification.
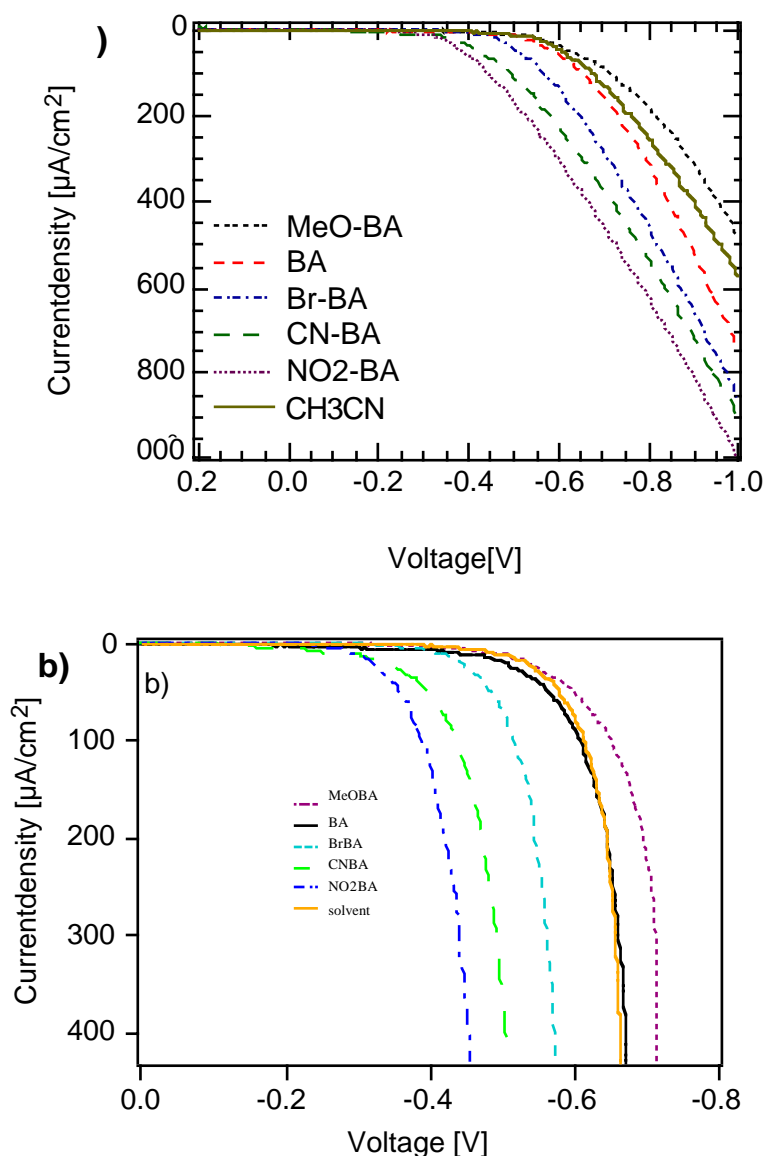
Figure 7.6 Current-voltage characteristics of TiO$_2$/*spiro*-OMeTAD heterojunctions, modified with a molecular, self-assembled layer. TiO$_2$ films were modified with methoxybenzoic acid (MeOBA), benzoic acid (BA), brombenzoic acid (BrBA), cyanobenzoic acid (CNBA) and nitrobenzoic acid (NO$_2$BA). Figure a) shows typical characteristics as measured, while Figure b) represents the same data, corrected for the series resistance of the devices.

However both graphs clearly show a significant effect of the surface modification on the diode characteristics. The more positive the observed workfunction shift was, the less rectifying the diodes proved to be. This seems reasonable as the workfunction difference between TiO$_2$ and *spiro*-OMeTAD becomes *smaller* when the workfunction of TiO$_2$ *increases*. In the following gedanken experiments the influence of the dipole layer on the built-in potential and band bending occuring at the heterojunction shall be rationalized.

7.4 Gedanken experiment
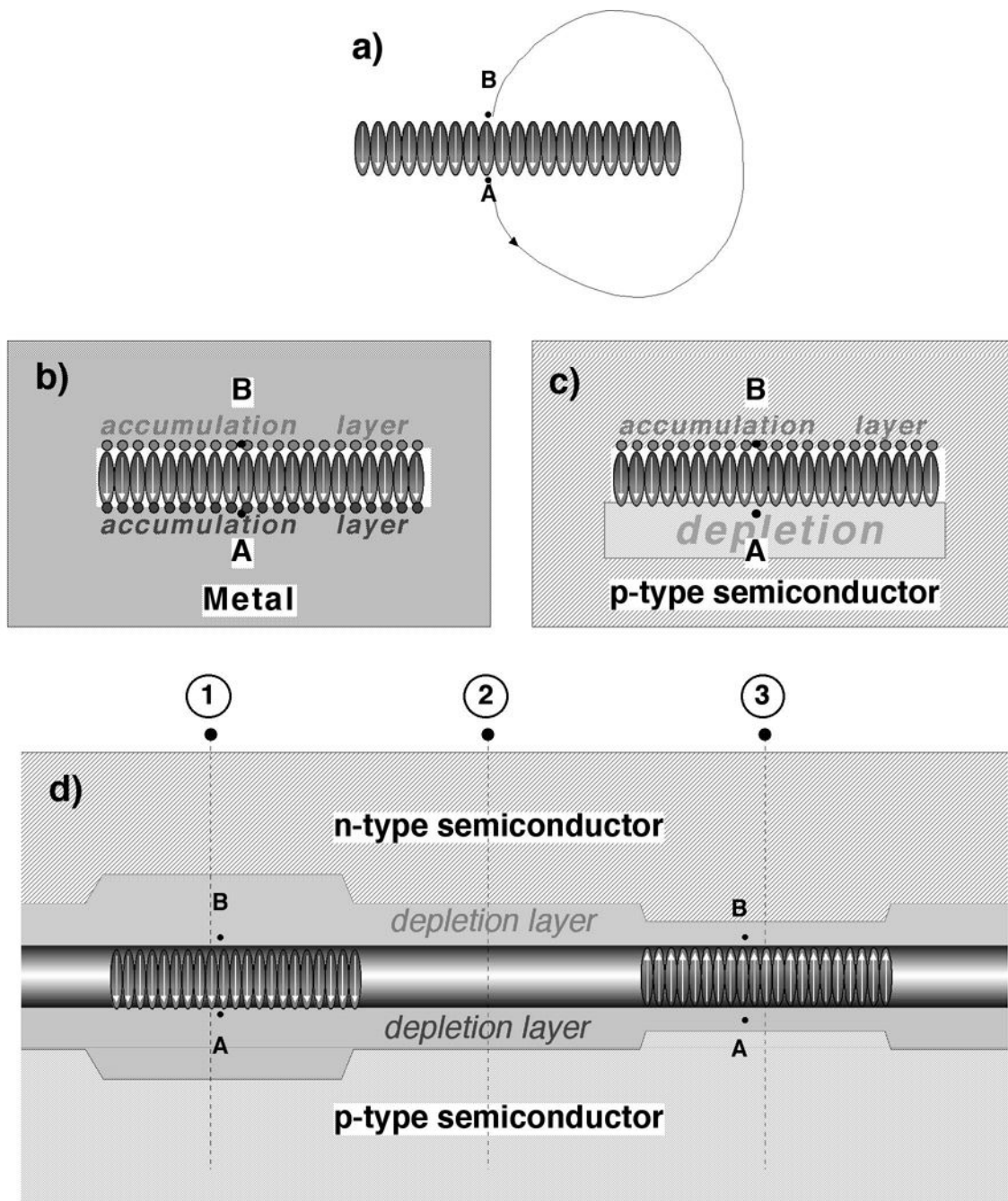
Figure 7.7 Gedanken experiment (see text).
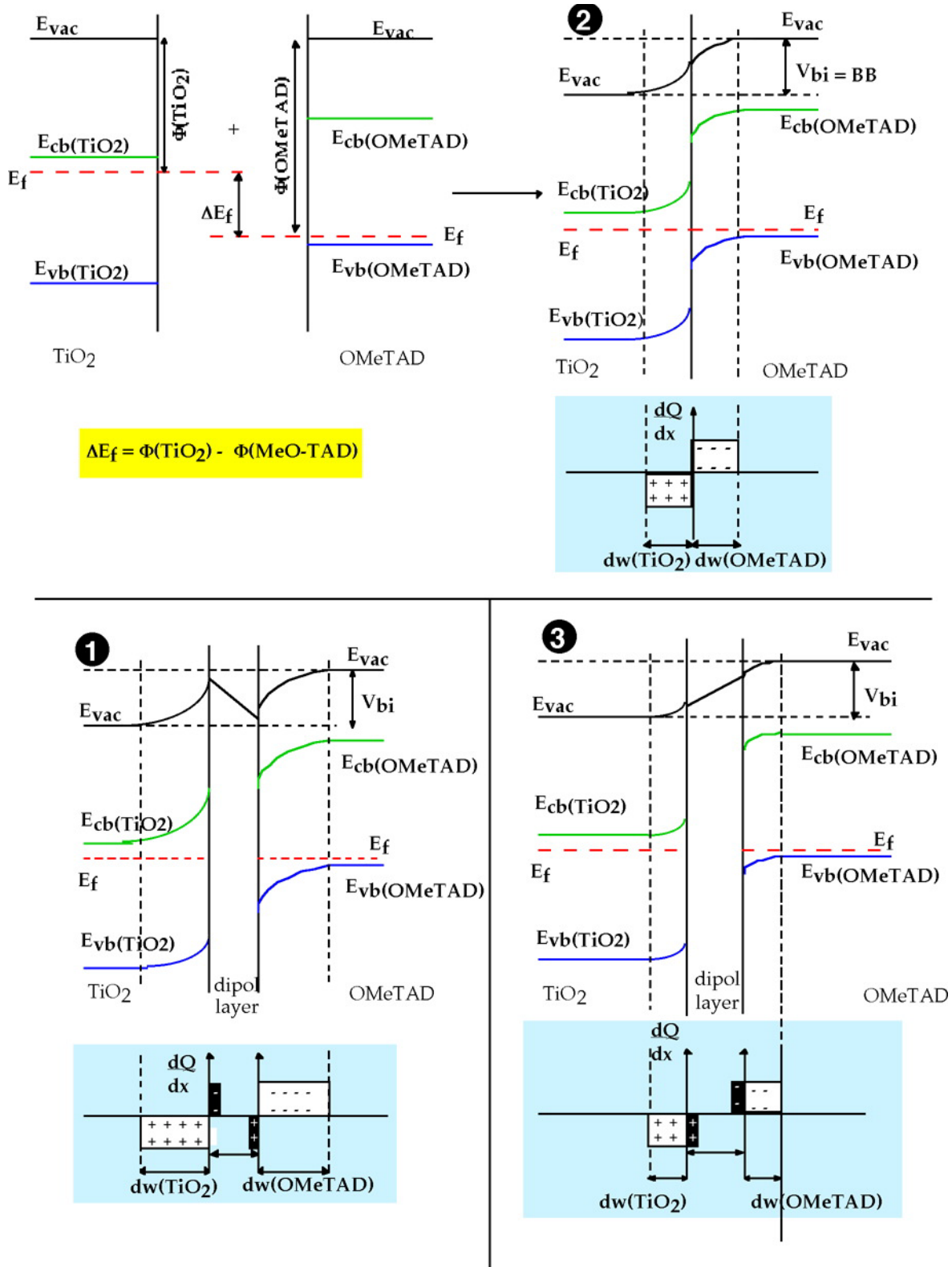
Figure 7.8 Scheme of the band diagrams of TiO$_2$/*spiro*-OMeTAD heterojunctions following the cross-sections 1, 2 and 3, shown in Figure 7.7.

Consider a dipole layer with finite dimensions placed in a *vacuum* (Figure 7.7a). The potential of an electron close to the positive side of the dipole layer (spot A) will be different to the potential of an electron in close vicinity to the negative side (spot B). The potential difference between point A and B will be identical to the potential drop inside the dipole layer. An electron traversing the dipole layer from A to B will experience the same change in potential as one going all the way around the finite dipole layer (path a). Hence an electric field exists outside the dipole layer. Due to the much longer distance, when taking path a) the electric field will be much weaker than inside the capacitor, but still present. Now imagine, that this finite capacitor is placed inside a *conductor* of infinite dimensions b). Due to the presence of mobile positive and negative charges the whole bulk of the conductor will be at exactly the same potential and no electric fields will exist outside the dipole layer. But still an electron traveling from A to B through the dipole field will experience the change in potential induced by the dipole field. To compensate this difference in potential at point A and B positive and negative charges will accumulate on each side of the capacitor, as shown in Figure 7.7. Due to the small screening length for charges inside the metal the thickness of the charge layers accumulating on either side of the dipole layer will be on the atomic scale.

Now consider the dipole layer being placed inside the infinite bulk of a *semiconductor* c). Again charge transfer from one side of the capacitor to the other will compensate for the potential difference, as similarly discussed in the previous case. Again no electric fields can exist inside the semiconductor bulk. However in case of the semiconductor a depletion layer will form on one side of the capacitor, as only one type of charge carriers is present. In case of a p-type semiconductor a charge accumulation layer will develop on the negative side of the capacitor, while a depletion layer will establishes on the positive side.

Finally let us treat a case where the finite dipole layer is placed at the infinite interface of a pn-heterojunction. Due to the workfunction differences of the two materials a depletion layer will establish at the interface. If now a dipole layer is

placed at the interface again charge will have to be transferred from one side of the capacitor to the other to compensate for the potential step, induced by the molecular dipole layer. As the negative side of the dipole layer faces the n-type material, charge transfer will further widen the depletion layer on both sides, while the introduction of an inversely polarized dipole layer will narrow the depletion width (see Figure 7.7).

Figures 7.8 show the band diagrams following the three different cross sections shown in Figure 7.7. The width of the depletion layer W is directly related to the total amount of band bending (BB) via the following equation[15]:

$$W = \sqrt{\frac{2\varepsilon_s}{q}\left(\frac{N_A + N_D}{N_A N_D}\right)BB}$$

(7.5)

$$
\begin{array}{lll}
N_A, N_D & = & \text{acceptor/donor impurity densities} \\
\varepsilon_s & = & \text{dielectric constant } (\varepsilon_{semiconductor}\,\varepsilon_0) \\
q & = & \text{elementary charge}
\end{array}
$$

Far away from the dipole layers (starting points of cross-sections 1, 2 and 3) the local vacuum level will be uninfluenced of any dipole field. Ionization energy, electron affinity and the relative position of the Fermi-level in respect to the bands will be that of the bulk material. This is true for the n-type as well as the p-type side of the junction. The transfer of charge induced by the dipole field will now alter the total amount of band bending (BB) observed at the junction by:

$$BB = V_{bi} - \Delta V$$

(7.6)

While V_{bi} represents the built-in field of the unmodified heterojunction (the workfunction difference of TiO_2 and *spiro*-OMeTAD) and ΔV the potential step induced by the dipole layer.

An amazing result of these model considerations, confirmed by our experimental results is that the current flow through this interface of two semiconductors can be dramatically improved by introducing an insulating layer at the interface of two semiconductors.

The presence of pinholes in these thin monolayers is very often considered as a problem, limiting the applicability of surface modification as a tool to control the electronic properties of a junction. The first point which rovides a good argument against this concern is that except for methoxybenzoic acid all the applied adsorbates improve current flow through the junction. Imperfections in the molecular monolayer which allow direct contact of TiO_2 and *spiro*-OMeTAD will therefore not act as 'pinhole' but in the worst case as a small spot on the surface which is less transparent for electron transfer than its surrounding. Furthermore the effect of the dipole can not simply be related to the way electrons pass through the dipolar molecules. This as an organic molecule will always enlarge the distance for interfacial electron transfer (introducing a certain barrier height) and as an increase in current flow – as observed- could never be explained by this model. The role of the dipole field is rather to influence the energetics of the entire junction by a decrease or increase of the total amount of band bending occurring at the junction. It can be expected that the dipole will always have an overall effect, whenever the diameter of the pinholes is significantly smaller than the depletion layer width. This assumption is illustrated in Figure 7.9. In this last gedanken experiment a pn-heterojunction is consider, which is modified with a molecular dipole layer showing imperfections. An external voltage is applied to the junction, which is just a bit smaller than the built-in field of the unmodified junction. Therefore the depletion layer will be very thin in unmodified areas of the junction. Areas which bear a perfect monolayer of dipole molecules will show a wide depletion layer, induced by the dipole layer. A thin pinhole as shown in case A will not result in a collapse of the depletion region at this point. The depletion layer will rather exhibit a small negative cusp above and below the pinhole. Once the pinhole is significantly wider than the depletion layer (case B) the later will actually break down and electron transfer is no more hindered by the presence of a depletion layer. In the case of a homogeneous 50 % coverage of the surface (C) a homogeneous depletion layer should form, whenever it is wider than the intermolecular distance of the molecular dipoles. These assumptions still have to be confirmed by experiments and/or theoretical calculations of the

electric fields. Following this theory a monolayer of weak dipoles, inducing a ΔCPD of 0.2 V (at 100 % coverage) should lead to the same experimental results as a 20% surface coverage with a strong dipole, showing a ΔCPD of 1.0 V (at 100 % coverage). This still has to be confirmed.
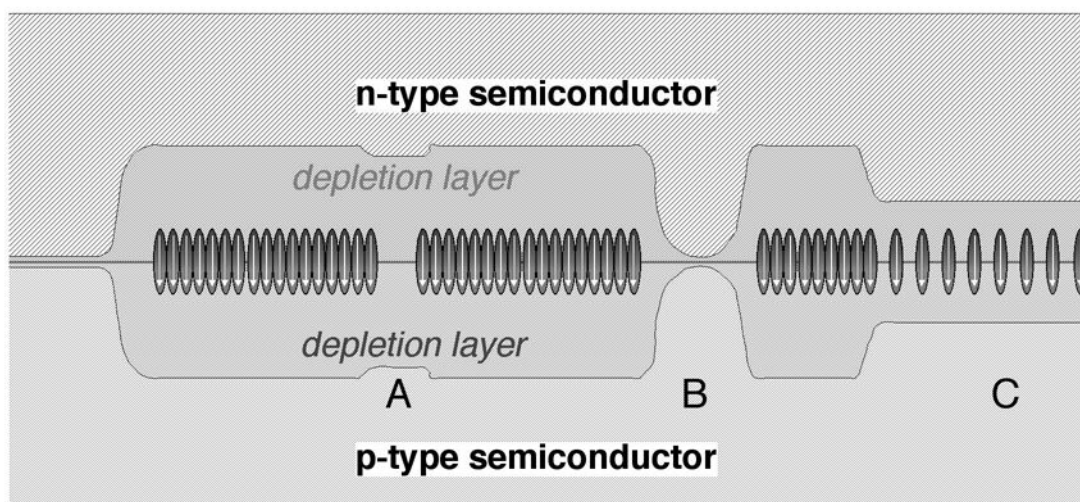
Figure 7.9 (see text).

When applying the above findings on the concept of dye-sensitized solar cells, it should be possible to improve their photovoltaic performance by controlling their interfacial dipole field. This can be realized either by choosing sensitizers with appropriate dipole properties or by co-adsorption of strongly dipolar substances. Assuming the quantum yield of photoinduced charge injection to be invariant towards the dipole field we would expect a suppression of the dark current and the recombination of photogenerated charge carriers. This would translate into an increase in open circuit voltage, short circuit current and fill factor. Experiments are currently under way to extend this concept to solid dye-sensitized solar cells.

References

1)   Nüesch, F.; Si-Ahmed, L.; Francois, B.; Zuppiroli, L. *Adv. Mater.* **1997**, *9*, 222.

2)   Campbell, I. H.; Kress, J. D.; Martin, R. L.; Smith, D. L.; Barashkov, N. N.; Ferraris, J. P. *Appl. Phys. Lett.* **1997**, *71*, 3528-3530.

3)   Gal, D.; Sone, E.; Cohen, R.; Hodes, G.; Libman, J.; Shanzer, A.; Schock, H.-W.; Cahen, D. *Proc. Indian Acad. Sci. (Chem. Sci.)* **1997**, *109*, 487-496.

4)   R. Hengerer, M. Grätzel; *unpublished results, manuscript in preparation* **2000**.

5)   Vittadini, A.; Selloni, A.; Rotzinger, F. P.; Grätzel, M. *J. Phys. Chem. B* **2000**.

6)   Bruening, M.; Moons, E.; Yaron-Marcovich, D.; Cahen, D.; Libman, J.; Shanzer, A. *J. Am. Chem. Soc.* **1994**, *116*, 2972-2977.

7)   Barbé, C. J.; Arendse, F.; Comte, P.; Jirousek, M.; Lenzmann, F.; Shklover, V.; Grätzel, M. *J. Am. Ceram. Soc.* **1997**, *80*, 3157.

8)   Besocke, K.; Berger, S. *Rev. Sci. Instrum.* **1976**, *47*, 840-842.

9)   Bastide, S.; Butruille, R.; Cahen, D.; Dutta, A.; Libman, J.; Shanzer, A.; Sun, L.; Vilan, A. *J. Phys. Chem. B* **1997**, *101*, 2678.

10) Cohen, R.; Bastide, S.; Cahen, D.; Libman, J.; Shanzer, A.; Rosenwaks, Y. *Adv. Mater.* **1997**, *9*, 746.

11) Si-Ahmed, L. *Synthèse et auto-assemblage de molécules fonctionalisées pour dérivatiser les électrodes des dispositifs électroluminescents organiques*; Ecole Polytechnique Fédéral de Lausanne: Lausanne, 1999.

12) Enright, B.; Redmond, G.; Fitzmaurice, D. *J. Phys. Chem.* **1994**, *98*, 6195.

13) Nüesch, F.; Rothberg, L. J.; Forsythe, E. W.; Le, Q. T.; Gao, Y. *Appl. Phys. Lett.* **1999**, *74*, 880-882.

14) Kavan, L.; O'Regan, B.; kay, A.; Grätzel, M. *J. Electroanal. Chem.* **1993**, *346*, 291-307.

15) Sze, S. M. *Physics of semiconductor devices*; John Wiley & Sons: New York, 1981.

Solid-state dye-sensitized mesoporous TiO2 solar cells showing high photon to electron conversion efficiencies

U. Bach*, D. Lupo†§, P. Comte*, J. E. Moser*, F. Weissörtel‡, J. Salbeck‡, H. Spreitzer† & M. Grätzel*¶

* Institute of Photonics and Interfaces, Swiss Federal Institute of Technology,
CH-1015 Lausanne, Switzerland

† Hoechst Research & Technology Deutschland GmbH & Co. KG,

Industriepark Höchst, D-65926 Frankfurt, Germany

‡ Max-Planck-Institut für Polymerforschung, D-55128 Mainz, Germany

§ Current address: Materials Science Laboratories, Sony International

(Europe) GmbH, Stuttgarter Str. 106, 70736 Fellbach, Germany

¶ To whom correspondence should be addressed

Solar cells based on dye-sensitized mesoporous films of TiO2 are low cost alternatives to conventional solid-state devices[1]. Impressive solar to electric conversion efficiencies have been achieved with such films when used in conjunction with liquid electrolytes[2]. Practical advantage may be gained by the replacement of the liquid electrolyte with a solid charge transport material. Inorganic p-type semiconductors[3,4] and organic materials[5-9] have been tested in this regard, but in all cases the incident monochromatic photon-to-electron conversion efficiency remained low. Here we describe a dye sensitized heterojunction of TiO2 with the amorphous organic hole transport material 2,2',7,7'-tetrakis-(N,N-di-p-methoxyphenyl-amine)9,9'-spirobifluorene[10, 11] (OMeTAD; refs. 10 and 11). Photoinduced charge carrier generation at the

heterojunction is very efficient. A solar cell based on OMeTAD converts photons to electric current with a strikingly high yield of 33 %.
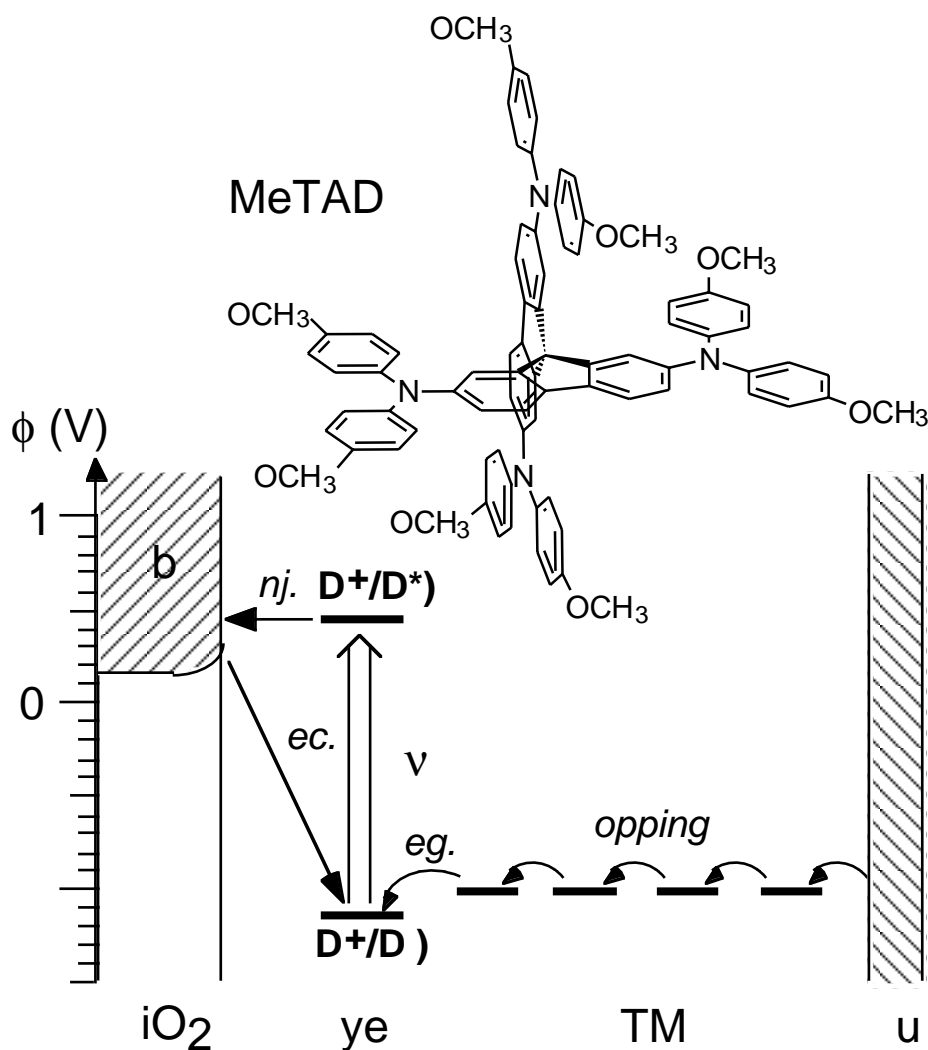
Figure 1 Scheme for the electron transfer processes (injection, regeneration, recapture, hopping) occurring in the dye sensitized heterojunction, as well as the approximate redox potentials and band energies of the different components.

The hole conductor contains a spiro-center (a tetrahedral carbon linking two aromatic moieties) which is introduced in order to improve the glass-forming properties and prevent crystallization of the organic material. Its glass transition temperature of $T_g = 120\,°C$, measured by differential scanning

calorimetry, is much higher then the one of the widely used hole conductor TPD (N,N'-diphenyl-N,N'-bis(3-methylphenyl)4,4'-diamine; $T_g = 62\ °C$). Crystallization is undesirable as it would impair the formation of a good contact between the mesoporous surface of the TiO_2 and the hole conductor. The methoxy groups are introduced in order to match the oxidation potential of the HTM to that of the sensitizer $Ru(II)L_2(SCN)_2$ (where L is 4,4'-dicarboxy-2,2'-bipyridyl), used in this study.
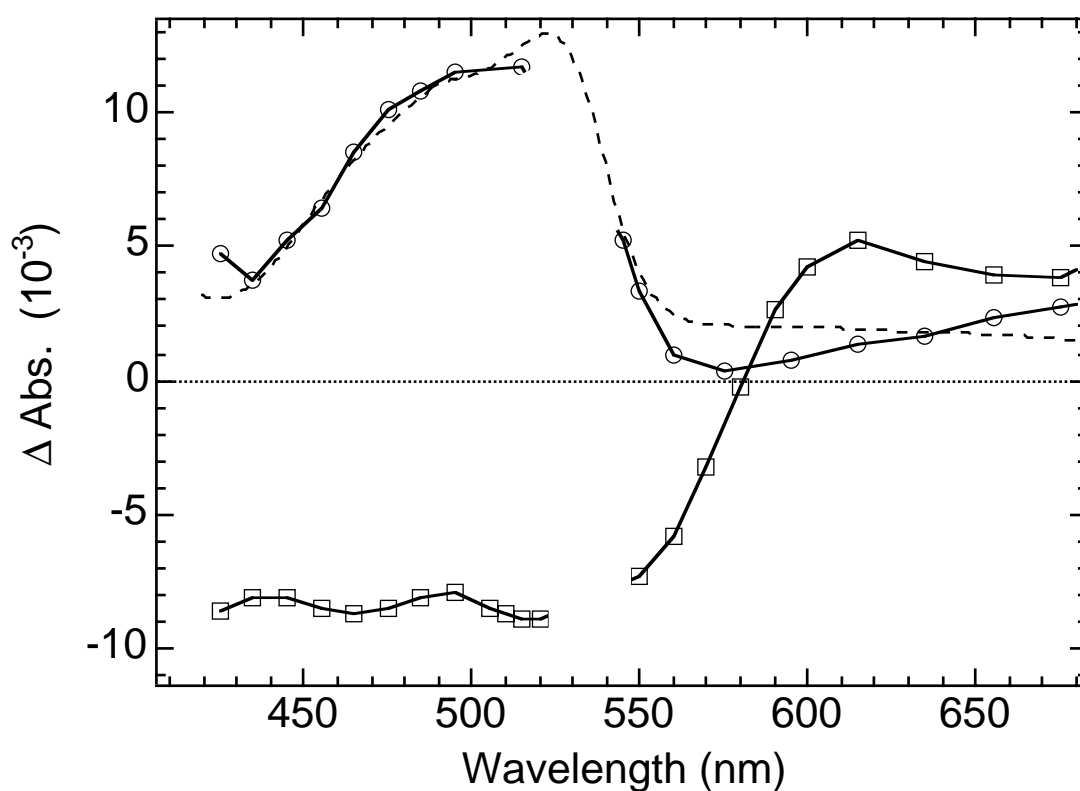
Figure 2 a) Transient absorption spectrum of a dye sensitized mesoporous TiO_2 film in the absence (squares) and in the presence (circles) of solid OMeTAD 50 ns after excitation at 532 nm. For comparison the absorption spectrum of chemically oxidized OMeTAD in chlorobenzene : acetonitrile = 90 : 10 is also displayed in the graph (dashed line, arbitrary units).

Figure 1 shows a scheme for the electron transfer processes occurring at the dye sensitized heterojunction. Visible light absorption by the sensitizer is followed by electron transfer to the conduction band of TiO_2. The dye is regenerated by hole injection into the HTM. The TiO_2 conduction band electrons as well as the holes in the HTM are subsequently transported by electronic

conduction to the contact electrodes. Pulsed nanosecond laser photolysis was used in conjunction with time resolved absorption spectroscopy to scrutinize the dynamics of the photoinduced charge separation process.

Figure 2 shows the transient absorption spectrum of a dye sensitized mesoporous TiO_2 film in the absence and presence of OMeTAD measured 50 ns after laser excitation. In the absence of OMeTAD, dye bleaching at around 500 nm is observed and a broad positive transient absorption appears above 570 nm due to the absorption of the oxidized dye $Ru(III)L_2(SCN)_2^+$ and of the TiO_2 conduction band electrons. Electron injection from the exited state of the dye into TiO_2 proceeds in the femtosecond domain[12], while the subsequent recapture of injected electrons by the oxidized dye takes several microseconds. In the presence of OMeTAD the bleaching signal disappears. Instead, the transient absorption rises vertically within the laser pulse. Comparison of the transient spectra obtained in the presence of OMeTAD with the absorption band of chemically oxidized OMeTAD confirms that the species giving rise to the new spectral feature is the radical cation $OMeTAD^+$. Apparently, electron injection from the excited sensitizer into TiO_2 is immediately followed by regeneration of the dye via hole transfer to OMeTAD, as shown below:

$$Ru(II)L_2(SCN)_2^* \longrightarrow Ru(III)L_2(SCN)_2^+ + e^- (TiO2) \quad (1)$$

$$OMeTAD + Ru(III)L_2(SCN)_2^+ \longrightarrow Ru(III)L_2(SCN)_2 + OMeTAD^+ \quad (2)$$

The process shown in equation (2) was too fast to be monitored with the laser equipment employed setting an upper limit of 40 ns for the hole transfer time.

A blank experiment was performed using mesoporous Al_2O_3 films instead of TiO_2 as a support for the $Ru(II)L_2(SCN)_2$ sensitizer, the results showed that hole transfer from the excited state of the dye to the OMeTAD does not contribute significantly to the photoinduced charge separation phenomena observed.

a)

b)
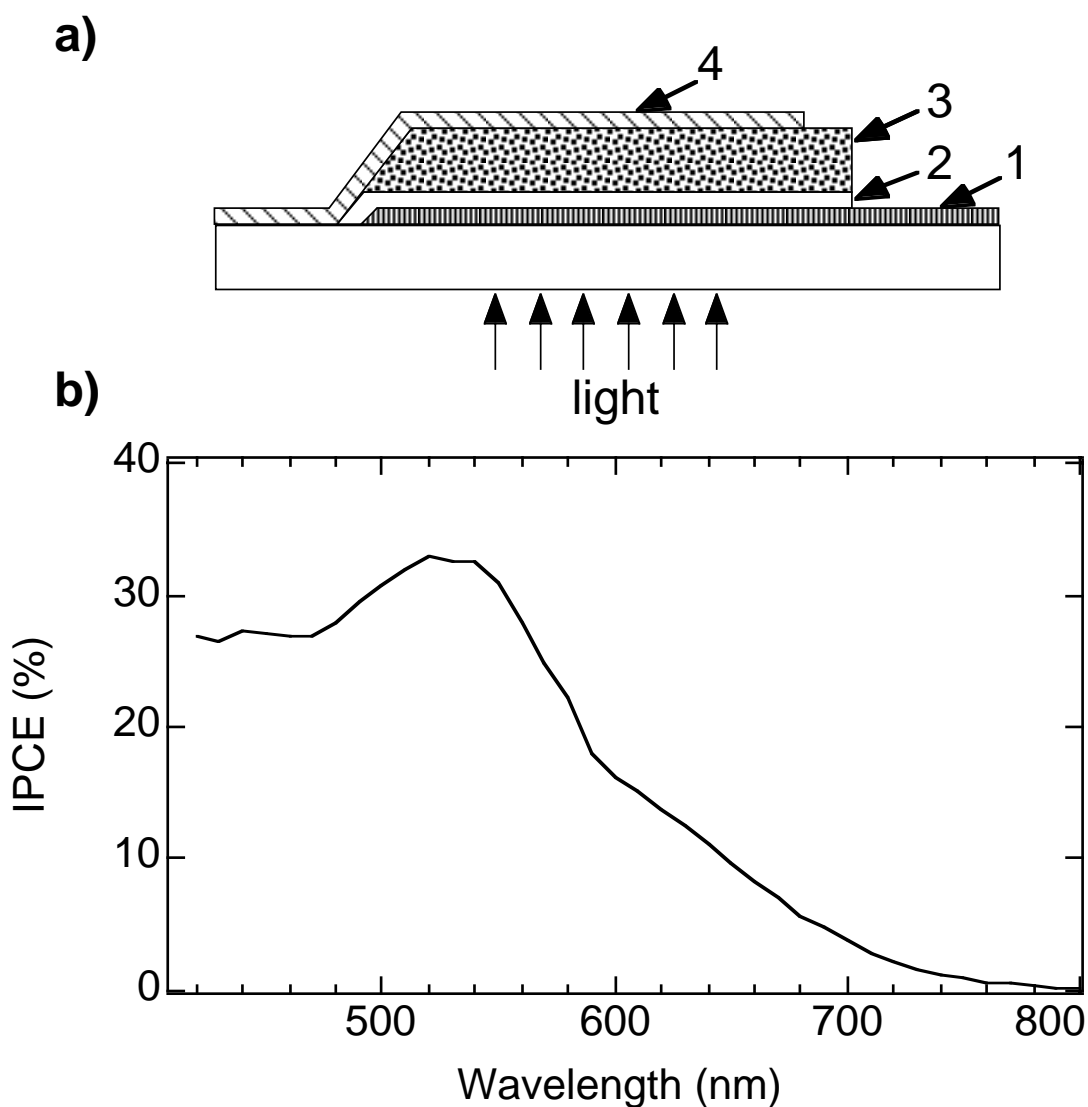
Figure 3 Structure and spectral response for the photovoltaic devices. a, Structure 1, conducting F-doped SnO_2 coated glass; 2, compact TiO_2 layer; 3, dye sensitized heterojunction; 4, gold electrode. b, Photocurrent action spectrum (IPCE) for a dye sensitized heterojunction, the structure of which is shown above. The IPCE value corresponds to the number of electrons generated by monochromatic light in the external circuit, divided y the number of incident photons. The 4 μm thick mesoporous TiO_2 film was sensitized with $Ru(II)L_2(SCN)_2$, spin-coated with a solution of 0.17 M OMeTAD, 3.3 mM $N(PhBr)_3SbCl_6$ and 15 mM $Li[(CF_3SO_2)_2N$ in chlorobenzene with 5 % acetonitrile added.

The photovoltaic performance of the dye-sensitized heterojunction was studied by means of sandwich type cells shown schematically in Figure. 3a. The working electrode consisted of conducting glass (F-doped SnO_2, sheet resistance 10 Ohm/square) onto which a compact TiO_2 layer was deposited by spray pyrolysis[13]. This avoids direct contact between the HTM layer and the SnO_2 which would short-circuit the cell. A 4.2 μm thick mesoporous film of TiO_2 was deposited by screen printing onto the compact layer[14] and derivatized with

$Ru(II)L_2(SCN)_2$ by adsorption from acetonitrile. The HTM was introduced into the mesopores by spincoating a solution of OMeTAD in chlorobenzene onto the TiO_2 film and subsequent evaporation of the solvent. A semi-transparent gold back contact was evaporated on top of the hole conductor under vacuum.
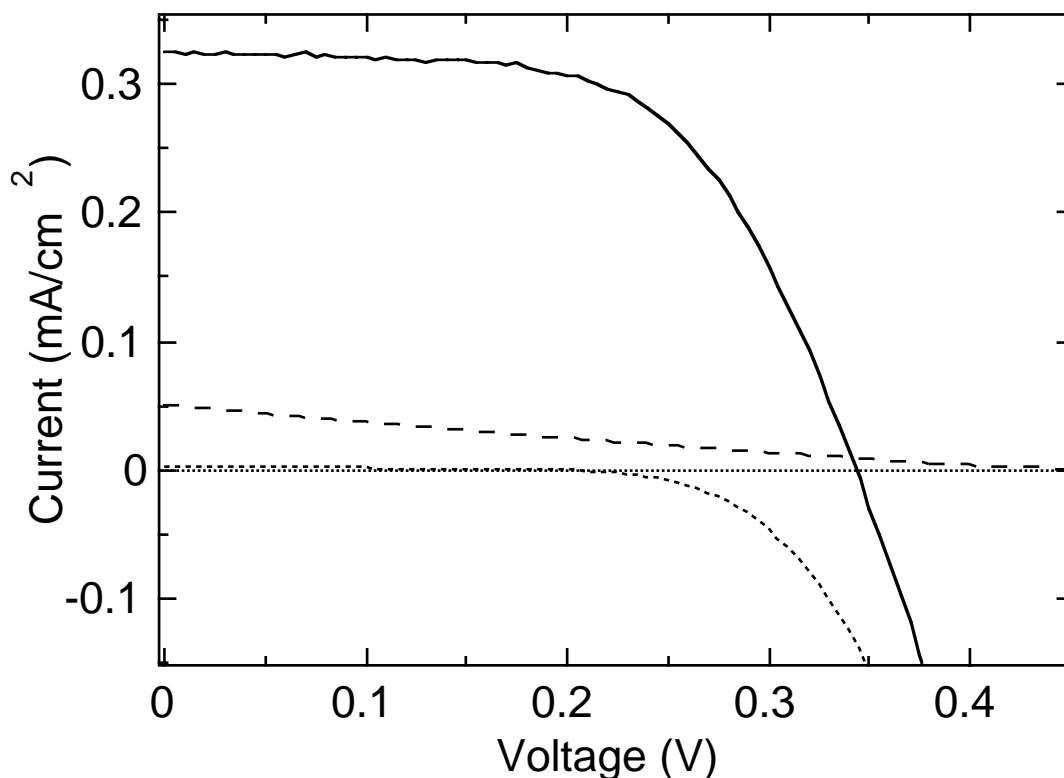
Figure 4 Current-density/voltage characteristics. Show are the characteristics of the same device as in Figure 3, obtained in the dark (I) and under white light illumination at 9.4 mW/cm^2 (II). The spectral distribution corresponded to global air mass 1.5 corrected for spectral mismatch. The short circuit current was 0.32 mA/cm^2, the open circuit voltage 342 mV and the fillfactor 62%, corresponding to an overall conversion efficiency of 0.74 %. For comparison the photocurrent-density/voltage characteristic of a cell containing no $N(PhBr)_3SbCl_6$ or $Li[(CF_3SO_2)_2N]$ is also shown (III).

Figure 3b shows the photocurrent action of a typical cell under short circuit conditions. The given values are not corrected for reflection and absorption losses of the conducting glass estimated to be at least 15% in the visible range of the spectrum. The spectrum closely matches the absorption spectrum of the dye, confirming that the observed photocurrent arises from electron injection by the sensitizer. The maximum value of the incident photon-to-electron conversion efficieny (IPCE) is 33%, which is more than two orders of magnitude larger then

the previously reported value for a similar dye sensitized solid heterojunction[9] and only a factor of about two lower that with liquid electrolytes[2].

The coating solution used for the device in Figure 3b contained 3.3 mM $N(PhBr)_3SbCl_6$ and 15 mM $Li[(CF_3SO_2)_2N$ in addition to 0.17 M OMeTAD. In the absence of these additives the maximum IPCE was only 5%. $N(PhBr)_3SbCl_6$ acts as a dopant, introducing free charge carriers in the HTM by oxidation, as confirmed by spectroelectrochemical measurements. Partial oxidation of OMeTAD by $N(PhBr)_3SbCl_6$ is a convenient way to control the dopant level[15]. Upon adding $N(PhBr)_3SbCl_6$ to a solution of OMeTAD in chlorobenzene, the radical cation $OMeTAD^+$ is instantly formed. The spectral features of $OMeTAD^+$ remained unchanged during solvent evaporation and glass formation, except for a small hypochromic shift. No subsequent absorption changes were detectable over weeks, confirming the temporal stability of $OMeTAD^+$ in the HTM.

The second additive $Li[(CF_3SO_2)_2N$ is a source of Li^+ ions, which are known to be potential determining for TiO_2 [16]. Along with the protons from the carboxylic acid groups of $Ru(II)L_2(SCN)_2$ they confer a positive charge to the surface of the oxide. As the sensitizer is negatively charged a local electrostatic field is produced, assisting electron injection into the TiO_2 while retarding recapture of the electron by the oxidized dye. The lithium salt may also compensate space charge effects. Under light illumination of the heterojunction regions a net positive space charge is expected to be formed in the HTM inducing a local field that impairs current flow. The lithium salt could screen this field eliminating the space charge control of the photocurrent. Improvement of the photovoltaic performance of dye sensitized heterojunctions by immersion in $LiClO_4$ solutions was also reported by Murakoshi et. al. [5].

Figure 4 shows current-density/voltage curves employing the device structure shown in Figure 3. Curves I and II were obtained with the hole conductor containing both the $N(PhBr)_3SbCl_6$ dopant and the $Li[(CF_3SO_2)_2N$ salt, whereas these additives were absent for curve III. Curve I was measured in the

dark, whereas curve II and III were obtained under light illumination. The device that contains the hole conductor without additives performs poorly, the conversion yield being only 0.04 % at a white light illumination of 9.4 mW/cm^2. Addition of the dopant and Li$^+$ salt increases the overall conversion efficiency to 0.74 %. Under full sunlight (100 mW/cm^2, air mass 1.5) short circuit photocurrents reached 3.18 mA/cm^2, a value which is unprecedented for solar cells based on organic solids. Further improvement of the photovoltaic performance is expected, as many parameters of the cell assembly have not yet been optimized. Preliminary stability tests performed over 80 h using the visible output of a 400W Xe lamp showed that the photocurrent was stable within ± 20 %, while the open-circuit voltage and the fill factor (see Methods) increased. The total charge passed through the cell during illumination was 300 Ccm-2; corresponding to turnover numbers of about 8,400 and 60 000 for the OMeTAD and the dye, respectively. This shows, that the hole conductor can sustain photovoltaic operation without significant degradation.

From the present findings the concept of dye sensitized heterojunctions emerges as a very interesting and viable option for future low cost state solar cells. Photodiodes based on interpenetrating polymer networks of poly(phenylenevinylene) derivatives[17,18] present a related approach. The main difference to our system is that at least one component of the polymer network needs to function simultaneously as an efficient light absorber and a good charge transport material. The dye sensitized heterojunction cell offers a greater flexibility, as the light absorber and charge transport material can be selected independently to obtain optimum solar energy harvesting and high photovoltaic output.

Methods

Compounds. OMeTAD was pure according to 1H-NMR and HPLC analysis. The synthesis will be reported elsewhere. Ru(II)L$_2$(SCN)$_2$ was prepared as previously described[2].

Transient absorption spectroscopy. This was carried out with a Nd-YAG laser as excitation light source, producing a 6 ns pulse at 532 nm of typically 1 mJ/cm^2, with a repetition frequency of 30 Hz. The probe light was provided by a Xe-lamp, which was spectrally narrowed by cutoff and interference filters before passing the device. A monochromator combined with a photomultiplier was used as detection system. A Tektronix 524 TDS oscilloscope was used to record and store the data. For the laser experiments dye sensitized mesoporous semiconductor films were deposited on ordinary glass.

Photocurrent-voltage characteristics. These were measured with a Keithley 2400 Source Meter and a 400 watt Xe-lamp. A Schott KG3 filter was used in order to approach the spectral distribution of the lamp to AM 1.5 G. The light intensity was regulated to the desired energy output by using a silicon solar cell, calibrated at the ISE-Fraunhofer Institut in Freiburg Germany. Efficiencies were corrected for the spectral mismatch. The fillfactor (FF) is defined as $FF = V_{opt}I_{opt}/I_{sc}V_{oc}$ where V_{opt} and I_{opt} are current and voltage for maximum power output and I_{sc} and U_{oc} the short circuit current and open circuit voltage.

References:

1. O'Regan, B. & Grätzel, M. A low-cost, high-efficiency solar cell based on dye-sensitized colloidal TiO$_2$ films *Nature* **353**, 737-739 (1991).

2. Nazeeruddin, M.K.*, et al.* Conversion of light to electricity by cis-X$_2$bis(2,2'-bipyridyl-4,4'-dicarboxylate)ruthenium(II) charge- transfer sensitizers (X = Cl-,Br-,I-,CN- and SCN-) on nanocrystalline TiO$_2$ electrodes *J. Am. Chem. Soc.* **115**, 6382-6390 (1993).

3. O'Regan, B. & Schwarz, D.T. Large Enhancement in Photocurrent Efficiency Caused by UV Illumination of the Dye-Sensitized Heterojunction TiO2/RuLL'NCS/CuSCN: Initiation and Potential Mechanism *Chem. Mat.* **10**, 1501-1509 (1998).

4. Tennakone, K., Kumara, G.R.R.A., Kumarasinghe, A.R., Wijayantha, K.G.U. & Sirimanne, P.M. Dye-sensitized nano-porous solid-state photovoltaic cell *Semicond. Sci. Technol.* **10**, 1689-1693 (1995).

5. Murakoshi, K., Kogure, R. & Yanagida, S. Solid State Dye-sensitized TiO$_2$ solar cell with polypyrrole as hole transport layer *Chemistry letters* **5**, 471-472 (1997).

6.   Bach, U*., et al.* Ultrafast hole injection from dye molecules into an organic hole conductor for dye sensitized solid state solar cells *Abstract Book, Bayreuth Polymer & Materials Research Symposium* , P28 (1997).

7.   Weissörtel, F. *Amorphe niedermolekulare Ladungstransportmaterialien für nanokristalline Solarzellen, Diplomarbeit* (Universität Regensburg, 1996).

8.   Grätzel, M. in *Future Generation Photovoltaic Technologies* (ed. McConnell) **404** 119-126 (A. I. P., Denver, 1997).

9.   Hagen, J*., et al.* Novel hybrid solar cells consisting of inorganic nanoparticles and an organic hole transport material *Synth. Met.* **89**, 215-220 (1997).

10.   Salbeck, J., Weissörtel, F. & Bauer, J. Spiro linked compounds for use as active materials in organic light emmiting diodes *Macromol. Symp.* **125**, 121-132 (1997).

11.   Salbeck, J., Yu, N., Bauer, J., Weissörtel, F. & Bestgen, H. Low molecular organic glasses for blue electroluminescence *Synth. Met.* **91**, 209-215 (1997).

12.   Tachibana, Y., Moser, J.E., Grätzel, M., Klug, D.R. & Durrant, J.R. Subpicosecond interfacial charge separation in dye-sensitized nanocrystalline titanium dioxide films *J. Phys. Chem.* **100**, 20056-20062 (1996).

13.   Kavan, L. & Grätzel, M. Highly efficient semiconducting TiO_2 photoelectrodes prepared by aerosol pyrolysis *Electrochim. Acta* **40**, 643-652 (1995).

14.   Barbé, C.J*., et al.* Nanocrystalline titanium oxide electrodes for photovoltaic applications *J. Am. Ceram. Soc.* **80**, 3157-3171 (1997).

15.   Abkowitz, M. &Pai D.M. Comparison of the drift mobility measured under transient and steady-state conditions in a prototypical hopping system *Phil. Mag. B* **53**, 193-216 (1986)

16.   Enright, B., Redmond, G. & Fitzmaurice, D. Spectroscopic determination of flat-band potentials for polycrystalline TiO_2 electrodes in mixed-solvent systems *J. Phys. Chem.* **97**, 1426-1430 (1994).

17.   Halls, J.J.M*., et al.* Efficient photodiodes from interpenetrating polymer networks *Nature* **376**, 498-500 (1995).

18.   Yu, G., Gao, J., Hummelen, J.C., Wudl, F. & Heeger, A.J. Polymer Photvoltaic cells: enhanced efficiencies via a network of internal donor acceptor heterojunctions *Science* **270**, 1789-1791 (1995).

Charge separation in solid-state dye-sensitized heterojunction solar cells

Udo Bach†, Yasuhiro Tachibana‡, Jacques-E. Moser†, Saif A. Haque‡, David

R. Klug‡, Michael Grätzel†* and James R. Durrant‡*

†‡

† *Institute of Photonic and Interfaces, Swiss Federal Institute of*

Technology, CH-1015 Lausanne, Switzerland

‡ *Center for Photomolecular Sciences, Departments of Biochemistry*

and Chemistry, Imperial College, London SW7 2AY, U.K.

* *Communicating authors*

Dye sensitized nanocrystalline solar cells are presently under intensive investigation as they offer an attractive alternative to conventional p-n junction devices[1,2]. Solid state versions have been described where the electrolyte present in the pores of the mesoporous oxide film is replaced by a large band gap p-type semiconductor[3-6]. In this way a solid state heterojunction of very large contact area is formed. Light is absorbed by the dye that is located at the interface. Upon excitation the dye injects electrons into the conduction band of the oxide and is regenerated by hole injection into the p-type conductor. High incident photon to electric current conversion efficiencies have been achieved recently with a cell consisting of a dye-derivatized mesoporous TiO_2 film contacted by a new organic hole conductor [7,8]. The great advantage of such systems with regards to conventional p-n junctions is that only majority carriers are involved in the photo-electric conversion process. Moreover, these are generated by the dye precisely at the site of the junction where the electric field is maximal, enhancing charge separation. Photo-electric conversion by conventional solar cells involves minority carriers whose lifetime is restricted due to recombination. As they are generated throughout the semiconductor and away from the junction, expensive

high purity materials are required in order to maintain the minority carrier diffusion length at a level where current losses are avoided.

While the dynamics of photoinduced redox processes in photoelectrochemical systems have been studied in great detail, little is known about the electron transfer dynamics in solid state sensitized junctions. Here we report for the first time on the direct observation of photoinduced, interfacial charge separation across a dye sensitized solid state heterojunction by means of picosecond transient absorption laser spectroscopy.
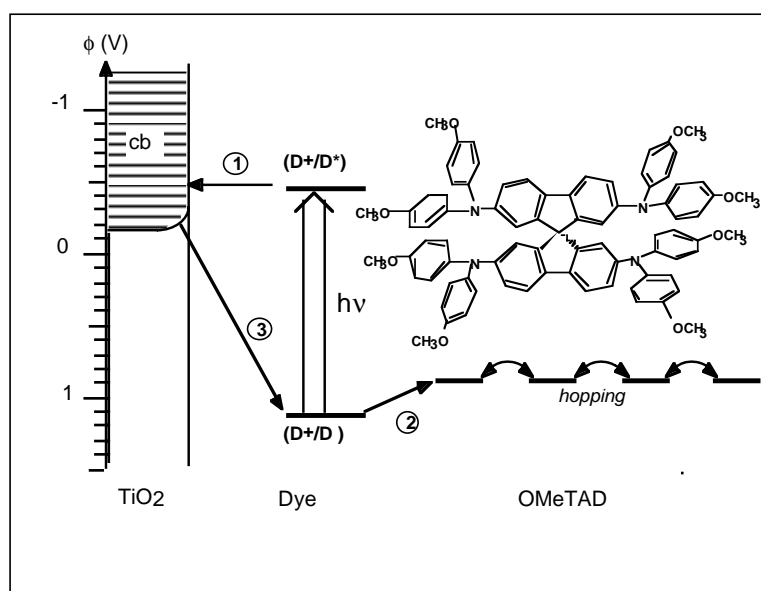
Figure 1: Scheme for the electron transfer processes occurring in the dye sensitized heterojunction together with the approximate redox potentials and band energies of the different components.

The charge transfer events taking place at the junction are depicted in Figure 1. Visible light is absorbed by the sensitizer, i.e. *cis*-$RuL_2(SCN)_2$ (where L is 4,4'-dicarboxy-2,2'-bipyridyl). Electron injection from the excited state of the dye into the conduction band of TiO_2 (1) is followed by subsequent hole transfer from the photooxidized dye to the organic holeconductor 2,2',7,7'-tetrakis(N,N-di-p-methoxyphenylamine)-9,9'-spirobifluorene or OMeTAD, regenerating the dye's original ground state (2).

$$RuL_2(SCN)_2{}^* \longrightarrow RuL_2(SCN)_2{}^+ + e^-(cb\ TiO_2) \quad (1)$$

$$RuL_2(SCN)_2{}^+ + OMeTAD \longrightarrow RuL_2(SCN)_2 + OMeTAD^+ \quad (2)$$
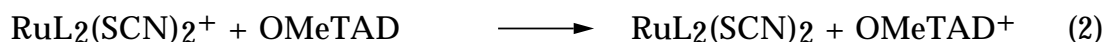
The latter process competes with recapture of the injected electron by the oxidized dye (3):

$$RuL_2(SCN)_2{}^+ + e^-(cb\ TiO_2) \longrightarrow RuL_2(SCN)_2 \quad (3)$$
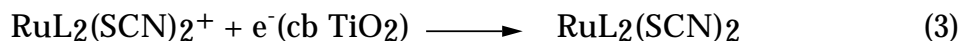
The double injection process described by equations (1) and (2) generates mobile majority carriers in both the TiO_2 and the hole conductor phases, which are subsequently collected at the contact electrodes.
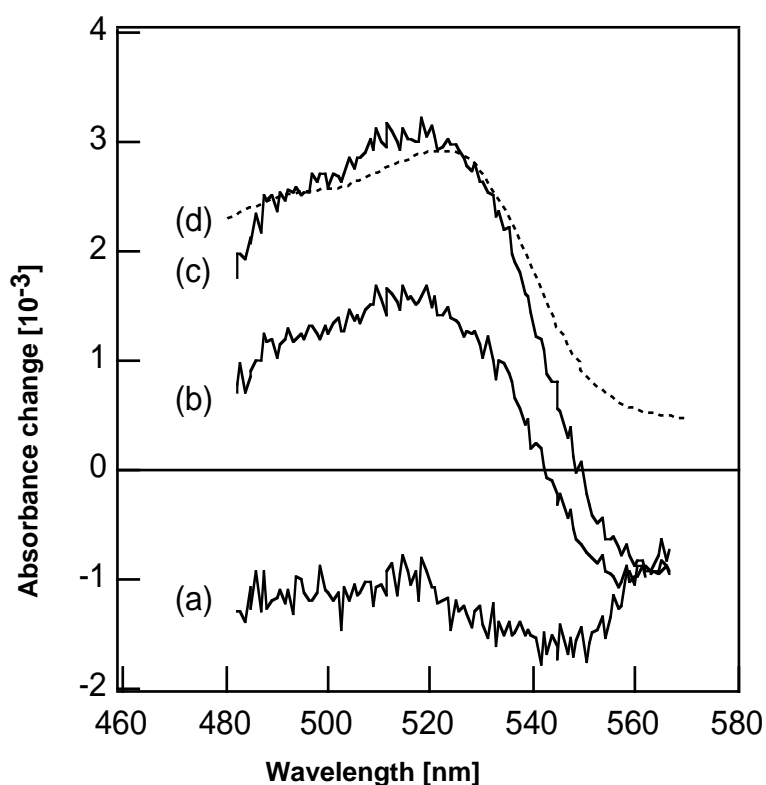
Figure 2: Transient absorption difference spectra obtained for solid TiO_2/OMeTAD heterojunctions, sensitized with $RuL_2(SCN)_2$, at different time delays to the exciting femtosecond pulse: (a) 3ps; (b) 300 ps; (c) 1000 ps. The excitation wavelength was 602±7 nm. For comparison, the absorption spectrum of chemically oxidized OMeTAD in chlorobenzene:acetonitrile = 90:10 (v/v) is also shown (d, arbitrary units).

Figure 2 shows the time evolution of the transient absorption spectra observed with such a *cis*-RuL$_2$(SCN)$_2$ sensitized heterojunction. At a time delay of 3 ps after laser excitation, a broad negative feature is observed between 480 and 570 nm. This can be assigned to the bleaching of the RuL$_2$(NCS)$_2$ ground state absorption due to excited state formation and electron injection into the TiO$_2$[9]. A positive feature with an absorption maximum at 520 nm grows in thereafter on the picosecond timescale. By comparison with the absorption spectrum of chemically oxidized OMeTAD (Figure 2, trace d) we can assign this transient to the formation of the OMeTAD$^+$ radical cation[7]. The spectral changes in Figure 2 are therefore due to electron injection from excited *cis*-RuL$_2$(SCN)$_2$ into TiO$_2$, reaction (1), followed by dye regeneration via hole transfer to OMeTAD, reaction (2). The first process is known to occur very rapidly with most of the reaction being completed within 1 picosecond [9-11]. Hence it is not resolved on the time scale employed in Figure 2. In view of the finding that the dynamics of photoinduced electron injection from *cis*-RuL$_2$(SCN)$_2$ into TiO$_2$ are insensitive to the nature of the contact medium of the dye [12], it can be assumed that a similar injection rate prevails for the TiO$_2$/OMeTAD heterojunction.
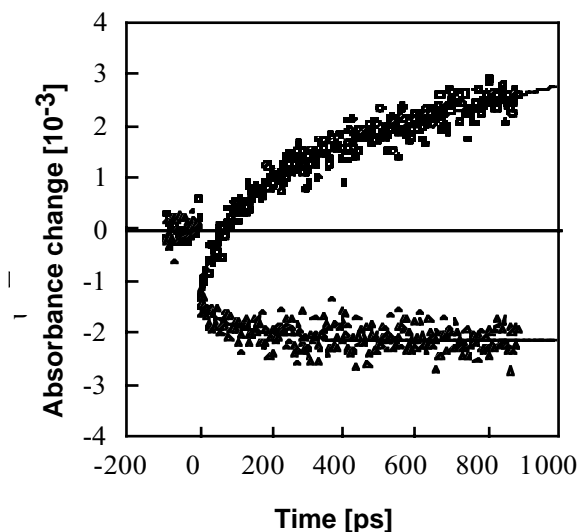
Figure 3: Transient absorption kinetics obtained for dye sensitized TiO$_2$ films covered with OMeTAD (circles) and with PC/EC (triangles) at a probe wavelength of 520 nm after excitation at 602 nm. The solid lines show results of exponential fitting to the data. For the sensitized TiO$_2$/OMeTAD heterojunction a double exponential fit yielded component lifetimes of 100 and 2300 ps.

Figure 3 compares the transient absorption kinetics of the 520 nm absorption for the *cis*-RuL$_2$(SCN)$_2$ sensitized mesoporous TiO$_2$ films in the presence and absence of the OMeTAD hole conductor. In the absence of OMeTAD, only the expected bleaching of the *cis*-RuL$_2$(SCN)$_2$ ground state absorption is observed due to electron injection into the TiO$_2$ conduction band. The small increase in this signal at early times is attributed to residual slow (10-100 ps) phases of the electron injection process into the TiO$_2$. In the presence of OMeTAD, the initially negative bleaching signal is replaced at later times by the positive OMeTAD$^+$ cation radical absorption due to hole injection from the oxidized sensitizer into the hole conductor. The hole injection kinetics observed in the presence of OMeTAD could be approximately fitted by a biexponential time law with component lifetimes of 100 and 2300 ps. We further note that the spectrum observed at 3 ps in Figure 2 suggests the formation of some (5-10 %) OMeTAD$^+$ cations even at this early time. We thus conclude that the hole injection from the RuL$_2$(SCN)$_2$$^+$ cation to the OMeTAD proceeds with a broad range of time constants from < 3 ps to > 1ns.

The multiple phases of the injection process may originate from the heterogeneous nature of the oxide/dye/OMeTAD heterojunction. In particular this may arise from incomplete filling of the mesoporous TiO$_2$ structure with the organic semiconductor. This would give rise to dye molecules with differing degrees of contact with the OMeTAD. In support of this possibility, we note that SEM studies on cross-sections recently revealed that porefilling is indeed incomplete when OMeTAD is applied via the spincoating technique (data not shown). We further note that for dye molecules not in contact with the OMeTAD, regeneration of the dye ground state may proceed via lateral hole migration between neighboring dye molecules until a dye molecule in close contact with the OMeTAD is reached. Such lateral charge transport has recently been observed in monolayers of surface adsorbed molecules on nanoporous TiO$_2$ such as aromatic amines[13] and ruthenium polypyridyl complexes[14]. Lateral hole hopping prior to dye regeneration by the hole conductor might therefore

contribute to the dye regeneration kinetics and could be the underlying mechanism for its slower components.

From consideration of the relative amplitudes of the traces shown in Figure 3, we can estimate the quantum yield of hole injection into OMeTAD. Assuming a difference in molar extinction coefficients of - 12000 l mol^{-1} cm^{-1} for $[\varepsilon_{520}(\text{dye}^+)-\varepsilon_{520}(\text{dye}^0)]$[15] and of 37000 l mol^{-1} cm^{-1} for $\varepsilon_{520}(\text{OMeTAD}^+)$[16] we conclude, that 900 ps after laser excitation the hole injection yield is about 50%. The presence of some residual dye cation states at this time is further supported by the small 560 nm negative feature observed in Figure 2, attributed to a residual bleaching signal of the $\text{RuL}_2(\text{SCN})_2$ dye cation. Extrapolation of the fit to the kinetics shown in Figure 3 suggests that at long times (~ 10 ns), the efficiency of hole transfer approaches unity. Such a high yield of charge separation is consistent with the rapid rate of hole transfer from the $\text{RuL}_2(\text{SCN})_2{}^+$ to the OMeTAD reported here. The competing recombination reaction (3) typically proceeds on the micro to millisecond time scale[17-19] and is therefore likely to be much slower than the hole injection reaction (2) studied here.

In conclusion, it was possible to directly observe the sequence of dye sensitized electron injection into TiO_2 and subsequent hole transfer from the dye to a solid organic charge transport material, resulting in regeneration of the dye ground state. The dye regeneration could be time resolved and shown to proceed primarily on the picosecond time scale with multiphasic kinetics. It is therefore at least one order of magnitude faster than the dye regeneration process involving iodine/iodide electrolytes[2,19]. The high rate of the hole injection reaction into the OMeTAD ensures that the quantum efficiency for the overall charge separation process across the junction is close to unity. This may be a key factor behind the high external quantum efficiencies for charge carrier collection obtained with OMeTAD compared to other solid state hole conducting materials studied to date[7].

References

1)   O'Regan, B.; Grätzel, M. *Nature* **1991**, *353*, 737-739.

2)   Nazeeruddin, M. K.; Kay, A.; Rodicio, I.; Humphry-Baker, R.; Müller, E.; Liska, P.; Vlachopoulos, N.; Grätzel, M. *J. Am. Chem. Soc.* **1993**, *115*, 6382-6390.

3)   O'Regan, B.; Schwartz, D. T. *Chem. Mater.* **1998**, *10*, 1501-1509.

4)   Tennakone, K.; Kumara, G. R. R. A.; Kumarasinghe, A. R.; Wijayantha, K. G. U.; Sirimanne, P. M. *Semicond. Sci. Technol.* **1995**, *10*, 1689-1693.

5)   Murakoshi, K.; Kogure, R.; Yanagida, S. *Chem. Lett.* **1997**, *5*, 471-472.

6)   Bach, U.; Weissörtel, F.; Uebe, J.; Grätzel, M.; Lupo, D. W.; Salbeck, J. *Abstract Book, Bayreuth Polymer & Materials Research Symposium* **1997**, P28.

7)   Bach, U.; Lupo, D.; Compte, P.; Moser, J. E.; Weissörtel, F.; Salbeck, J.; Spreitzer, H.; Grätzel, M. *Nature* **1998**, *395*, 583-585.

8)   Sinke, W. C.; Wienk, M. M. *Nature* **1998**, *395*, 544-545.

9)   Tachibana, Y.; Moser, J. E.; Grätzel, M.; Klug, D. R.; Durrant, J. R. *J. Phys. Chem.* **1996**, *100*, 20056-20062.

10)   Hannappel, T.; Burfeindt, B.; Storck, W.; Wilig, F. *J. Phys. Chem B.* **1997**, *101*, 6799-6802.

11)   Asbury, J. B.; Ellingson, R. J.; Gosh, H. N.; Ferrere, S.; Notzig, A. J.; Lian, T. *J. Phys. Chem. B* **1999**, *103,* 3110-3119.

12)   Durrant, J. R.; Tachibana, Y.; Mercer, I.; Moser, J. E.; Grätzel, M.; Klug, D. R. *Zeit. Phys. Chem.* **1999**, *in press*

13)Bonhôte, P.; Gogniat, E.; Tingry, S.; Barbé, C.; Vlachopoulos, N.; Lenzmann, F.; Comte, P.; Grätzel, M. *J. Phys. Chem. B* **1998**, *102*, 1498-1507.

14)Heimer, T. A.; D'Arcangelis, S. T.; Farzad, F.; Stipkala, J. M.; Meyer, G. J. *Inorg. Chem.* **1996**, *35*, 5319-5324.

15) estimated from earlier measurements, correlating injection efficiency data and transient absorption data

16)   Weissörtel, F. Amorphe niedermolekulare Ladungstransportmaterialien für nanokristalline Solarzellen, Diplomarbeit; Universität Regensburg:, 1996.

17)   Hagfeldt, A.; Grätzel, M. Chem. Rev. **1995**, 95, 49-68.

18)   O'Regan, B.; Moser, J.; Anderson, M.; Grätzel, M. J. Phys. Chem. **1990**, 94, 8720.

19)   Haque, S. A.; Tachibana, Y.; Klug, D. R.; Durrant, J. R. J. Phys. Chem. B **1998**, 102, 1745-1749.

Supporting information

Compounds. Transparent, mesoporous TiO_2 films of about 3 μm thickness on ordinary glass and the dye $RuL_2(SCN)_2$ were prepared as previously described[2]. OMeTAD was used as received from Aventis AG/Frankfurt-Germany and was pure according to ^{1}H-NMR and HPLC analysis.

Samples. Dye adsorption was carried out from 5×10^{-4} M solutions in acetonitrile for about 1 hour. The film was then dried in air and spincoated with a solution of 300 mg OMeTAD per ml of chlorobenzene (puriss. p.a.). The samples were dried in vacuum prior to laser experiments.

Ultrafast transient absorption spectroscopy. The ultrafast transient absorption spectrometer employing the femtosecond Ti:sapphire chirped pulse amplifier laser system has been described in detail elsewhere. The excitation pulse with an intensity of 48±5nJ (600±60μJ/cm2) was tuned at 602±7 nm with the optical parametric amplifier (OPA) system. Absorbance at this excitation wavelength is 0.05-0.2 for all samples used. Transient absorption data were collected over 0-1 ns with a time delay of 3.3 ps between points and a probe wavelength of 480-570 nm, using a multichannel detector. All experiments were carried out with the magic angle configuration (54.7°) between pump and probe pulses with a repetition rate of 1 KHz at 20 °C. The instrument response of the spectrometer was 150-250 fs. All transients are presented normalized with the number of photons adsorbed by the sensitizer dyes for each sample.

Characterization of hole transport in a new class of spiro-linked oligotriphenylamine compounds

Udo Bach*, Kenny DeCloedt, Hubert Spreitzer and Michael Grätzel

Udo Bach, Kenny DeCloedt, Prof. Michael Grätzel
Institute of Photonic and Interfaces
Swiss Federal Institute of Technology
Lausanne 1015 (Switzerland)

Dr. Hubert Spreitzer
Covion Organic Semiconductors GmbH
Industrial Park Höchst
Frankfurt am Main 65926 (Germany)

The development of new charge transport materials (CTMs) for the application in organic light emitting diodes (OLEDs)[1, 2] organic solar cells[3-6] or organic transistors[7-9] has become a major research focus in material science. High current densities at low driving voltages and excellent stability are two of the key requirements that CTMs have to fulfill to find application in new electronic components. In order to meet these requirements materials have to be developed, which form thermally stable amorphous states, showing high carrier mobilities and matching the redox levels of the other device components. Molecular CTMs proved to be superior to charge transport polymers such as PPV with regards to carrier mobilities, however they often suffer from poor thermal stability. Different synthetic approaches have been pursued, to confer a higher stability of the glassy state to the chemical structure of low molecular weight compounds[10-13]. Salbeck and co-workers introduced the concept of linking two arylamine moieties via a *spiro*-center, introducing a 90° angle between them[14, 15]. This enhances the thermal stability of its amorphous state, the glass transition temperature augmenting significantly (see Table 1). Compounds based on this

spiro-linkage have meanwhile found applications in solar cells[3] and OLEDs[14, 15], however the influence of the *spiro*-center on the hole mobility has so far never been elucidated. In this communication we present a detailed study of charge transport in vapor-deposited glasses of two different *spiro*-compounds via the time-of-flight technique (TOF) and compare these results to non-*spiro* analogues, which were studied earlier in literature.

substance	Tg	substance	Tg
m-TTB	66 °C[22]	*spiro-m*-TTB	119 °C[23]
TAD	70 °C[12]	*spiro*-TAD	133 °C[23]

Table 1. Glass transition temperatures for spiro-*m*-TTB, spiro-TAD and their non-*spiro*-connected homologues determined by differential scanning calorimetry.

Films of 2,2',7,7'-tetrakis-(N,N-diphenylamine)-9,9'-spirobifluorene (*spiro*-TAD) and 2,2',7,7'-tetrakis-(N,N-di-*m*-methylphenyl-amine)9,9'-spirobifluorene (*spiro-m*-TTB) (see Figure 1) were prepared by vacuum vapor deposition onto a fluorine-doped SnO_2 conducting glass substrate and a back contact was formed by thermal evaporation of 40 nm gold on top of the organic layer. Prior to the evaporation of the CTM the SnO_2 electrode was modified with a thin film (50 –100 nm) of TiO_2 via spray-pyrolysis[16]. The TiO_2 film was introduced as charge generating layer, forming electron/hole pairs upon excitation with UV light which dissociate in the electric field at the junction with the organic CTM. Light adsorbed by the CTM creates excitons, which will also give rise to free positive charge carriers, when the excitons dissociate at the built-in field region. Both mechanisms are likely to contribute to the initial formation of charge carriers.

Fig. 1. Chemical structures of the two *spiro*-CTM molecules studied and their non-*spiro* connected homologues.

The mobilities were measured by conventional time-of-flight techniques that have been described in detail elsewhere[17] (see also experimental). The samples were connected to an external voltage source, applying a positive bias to the SnO_2 electrode. A thin slab of positive charge carriers was formed by excitation with a short laser pulse through the SnO_2-electrode (354 nm/ 6 ns). The holes migrate under the influence of the external electric field towards the back contact, giving rise to a displacement current, which can be measured in the external electric circuit. In case of non-dispersive transport the current is constant, as long as the thin sheet of holes traverses the bulk of the sample. It will fall to zero, once the charge carriers arrive at the back contact. This time is generally called the transient time.
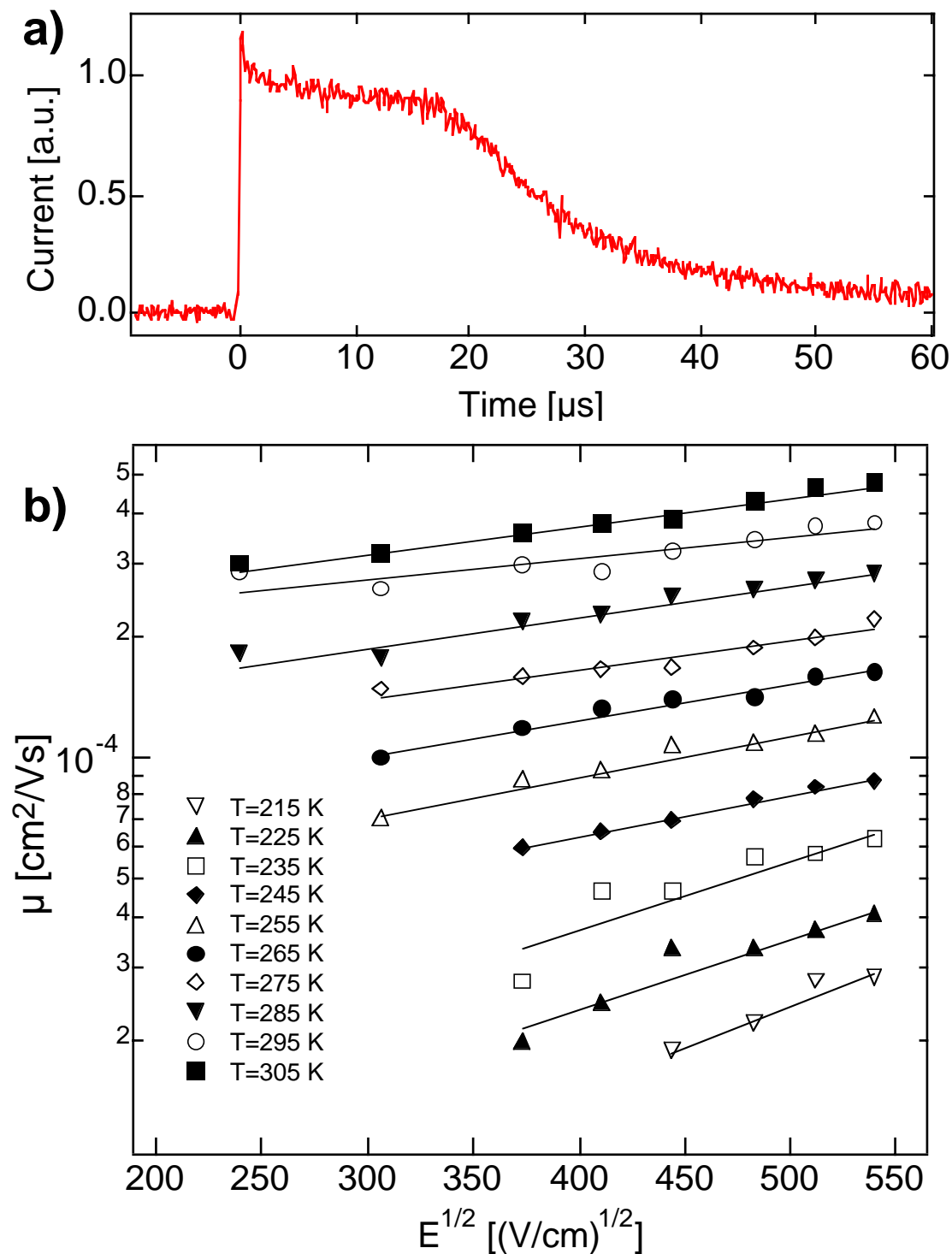
141

Fig. 2. a) A typical photocurrent transient for *spiro-m*-TTB. The temperature was 245 K, The applied electric field 2.3 10^5 V/cm, the thickness of the organic layer 3.3 μm, b) Field dependencies of the mobility at different temperatures for *spiro-m*-TTB.

Figure 2a shows a typical photocurrent transient for a sample of *spiro*-TAD. The transient current exhibits a pronounced plateau followed by a longer tail. The transient times can be determined from the intersection of asymptotes to the plateau and the trailing edge of the transients, in a linear current versus time representation. The moblility μ can be derived from the simple relation $\mu = d/\tau_t$

E, where d is the film thickness, τ_t is the transient time and E the strength of the externally applied field.

Figure 2b shows the temperature and field dependent hole mobility of spiro-*m*-TTB. Nondispersive transients were observed over a wide range of fields and temperatures. The mobility of *spiro-m*-TTB for a given temperature depends linearly on the square root of the electric field strength when plotted in semilogarithmic fashion indicating that the Pool-Frenkel law $\mu \propto \exp[\beta E^{1/2}]$ applies. The mobility increases with temperature, while the factor β decreases at higher temperatures. These findings are in agreement with the predictions of the disorder formalism proposed by Bässler *et.al.* [18], which postulates that charge transport occurs via random walk hopping through a manifold of localized states. The Bässler model considers energetic and positional disorder separately. The first arises from energetic fluctuations of electronic states, assumed to follow a Gaussian distribution, while the second is due to variations in the distance or orientation of adjacent hopping sites. The expression derived is:

$$\mu(\sigma, \Sigma, E) = \mu_0 \cdot \exp\left[-\left(\frac{2\sigma}{3kT}\right)^2\right] \cdot \exp\left[C \cdot \left(\left(\frac{\sigma}{kT}\right)^2 - \Sigma^2\right) \cdot \sqrt{E}\right] \tag{1}$$

with

> μ_0 = prefactor mobility
> σ = energetic disorder
> Σ = degree of positional disorder
> C = empirical constant of $2.9 \; 10^{-4} \; (cm/V)^{1/2}$
> E = applied electric field

The temperature and field dependence of the mobility was analyzed according to this model. The temperature dependence of the zero-field mobility was used to derive values for the prefactor mobility μ_0 and the energetic disorder σ. Values for the zero-field mobilities at different temperatures were derived by extrapolation of the data shown in Figure 2b to zero field. Values for the positional disorder were obtained from the temperature dependence of the slope of the field dependence β.

substance	μ_0 [cm^2/Vs]	σ [eV]	Σ	Ref.
*spiro-m-*TTB	0.010	0.08	1.2	-
spiro-TAD	0.016	0.08	2.3	-
m-TTB	0.019	0.069	1.5	[24]

Table 2. hole transport parameters[21]

Table 2 lists the hole transport parameters for *spiro-m*-TTB and compares them to literature values for its homologue *m*-TTB (see Figure 1) containing no *spiro*-center. The spiro-linkage reduces the prefactor mobility μ_0 by a factor of 1.9 while having little effect on the energetic disorder parameter σ. The positional disorder Σ decreases slightly upon introduction of the *spiro*-center, suggesting that the *spiro*-linkage to some extend improved the morphologic properties of the amorphous state.

The temperature and field dependence shows the same basic features as for *spiro-m*-TTB. Analysis of the data shown in Figure 3b according to the Bässler formalism (eq. 1) yields the charge transport parameters given in Table 2. The prefactor mobility μ_0 and positional disorder are higher for *spiro*-TAD compared with *spiro-m*-TTB. At low electric fields *spiro*-TAD therefore exhibits higher mobility then *spiro-m*-TTB, while at higher fields ($\sqrt{E} > 400 \, \text{V}^{0.5}/\text{cm}^{0.5}$) the influence of the positional disorder overcomes that of μ_0, making charge transport slightly more favorable in *spiro-m*-TTB, compared to *spiro*-TAD.

Fig. 3. a) A typical photocurrent transient for *spiro*-TAD. The temperature was 245 K, The applied electric field was 2.3 10^5 V/cm and the thickness of the organic layer 3.3 μm, b) Field dependency of the mobility at different temperatures for spiro-TAD.

Figure 3 shows the corresponding TOF data for spiro-TAD. Similar to the data presented for *spiro-m*-TTB the transient photocurrent exhibits a pronounced

plateau, which is followed by a longer tail indicating non-dispersive transport in *spiro*-TAD.

The introduction of methyl-groups in meta position to the nitrogen substantially decreases the thermal stability of the compound while it has minor effects on its charge transport properties. Still the differences observed for the charge transport parameters of the three substances, shown in Table 2 are not very pronounced.

We conclude, that the introduction of a *spiro*-center between 2 CTM moieties strongly improves the thermal stability of the amorphous state, without significantly changing their charge transport properties. The observed decrease in the hole mobility is of the same magnitude as that arising from changes in film morphology due to variation of the evaporation conditions or the presence of trace impurities [19]. Conferring higher thermal stability of the amorphous state by modification of the chemical structure of the CTM is superior to the classical approach where the amorphous state is stabilized by blending the CTM into a polymer matrix, e.g. polycarbonate. This is generally accompanied by a mobility drop of more then one order of magnitude[20]. In contrast, *spiro*-substituted CTMs combine the high morphologic stability commonly only observed in polymeric systems with the high charge mobility that is proper to low-molecular weight CTM's. They open a new synthetic route to stable, electronically active materials with improved properties for the design of highly performing optoelectronic devices.

Experimental

Spiro-m-TTB and spiro-TAD were used as received from Covion Semiconductors GmbH/Frankfurt (>99.9 % pure; according to HPLC and 1H-NMR).

Conducting glass sheets, coated with fluorine doped SnO_2 (1mm; Asahi) were used as substrates and structured with a mixture of 4N HCl and zinc granulate. The structured substrates were cleaned by subsequent ultrasonification in aceton, ethanol, Hellmanex and destilled water. A thin, compact layer (50-100 nm) of TiO_2 was applied via spray pyrolysis of a 0.02 M ethanolic solution of titanium(IV)bis(acetylacetonat)diisopropoxide at 450 °C. A thin, 3 to 4 µm thick film of the holeconducting material was evaporated onto the sample from a tantalum crucible. Typical deposition rates were 1 nm/s at a typical background pressure of 10^{-6} Torr. Finally a 40 nm thick gold layer was vapor deposited in top of the organic layer. The sample was not exposed to ambient atmosphere between the two evaporation steps.

Mobilities were measured with a conventional time-of-flight setup. The sample was placed inside a cryostate (Oxford Instruments), equipped with quartz windows and kept under nitrogen atmosphere. A frequency doubled ruby laser (6 ns pulse width, 354 nm excitation wavelength, 0.1 Hz) was used as excitation light source. Optical neutral density filters were used to adjust the excitation energy. The exposures were such that the maximum charge injected into the sample was always less then 5% of the charge stored on the capacitor, represented by our device. The displacement current was measured in the external circuit by time resolved measurement of the potential drop over a variable resistance, using a Tektronix digital oscilloscope. From the absorption coefficient of the CTMs and TiO_2 we calculated that more than 90 % of the excitation light is adsorbed in the TiO_2 layer and the first 10 % of the organic film.

References

[1] Hadziioannou, G.; van Hutten, P. F. *Semiconducting polymers*; Wiley-VCH: Weinheim, 2000.

[2] Müllen, K.; Wegner, G. *Electronic Materials: The Oligomer Approach*; Wiley-VCH: Weinheim, 1998.

[3] Bach, U.; Lupo, D.; Compte, P.; Moser, J. E.; Weissörtel, F.; Salbeck, J.; Spreitzer, H.; Grätzel, M. *Nature* **1998**, *395*, 583-585.

[4] Yu, G.; Gao, J.; Hummelen, J. C.; Wudl, F.; Heeger, A. J. *Science* **1995**, *270*, 1789.

[5] Granström, M.; Petrisch, K.; Arias, A. C.; Lux, A.; Andersson, M. R.; Friend, R. H. *Nature* **1998**, *395*, 257-260.

[6] Halls, J. J. M.; Walsh, C. A.; Greenham, N. C.; Marseglia, E. A.; Friend, R. H.; S.C.Moratti; Holmes, A. B. *Nature* **1995**, *376*, 498-500.

[7] Dimitrakopoulos, C. D.; S.Purushothaman; Kymissis, J.; Callegari, A.; Shaw, J. M. *Science* **1999**, *283*, 822-824.

[8] Horowitz, G. *Adv. Mater.* **1998**, *10*, 365-377.

[9] Katz, H. E.; Bao, Z. *J. Phys. Chem. B* **1999**, *in print*.

[10] Thelakkat, M.; Schmidt, H.-W. *Adv. Mater.* **1998**, *10*, 219-223.

[11] Oldham, W. J.; Lachicotte, R. J.; Bazan, G. C. *J. Am. Chem. Soc.* **1998**, *120*, 2987-2988.

[12] Naito, K.; Miura, A. *J. Phys. Chem.* **1993**, *97*, 6240.

[13] O'Brian, D. F.; Burrows, P. E.; Forrest, S. R.; Koene, B. E.; Loy, D. E.; Thompson, M. E. *Adv. Mater.* **1998**, *10*, 1108-1112.

[14] Salbeck, J.; Weissörtel, F.; Bauer, J. *Macromol. Symp.* **1997**, *125*, 121-132.

[15] Salbeck, J.; Yu, N.; Bauer, J.; Weissörtel, F.; Bestgen, H. *Synth. Met.* **1997**, *91*, 209-215.

[16] Kavan, L.; Graetzel, M. **1995**, *40*, 643.

[17] Melnyk, A. R.; Pai, D. M. *Transient photoconductivity measurement*; 2 ed.; Rossiter, B. W. and Baetzold, R. C., Ed.; Wiley: New York, 1993; Vol. 8, pp 321-389.

[18] Borsenberger, P. M.; Pautmeier, L.; Bässler, H. *J. Chem. Phys.* **1991**, *94*, 5447-5454.

[19] Pai, D. M.; Janus, J. F.; Stolka, M. *J. Phys. Chem.* **1984**, *88*, 4714-4717.

[20] Stolka, M.; Janus, J. F.; Pai, D. M. *J. Phys. Chem.* **1984**, *88*, 4707.

[21] De Cloedt, K. *Characterisation of new hole conductors for the dye-sensitised solid-state solar cell*; Universiteit Gent: Gent/Belgium, 1999.

[22]   Richter, A. M. *www.syntec-synthon.com*, SynTec GmbH Wolfen/Germany.

[23]   Weissörtel, F. *Synthese und Characterisierung spiroverknüpfter niedermolecularer Gläser für optoelectronische Anwendungen*; University of Regensburg: Regensburg, 1999.

[24]   Borsenberger, P. M.; Fitzgerald, J. J. *J. Phys. Chem.* **1993**, *97*, 4815-4819.

Chapter 11

Conclusion

The objective of this work was to develop an efficient solid-state dye-sensitized solar cell, based on nanoporous metal oxide electrodes and organic charge transport materials. *Spiro*-OMeTAD was chosen as an appropriate candidate for this particular application as its redox level proved to match that of the ruthenium polypyridyl sensitizers commonly applied in photoelectrochemical solar cells. Furthermore it features high stability of the amorphous state, high conductivities in the partially doped state and a remarkable stability of its radical cation. The outcome of my work can be summarized as follows:

- A highly efficient solid-state dye-sensitized organic/inorganic heterojunction was realized. Monochromatic photon-to-electron conversion efficiencies as high as 50 % (uncorrected for transmission losses) were obtained compared to 70 % in similar photoelectrochemical solar cells. Maximum white light conversion efficiencies reached 1.8 % (AM1.5; 10 mW/cm^2). This was the first time that dye-sensitized hybrid organic/inorganic solar cells with such high conversion yields were obtained, exceeding previously reported performances by about two orders of magnitude.

- The electron transfer steps, proceeding in solid-state dye-sensitized solar cells were studied in great detail, using femto- to nanosecond laser spectroscopy. Dye regeneration proved to proceed at least one order of magnitude faster than in comparable photoelectrochemical systems and several orders of magnitude faster then the competing recombination reactions.

- Conducting glass based on fluorine doped SnO_2, covered with a dense TiO_2 layer, was found to be the appropriate window material for solid-state dye-

sensitized solar cells. Gold, platinum, carbon and conducting polythiophene polymers were found to be appropriate contact materials to *spiro*-OMeTAD. The conductivity of thin *spiro*-OMeTAD films could be continuously adjusted by addition of appropriate dopants like [N(p-C$_6$H$_4$Br)$_3$][SbCl$_6$] or the diradical cation *spiro*-OMeTAD^{++}(PF$_6$)$_2$. The latter was synthesized and isolated as a pure salt.

- Mobility studies were conducted on charge transport materials containing *spiro*-centers. High charge mobilities were measured, comparable to those of non-*spiro*-analogues. The '*spiro*-concept' therefore proved to be a powerful strategy to confer high morphologic stability to a material, without deteriorating its electronic properties.

- For the first time it could be shown, that the electronic properties of organic/inorganic photovoltaic junctions can be controlled by means of a self-assembled organic layer located at the heterojunction. The dipole moment of the self-assembling molecules was found to be the chief parameter, controlling the rectifying junction properties.

- Photocurrent action spectra were recorded for front- and backside illumination and the values analyzed using a recombination model. The results suggested, that interfacial charge recombination is the main loss mechanism in solid-state dye-sensitized solar cells with a mean free pathway of about 1 μm for the photoinjected electrons.

Outlooks

The most urging question, which is expected to be answered in this very last section of my work is of course: '*How efficient will solid-state dye-sensitized solar cells be in the future, where are the theoretical limits, and what are the strategies leading us to this point.*'

First of all, there is no theoretical limit which would impede solid-state dye-sensitized solar cells from being as efficient as their photoelectrochemical counterparts (up to 10 % at AM 1.5 ∕ 100 mW/cm^2)[Nazeeruddin, 1993 #82]. The devices presented in this study suffer mainly from a significant charge carriers loss due to ***recombination***. Different strategies might be pursued, by means of which interfacial charge recombination could be restrained: by modulation of the surface states (using e.g. ^{t}butylpyridine)[Nazeeruddin, 1993 #82], by introduction of an appropriate dipole field at the interface (see chapter 7) or by an increase of the electron mobility inside the nanoporous TiO$_2$ phase. Stacking of solar cells in several layers on top of each other as proposed in reference[Hiramoto, 1990 #175] is another possible but not very practical approach to this problem.

In view of future applications it will be crucial to study the ***stability*** of the solid junction solar cell under simulated operation conditions. Upon storage of the device under ambient conditions the short circuit current generally decreased, while the open-circuit voltage and fill-factor increased with time. These effects generally compensated each other, leaving the overall efficiency basically unaltered. Sealing the cells towards oxygen and moisture will be a requisite to elucidate the underlying processes.

Conductivity of the *spiro*-OMeTAD phase is a further issue, which is of particular importance at high light intensities. It generally results in poor fill factors, which are controlled by the cell's series resistance. Here the device has to be optimized in

thickness and degree of doping, according to the potential field of application (indoor/outdoor).

Light harvesting is far from optimum, even in the most efficient solid-state solar cells studied so far. None of the two efficient merocyanine sensitizers absorbs light beyond a wavelength of 700 nm. A near-IR sensitizer is needed, which extends the spectral sensitivity of the cell much further into the near infrared when coabsorbed with a merocyanine dye.

Even in photoelectrochemical solar cells the ***open circuit voltage*** is only about _half_ the value of the optical bandgap energy of the sensitizer (divided by *e*)[Kay, 1994 #216][Grätzel, 2000 #204]. The resulting tremendous loss in efficiency is also observed in the solid-state analogs. Usually the necessity of driving forces for dye regeneration and electron injection are held responsible for this voltage drop[Kay, 1994 #216]. However, examples can be found in the field of interpenetrating polymer network solar cells, where the optical bandgap energy of the polymer and the open circuit voltage of the cell coincide[Granström, 1998 #101]. This of course opens up very exciting perspectives and one might *dream* of surpassing the best ever-reported efficiencies of photoelectrochemical solar cells.

The open-circuit voltage is mainly limited by the difference in workfunction of the two semiconductors used. Improvements might therefore be achieved by using an organic semiconductor showing a slightly more positive ground state redox potential. However, even when using the same starting materials (TiO_2 and *spiro*-OMeTAD) values for Voc varied in the range of 300 to 800 mV. This, as several additional factors determine Voc, such as the dipole field of the self-assembled molecular layer at the interface, the occurrence of recombination, the flatband potential determining action of ions like H^+ or Li^+ or Fermi-level pinning due to the presence of bandgap states. All these factors have to be controlled in order to maximize the cell voltage. This demands careful engineering of the interface and additional studies to widen our comprehension and improve our control over the underlying working principals.

Acknowledgements

Curriculum vitae

Name   **Udo Bach**
Date of birth   14th of June 1968 in Singen (Germany)
Nationality   German

Education

1995-2000   **Ph.D. Thesis** at the Swiss Federal Institute of Technology (EPFL) in the group of Prof. M. Grätzel:

1989 – 1995   Studies in Chemistry at the University of Konstanz (Germany)
master thesis on: *EPR and NMR spectroscopic studies and synthesis of spin-chemically active ruthenium(III) and iron(III)bipyridyl-cyano complexes*
Final Examination: 5/1995

1988   **Abitur** (final highschool examination) Friedrich Wöhler Gymnasium
Singen am Hohentwiel

Assistant Work

1998-1999   Supervisor - master thesis of Kenny DeCloedt *"hole mobilities in organic charge transport materials determined via the time-of-flight technique"*

1998   Supervisor - master thesis of Jessica Krüger *"modification of TiO$_2$ semiconductor films for   the application in hybrid solid-state solar cells"*

1995-1998   Teaching lab classes - physical chemistry (EPFL)

1993-1994   Teaching lab classes photochemistry (University of Konstanz)

Patents

1)   **DE 197 11 713 A 1**
U. Bach, M. Grätzel, J. Salbeck, F. Weißörtel & D. Lupo, *Photovoltaische Zelle*
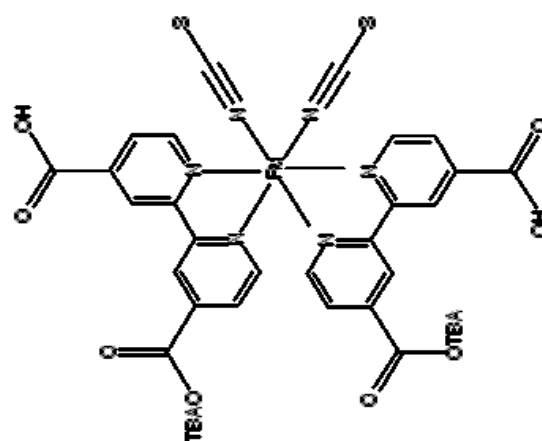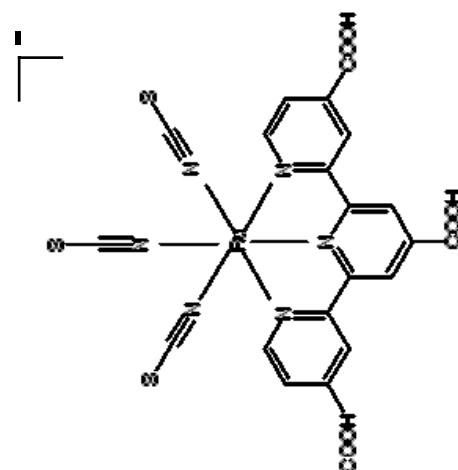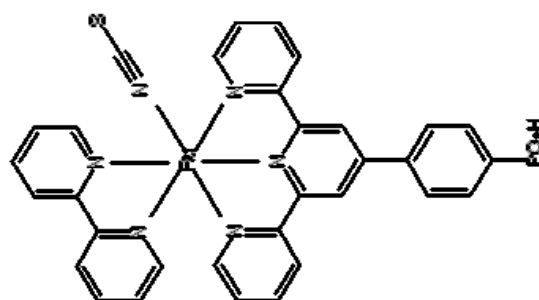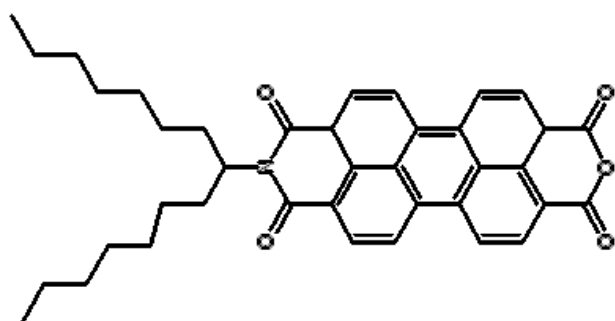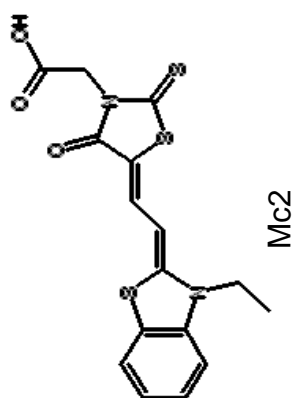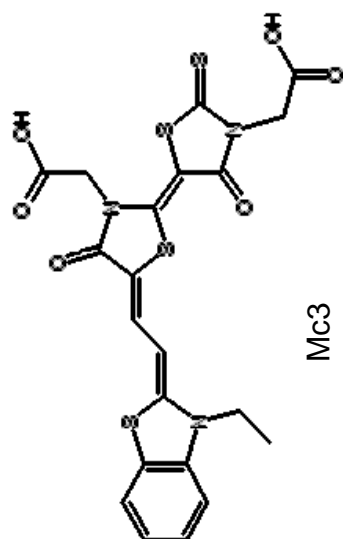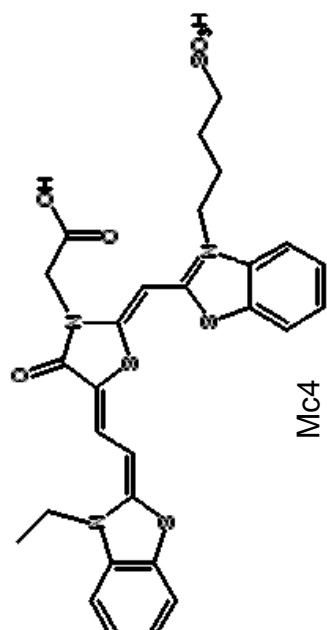
Publications

1)   **Nature** *395*, 583-585 (1998)
U. Bach, D. Lupo, P. Comte, J.E. Moser, F. Weissörtel, J. Salbeck, H. Spreitzer & M. Grätzel
Solid-state dye-sensitized mesoporous TiO$_2$ solar cells with high photon-to-electron conversion efficiencies.

2)   **J. Am. Chem. Soc.** *121*, 7445-7446 (1999)
U. Bach, Y. Tachibana, J.E. Moser, S.A. Haque, D.R. Klug, M. Grätzel & J.R. Durrant
Charge separation in solid-state dye-sensitized heterojunction solar cells.

3)   **Adv. Mater.** *12 (6),* 447-451 (2000)

J. Krüger, U. Bach & M. Grätzel

Modification of TiO$_2$ heterojunctions with benzoic acid derivatives in hybrid molecular solid-state devices

4)   **Adv. Mater.** *12 (14),* 1060-1063 (2000)

U. Bach, K. DeCloedt, H. Spreitzer & M. Grätzel

Characterization of hole transport in a new class of spiro-linked oligotriphenylamine compounds

5)   **Encyclopedia of Electrochemistry** Volume 6: *Semiconductor Electrodes and Photoelectrochemistry*, edited by Bard/Stratmann, WILEY-VCH/Weinheim (2001), *manuscript in preparation (chapter contribution)*

6)   **J. Phys. Chem. B** *102*, 3649-3650 (1998)

J.E. Moser, D. Noukakis, U. Bach, Y. Tachibana, D.R. Klug, J.R. Durrant, R. Humhry-Baker & M. Grätzel

Comments on "Measurements of ultrafast photoinduced electron transfer from chemically anchored Ru-dye molecules into empty electronic states in a colloidal anatase TiO$_2$ film"

Conferences

2000   SPIE's 45th Annual Meeting, **San Diego** (USA); *oral presentations*

The concept of dye-sensitized mesoporous solid-state heterojunction solar cells

2000   ETH/EPFL-WIS Forum on Advanced Materials, **Rehovot** (Israel); *poster presentation*

Solid-state dye-sensitized heterojunction solar cells

1999   Int. Symp. on New Trends in Photoelectrochemistry, **Nice** (France); *poster presentation*

Solid-state dye-sensitized heterojunction solar cells

1999   Symp. of the Swiss Society for Photochemistry, **Fribourg** (Switzerland); *oral presentations*

Solar cells based on solid-state dye-sensitized heterojunction solar cells

1999   *Invited Talk* at the University of **Konstanz** (Germany)

Dye-sensitized nanocrystalline semiconductor photovoltaic devices

1998   Material Research Society - Fall Meeting, **Boston** (USA); *two oral presentations*

1) Efficient photovoltaic conversion by mesoporous junctions (invited talk)

2) Dye sensitized mesoporous solid heterojunction solar cells showing high photon-to-electron conversion efficiencies

1998   *Invited talk* at the Imperial College in **London** (UK)

Electron transfer dynamics in solid-state dye-sensitized mesoporous solar cells

1997   Polymer & Material Research Symposium **Bayreuth** (Germany) *poster presentation*

U. Bach, F. Weissörtel, J. Uebe, M. Grätzel, D.W. Lupo & J. Salbeck

Ultrafast hole injection from dye molecules into an organic hole conductor for dye sensitized solar cells

1996   Seminar on Inherently Conducting Polymers **Brugge** (Belgium)

Mc4

perylene

Mc3

Z636

Ru(ctpy)(SCN)3

Mc2

N719
[cis-Ru(dcbpyH)2(SCN)2TBA2]